

Applications of Ultrafast Pulse Shaping to Two-Photon Fluorescence Microscopy

by

Meredith Holland Brenner

A dissertation submitted in partial fulfillment
of the requirements for the degree of
Doctor of Philosophy
(Applied Physics)
in the University of Michigan
2013

Doctoral Committee:

Associate Professor Jennifer P. Ogilvie, Chair
Professor Jens-Christian D. Meiners
Professor Theodore B. Norris
Professor Duncan G. Steel
Professor Joel A. Swanson

“Research is what I’m doing when I don’t know what I’m doing.”

— Werner von Braun

Copyright Meredith Holland Brenner 2013

All Rights Reserved

For my parents

ACKNOWLEDGEMENTS

During my first physics class, I was given an “All-Star Physicist” trading card as a bit of a joke. It featured Maria Goppert-Mayer, and I wound up keeping the card as a lucky charm after that first physics class piqued my interest in the field. Little did I know that more than ten years later, I would write my PhD thesis on work made possible by hers. I carry that trading card in my wallet to this day, and it reminds me that I have many people to thank for helping me get this far.

The trading card was given to me by my high school physics teacher, Justin Parke, who made an intimidating field accessible and fun. At the University of Maryland, I was lucky to have two great mentors - Tom Cohen, whose quantum mechanics course motivated me to stick with physics when I was thinking of quitting, and Steve Rolston, who welcomed me into his lab and introduced me to the field of optics.

At Michigan, I always felt like I had a home in the Applied Physics program. I am grateful to the many other Applied Physics students for their advice and friendship. Cynthia McNabb and Charles Sutton have helped with navigating the logistics of getting a PhD, and Brad Orr, Roy Clarke, and Cagliyan Kurdak have provided excellent leadership. Similarly, I want to thank the staffs of Physics and Biophysics, who were invaluable when my appointments were through their departments.

I appreciate the advice and insight my committee members have given me during my PhD. I want to thank them for taking the time to help me throughout this process and am grateful for their contributions.

I owe a huge thanks to Professor Ogilvie. Her excitement about every step of

progress in the lab was a great motivator when I felt stuck. I admire her knowledge of and love for physics, not to mention her tenacity as a researcher, and am grateful for her support and guidance over these years.

I would like to thank Joel Swanson for his guidance as a collaborator and for welcoming me into his lab. His group members have all been incredibly accomodating and helpful. I particularly want to thank Sam Straight, who taught me everything I know about tissue culture. I went from barely being able to use a pipetter to maintaining my own cell line and transfecting my own samples in no time thanks to his guidance. I'd also like to thank Adam Hoppe, who has provided his FRET stoichiometry expertise long-distance.

I couldn't have accomplished this without the rest of the Ogilvie group. Sarah Nichols, who started as a postdoc just before I joined the lab, was instrumental in helping get this project going. I learned a lot about CARS microscopy from Brandon Bachler, who was great company during long days in the lab and office. Dan Flynn and Amar Bhagwat are inheriting "my" microscope and I know it will be in excellent hands. I admire their excitement to learn and try new things. Officemate and unofficial group member Jessica Ames has been a very good friend as we've shared in the struggles of graduate school. I wish her the best of luck as she finishes her degree. I also have to thank Dawen Cai for contributing his encyclopedic knowledge of fluorescent proteins and creativity in developing new ideas.

Although I did not work directly with the 2DES side of the group, they have been supportive as well. Jeff Meyers and Kristin Lewis provided invaluable guidance when I was getting started in the group. I owe Daniel Wilcox and Frank Fuller thanks for always asking the hard questions that make me really think. It has also been great to get to know Seckin, Jie, Anton, Henry, Veronica, and Andrew, and I'm sure they will all do amazing work in the lab.

William Fisher has never hesitated to help me in any way he could. He has

always reminded me that I could do this, even when I thought it was impossible. I am grateful to him for teaching me the importance of taking breaks to relax, even if I still struggle to heed that advice, and for being the best personal chef a girl writing her thesis could ever hope for. I cannot thank him enough for everything he has done.

Finally, I would have never made it through my PhD without the support of my parents. They have been behind me every step of the way, from driving the truck from Maryland when I moved, to letting me vent on countless phone calls when nothing was working in the lab, all the way to organizing the menu for my defense. I am grateful for their advice and for giving me the skills and confidence to make it this far. I could never thank them enough for their love and support, but I can answer a long-standing question of theirs: the anchors behind Randall Lab were salvaged from Lake Michigan by the University of Michigan Center for Great Lakes and Aquatic Science. They are thought to be from 19th century lumber ships.

As Einstein said, “the important thing is to not stop questioning.” I thank everyone I’ve mentioned here, and many others, for helping me learn this - and I look forward to lots of new questions!

TABLE OF CONTENTS

DEDICATION	ii
ACKNOWLEDGEMENTS	iii
LIST OF FIGURES	viii
LIST OF ABBREVIATIONS	x
ABSTRACT	xi
CHAPTER	
I. Introduction	1
II. Pulse Shaping	15
2.1 Introduction	15
2.2 Basics of 4f Pulse Shaping	18
2.3 Phase Shaping for Two-Photon Fluorescence	21
2.4 Multiphoton Intrapulse Interference Phase Scan	37
2.5 Conclusion	41
III. Linear Unmixing	47
3.1 Introduction	47
3.2 Theory of Linear Unmixing	52
3.3 Experimental Methods	57
3.4 Results	66
3.5 Discussion	72
IV. Fluorescence Resonance Energy Transfer	79
4.1 Introduction	79

4.2	Fluorescence Resonance Energy Transfer	81
4.3	Detection of FRET Using Pulse Shaping	85
4.3.1	Introduction	85
4.3.2	Experimental Methods	87
4.3.3	Results and Discussion	92
V. Fluorescence Resonance Energy Transfer Stoichiometry . . .		100
5.1	Introduction	100
5.2	Theory of One-Photon FRET Stoichiometry	103
5.3	Theory of Two-Photon FRET Stoichiometry	114
5.4	Current Results	125
5.4.1	Experimental Methods	125
5.4.2	Results	135
5.5	Future Work	138
VI. Conclusion		144

LIST OF FIGURES

Figure

1.1	Jablonski diagram of a fluorescence process.	2
1.2	Jablonski diagram of two-photon excited fluorescence.	5
1.3	Three-dimensional sectioning in two-photon microscopy.	7
2.1	Diagram of a 4f pulse shaper.	18
2.2	Schematic of the liquid crystal structure in an SLM.	20
2.3	Example of photon combinations in two-photon absorption.	24
2.4	Section of a random binary phase mask.	27
2.5	Example of random binary phase shaping.	29
2.6	Tuning of phase masks.	30
2.7	Fundamental laser spectrum, amplitude shaped spectrum, and phase mask used in simulation of random binary shaping.	31
2.8	Comparison of different flat-phase widths.	32
2.9	Temporal behavior of shaped pulses.	34
2.10	Simulated SH intensities and electric field for a phase shaped pulse centered at 820 nm with a 40 nm central flat section.	36
2.11	Sample MIIPS trace.	39
2.12	Improvement in SH intensity achieved with MIIPS.	41
3.1	Simulated SH spectra of ultrabroadband lasers.	50
3.2	Experimental setup for linear unmixing.	58

3.3	Spectra of fluorescent proteins used for linear unmixing.	60
3.4	Linear unmixing binary phase mask centered at 820 nm.	61
3.5	Linear unmixing binary phase mask centered at 780 nm.	61
3.6	Second harmonic spectra of shaped pulses.	62
3.7	Demonstration of selective excitation using shaped pulses.	67
3.8	Images after linear unmixing.	71
4.1	Jablonski diagram of FRET process.	82
4.2	Experimental setup for detection of FRET.	87
4.3	Two-photon absorption spectra of mCerulean and mCherry.	90
4.4	Second harmonic spectra of the shaped pulses.	91
4.5	Demonstration of selective excitation in the No FRET condition.	92
4.6	Demonstration of selective excitation in the FRET condition.	94
5.1	Example of FRET stoichiometry.	111
5.2	One-photon FRET stoichiometry data.	113
5.3	Two-photon cross-section of TagRFP.	115
5.4	Experimental setup for FRET stoichiometry.	126
5.5	Spectrum of the laser used for FRET stoichiometry experiments.	128
5.6	Two-photon cross-sections of fluorophores used for FRET stoichiometry.	129
5.7	Phase mask for selective excitation of TagRFPt.	130
5.8	Phase mask for selective excitation of TFP.	131
5.9	SH spectra of shaped and TL pulses for FRET stoichiometry.	132
5.10	Example corrected image and corresponding mask.	136
5.11	Spectrum of Vteon ultrabroadband laser.	140

LIST OF ABBREVIATIONS

BBO	Beta Barium Borate
CARS	Coherent Anti-Stokes Raman Scattering
CFP	Cyan Fluorescent Protein
DMEM	Dulbecco's Modified Eagle's Medium
FLIM	Fluorescence Lifetime Imaging Microscopy
FRET	Fluorescence Resonance Energy Transfer
GFP	Green Fluorescent Protein
MII	Multiphoton Intrapulse Interference
MIIPS	Multiphoton Intrapulse Interference Phase Scan
NA	Numerical Aperture
OPO	Optical Parametric Oscillator
PBS	Phosphate-Buffered Saline
PMMA	Polymethylmethacrylate
PMT	Photomultiplier Tube
SH	Second Harmonic
SHG	Second Harmonic Generation
SLM	Spatial Light Modulator
Ti:Sapph	Titanium:Sapphire
TL	Transform-Limited

ABSTRACT

Applications of Ultrafast Pulse Shaping to Two-Photon Fluorescence Microscopy

by

Meredith Holland Brenner

Chair: Jennifer P. Ogilvie

Two-photon fluorescence microscopy is a popular method for imaging biological systems, offering benefits over one-photon fluorescence microscopy including increased penetration depth in tissues and reduced photobleaching. Experiments requiring selective excitation of multiple fluorophores are challenging to perform with existing two-photon fluorescence methods. Conventional two-photon microscopes employ tunable laser systems with limited temporal resolution. Other approaches include multiple-beam setups which may have complicated alignments, and ultrabroadband lasers, which simultaneously excite all fluorophores. The use of ultrafast pulse shaping methods in two-photon fluorescence microscopy offers the ability to tailor an ultrabroadband pulse to excite specific fluorophores for multicolor two-photon microscopy applications.

This thesis demonstrates three applications of ultrafast pulse shaping to multicolor two-photon fluorescence microscopy. The first is the use of pulse shaping with linear unmixing of fluorescence signals to perform three-color two-photon imaging of live cells expressing fluorescent proteins. Resulting images show that the method can

identify cells expressing single fluorescent proteins as well as cells expressing three fluorescent proteins simultaneously. This ultrafast pulse shaping approach has a simpler setup compared to other three-color imaging techniques, and can be easily expanded to more fluorophores.

Two applications of ultrafast pulse shaping to Fluorescence Resonance Energy Transfer (FRET) microscopy are also presented. FRET microscopy is a powerful tool for observing interacting molecular species. While significant progress has been made in obtaining quantitative one-photon FRET measurements, similar progress in two-photon FRET measurements has been lacking. The techniques presented here use the selective excitation provided by pulse shaping to pave the way towards quantification of two-photon FRET. First, the use of pulse shaping to distinguish between FRET and no FRET conditions in live cells expressing fluorescent proteins is demonstrated. Differing intensity contrast results between cells imaged with different shaped pulses indicate that selective excitation can be applied to donor and acceptor fluorophores in FRET constructs and FRET can be detected. The second application discussed is the generalization of FRET stoichiometry to two-photon FRET measurements. A new theory for two-photon FRET stoichiometry is derived, and initial experimental measurements on live cells expressing fluorescent proteins are presented, yielding results that are largely consistent with expectations.

CHAPTER I

Introduction

The field of optical microscopy has seen intense development at the crossroads of physics and biology. From its most basic implementation as a single focusing lens to the complex laser-based systems found in modern research labs, optical microscopy has proven instrumental to the study of biological structures and processes. The earliest versions of the microscope, dating back 350 years, relied on the light absorption properties of the sample to generate contrast in the final image [1]. Biological samples can be challenging to image with this basic implementation, however; they often lack absorbing molecular species or are so thin that their absorption is negligible [2]. Even with the addition of histological stains, obtaining enough contrast to form meaningful images can be a challenge [1]. Numerous variations on the basic bright field microscope have been developed in an attempt to improve image quality, including phase contrast, differential interference contrast, and dark field methods [1, 2]. However, one of the most common techniques for improving contrast in microscope images and to enable labeling of specific molecular species is the use of fluorescence.

The first foray into fluorescence microscopy was performed in 1950 by Coons and Kaplan [3], who mixed antibodies with fluorescein dye. The resulting dye conjugate was used as a stain on fixed tissue samples; when imaged under the microscope, the locations of fluorescent signal indicated the locations of the antibody in the tissue

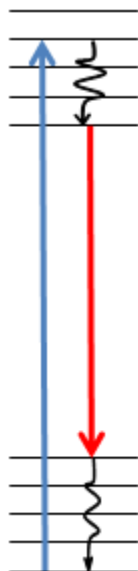


Figure 1.1: Jablonski diagram of a fluorescence process. The molecule is excited from its ground state via absorption of a photon. It then undergoes vibrational relaxation before emitting a photon and returning to the ground state, where it experiences further vibrational relaxation.

[3]. This type of labeling to indicate localization has proven to be one of the key benefits of fluorescence microscopy compared to more traditional imaging methods, in addition to the improved image contrast. Figure 1.1 shows a Jablonski diagram of how fluorescence works. Fluorescence occurs when a molecule initially in the ground state absorbs a photon with a specific energy (or frequency) and is excited to some vibrational level of a higher electronic state. Many such absorption transitions are possible, and their probabilities can be determined from the Franck-Condon factors; these define the absorption spectrum of the fluorophore [4, 5]. Once excited, fast vibrational relaxation occurs so that the molecule is left in the lowest vibrational level of the excited electronic state. Called internal conversion, this process takes place on the order of picoseconds. An important feature is that because the internal conversion is so rapid, all fluorescence occurs from this lowest vibrational level [4, 5]. The molecule then relaxes to the ground state via emission of a photon, which is detected as the fluorescent signal. As with excitation, the transition back to the ground state can

end with the molecule in a vibrational level before subsequent vibrational relaxation. This creates the emission spectrum of the fluorophore [4, 5].

Fluorescence emission has several unique features. The first is that the absorption and emission spectra of a fluorophore are often mirror images of each other. This is due to the fact that the spacing of the vibrational levels in the ground and excited electronic states are typically similar, because the electronic excitation often does not significantly alter the nuclear geometry [5]. Transitions to the excited state occur on the order of femtoseconds, which is too fast for displacement of nuclei according to the Franck-Condon principle. Consequently, transitions to particular vibrational levels that occur in excitation are likely to occur in reverse in emission as well [4, 5]. A related feature is that the fluorescence emission spectrum is independent of the excitation wavelength used. Called Kasha's rule, this is because of the fast vibrational relaxation to the lowest vibrational level of the excited electronic state. All fluorescence occurs from this state regardless of the specific excitation transition [4, 5]. Another critical feature of fluorescence emission is the Stokes shift. Because of the fast vibrational relaxations that occur during both excitation and relaxation, the emitted light has less energy than the excitation light [4, 5]. This appears as a shift between the excitation and emission spectra, as the emitted light is at longer (redder) wavelengths than the excitation light. Environmental factors such as solvents can also contribute to this effect. This spectral separation makes it possible to efficiently filter out the excitation light, reducing background signal in fluorescence measurements [4, 5].

Although the Stokes shift and appropriate filters make it possible to achieve good contrast in fluorescence images by blocking out the excitation light, basic fluorescence microscopy still has limitations. A particular concern is the presence of unwanted signal from axial planes other than the plane of focus. For the high numerical aperture (NA) objectives commonly used in fluorescence microscopy, the depth of field (that

is, the axial distance over which a region remains in focus) is less than 1 μm [6]. Up to 80% of the light observed when imaging samples as thin as 5 μm may come from out of focus regions [6]; this thickness is comparable to that of adherent cells grown on a tissue culture dish. Consequently, when performing fluorescence imaging in live cells, this unwanted background signal can become significant. It appears as blurry background signal around features of interest [6, 7]. As thicker samples such as tissue sections or live animals become targets for fluorescence microscopy, this problem of out-of-focus fluorescence dominating the image becomes pronounced.

One of the first solutions to this problem - and one that is still considered a standard today - is confocal microscopy. First proposed in a patent by Minsky in 1957 [8], confocal microscopy relies on a modified optical setup to block out-of-focus fluorescence. Modern laser scanning confocal setups place a pinhole aperture before the detector, and an objective is used to focus onto the sample. Light from the axial focal plane passes through the pinhole, but light from other axial positions is blocked by the edges of the aperture [6, 7]. The objective itself provides a tight lateral focus; to create the entire image, the focal spot is scanned across the sample. Thus, confocal microscopy has a three dimensional sectioning ability, making it capable of acquiring fluorescence images with improved contrast over wide field methods. However, confocal setups can be difficult to align due to the pinhole. In addition, the gains in sample thickness through which high-quality images can be obtained are modest, increasing only to about 50 μm [6]. This means that confocal microscopy is still not a viable method for biological imaging deep into tissues.

Multiphoton microscopy provides all the benefits of confocal microscopy while offering several advantages including dramatically improved penetration depth. In multiphoton microscopy, more than one photon is absorbed to achieve excitation of the fluorescent molecule. This is a nonlinear optical process and thus has unique characteristics not found in the single-photon fluorescence techniques described above.

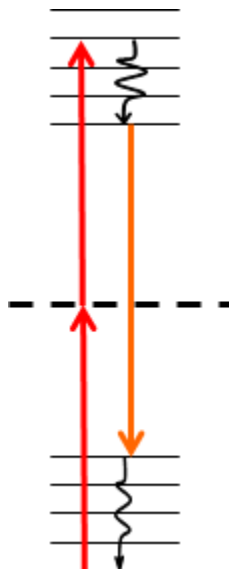


Figure 1.2: Jablonski diagram of two-photon excited fluorescence. Two photons are absorbed whose combined energies are enough to excite the fluorophore. This occurs through a virtual state, denoted by the dashed line. The vibrational relaxation and fluorescence occurs in the same way as in one-photon excited fluorescence.

The most common multiphoton microscopy method is two-photon fluorescence microscopy. Other multiphoton microscopy methods include three-photon fluorescence, second harmonic generation, third harmonic generation, Coherent Anti-Stokes Raman Scattering (CARS), and pump-probe microscopy [9–11]. Two-photon microscopy is the focus of the work presented in this thesis. It is based on the phenomenon of two-photon absorption, which was predicted in 1931 by Maria Goppert-Mayer in her doctoral thesis ([12], English translation in [13]). However, it was not observed experimentally until after the development of the laser; the first report of two-photon excited fluorescence was by Kaiser and Garrett in 1961 [14].

A Jablonski diagram illustrating the two-photon excited fluorescence process is shown in figure 1.2. In two-photon excitation, two photons which individually do not have the energy required for the transition are absorbed nearly simultaneously, allowing the transition to occur. The figure shows two photons of equal energy - half that needed for the transition - being used, but any two photons whose energies sum to the necessary amount can perform two-photon excitation [15]. This process

is mediated by a virtual state, designated by the dashed line in the figure [16]; it is not a real eigenstate of the system. Its lifetime is quite short - on the order of 10^{-16} seconds [17] - so the second photon must be absorbed within this time frame. The probability of a two-photon transition occurring can be calculated with second-order time-dependent perturbation theory. The final form of the probability goes as [13, 16, 18]:

$$P \propto \left| \sum_k \frac{\mu_{mk} \vec{\mu}_{kn} \vec{E}^2}{\omega_{kn} - \omega} \right|^2 \quad (1.1)$$

Here, the transition is from the ground state n to the excited state m , and the probability is summed over all intermediate virtual states k . The presence of two dipole moments in this equations indicates that the selection rules are different for one- and two-photon transitions: while one-photon transitions are only allowed for states of opposite parity, two-photon transitions are only allowed for states of the same parity [15, 16].

An important feature of two-photon excitation is displayed in equation (1.1) - its dependence on the square of the incident light intensity. Because of this, appreciable two-photon excitation only occurs in regions of high intensity. This makes ultrafast pulsed lasers ideal for exciting two-photon fluorescence, as the short pulse durations act to concentrate the laser power in time, leading to higher peak intensities [2, 15]. Because two-photon excitation is so rare at the intensities used in one-photon fluorescence microscopy - there is approximately one two-photon absorption per fluorophore every one hundred seconds using one of the brightest available conventional light sources [19] - it was not until the advent of pulsed lasers that two-photon fluorescence microscopy was demonstrated. It was first performed by Denk and colleagues in 1990 [20], who demonstrated the use of two-photon excited fluorescence in a laser scanning microscope to image fluorescent beads as well as live cultured pig kidney cells.

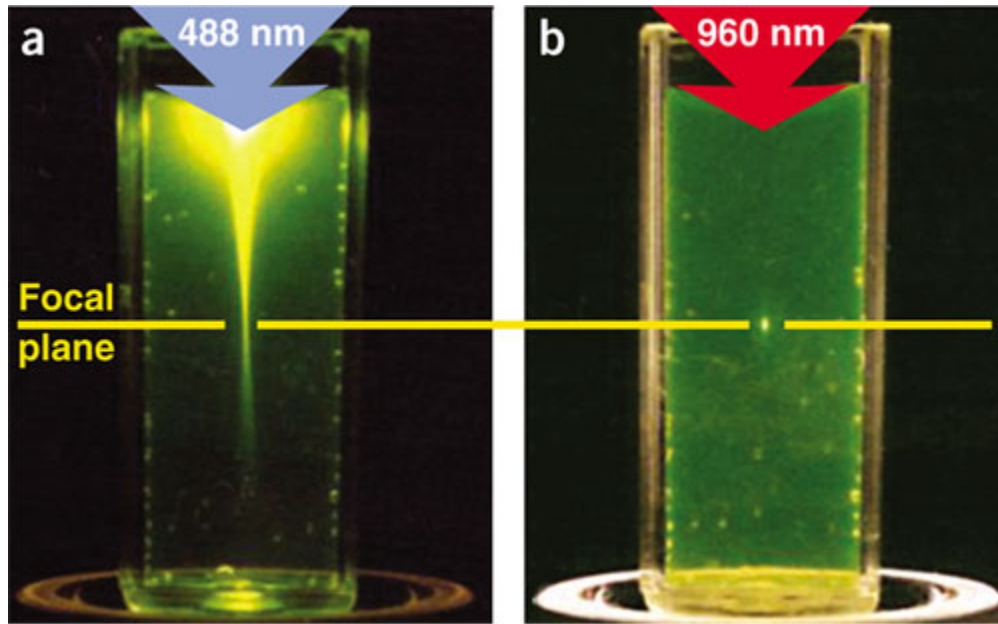


Figure 1.3: Three-dimensional sectioning in two-photon microscopy. A fluorescein solution is undergoing one-photon fluorescence on the left and two-photon fluorescence on the right. In both cases the incident laser beam is propagating from the top down and the focal plane is denoted by the yellow line. Note that in the one photon case, a significant amount of fluorescence signal is generated throughout the laser beam path. In the two-photon case, however, fluorescence only occurs at the focus. Reprinted by permission from Macmillan Publishers Ltd: Nature Biotechnology, [17], copyright 2003.

To further generate the required high intensities, high numerical aperture objectives are used and the laser is focused to a diffraction-limited spot [16, 20]. The result of this tight focusing and strong intensity dependence is that two-photon fluorescence only occurs in a very small region around the focus, generally sub-femtoliter in volume [15, 16]. This gives two-photon microscopy an intrinsic three-dimensional sectioning ability similar to that of confocal microscopy. A demonstration of this is presented in figure 1.3 [17]. This figure shows a solution of fluorescein undergoing one-photon fluorescence on the left and two-photon fluorescence on the right. Note that in the one-photon case, a significant amount of fluorescence signal is generated from areas outside of the focus; however, in the two-photon case, fluorescence only occurs in a small area around the focus.

When implemented in a laser scanning microscope, this natural sectioning behavior makes it possible to acquire images with strong signal and low background. It also has implications for the ability to image deep into tissues. The elimination of unwanted signal from out-of-focus areas means that signal quality is not degraded by background as imaging depth increases. In addition, the use of pulsed laser excitation to generate the high peak intensities required means that average beam power can remain low, reducing the chance of photobleaching or photodamage in sample areas outside of the focus [15]. With two-photon microscopy, images have been recorded from as deep as 500 μm in biological samples [2]. Two-photon excitation has other benefits that make it a useful tool for biological imaging. The longer wavelength light used for excitation in two-photon microscopy undergoes less scattering in tissues, is less damaging because of its lower energy, and is less absorbed than lower wavelengths [2].

As a result of these benefits, two-photon microscopy has been widely implemented in biological studies. It does have downsides, however. A particular challenge has been the implementation of multicolor two-photon microscopy. Although fluorescent probes exist across the visible spectrum, both as synthetic dyes and increasingly as fluorescent proteins that can be natively expressed by the sample, adding more colors requires adding more excitation wavelengths and/or more channels in detection. A handful of methods have been implemented to perform two-color imaging, mostly relying on simultaneous excitation. One method is to use a single excitation wavelength with fluorophores whose Stokes shifts are large enough that the two fluorescent signals can be split into separate detection channels by filters [21, 22]. A recent discovery that some red fluorescent proteins have large, unexpected increases in their two-photon excitation spectra at shorter wavelengths [23, 24] also makes it possible to use a single excitation wavelength and filters to separate the signal [25].

Moving on to three-color imaging or imaging with selective excitation of individual

fluorophores present in the sample is even more challenging, as multiple excitation wavelengths are needed. One solution to this is the use of tunable femtosecond lasers [26]; however, the use of this method is limited to systems with low time resolution that can accommodate the seconds to minutes it takes to tune the laser. Another option is the use of ultrabroadband lasers with bandwidths of 100 nm or more. However, the spectra of these lasers will generally overlap with the two-photon excitation spectra of multiple fluorophores [24], meaning that all fluorophores are excited without any selectivity. A final set of methods uses multiple laser beams overlapping in the setup to perform the different excitations [26, 27], but these methods rely on complicated alignments and have higher costs due to the multiple lasers involved.

An additional challenge in two-photon microscopy experiments is that it can be difficult to obtain quantitative results. Fluorescence Resonance Energy Transfer (FRET) is a standard microscopic technique that has been successfully applied with two-photon excitation. It can provide beautiful images and can keep track of system motion and interaction in a qualitative way, but quantitative results are lacking. Several methods have been proposed based on both one- and two-photon microscopy to learn more, but they fall short of true stoichiometric information. A notable exception is the development of FRET stoichiometry by Hoppe *et al.* [28] which yields quantitative information about an interacting system based on microscope images. However, this has not been implemented for two-photon microscopy due to the challenges described above of performing selective, multicolor excitation.

The work described in this thesis aims to resolve these problems and improve the utility of two-photon microscopy by implementing ultrafast pulse shaping. Pulse shaping makes it possible to tailor the laser pulses used for fluorescence excitation to achieve desired results, including the selective excitation of certain fluorophores over others present in the sample [29] and the suppression of unwanted autofluorescence signal [30]. This opens the door to performing rapid multicolor imaging in biological

samples in addition to implementing FRET stoichiometry to achieve quantitative results. This thesis demonstrates the application of pulse shaping to linear unmixing for three-color two-photon microscopy in live cells [31]. It also demonstrates two-photon FRET [32, 33] and generalizes the theory of one-photon FRET stoichiometry to the two-photon case. Finally, it presents preliminary two-photon FRET stoichiometry results and discusses future directions for improving the method. A chapter outline of this work is presented below.

Chapter II provides a comprehensive overview of the ultrafast pulse shaping methods used in this work. The development of the method and its applications to biological imaging are reviewed, and the basic setup needed to perform the experiments is described. The theory supporting the application of pulse shaping methods to two-photon excited fluorescence is discussed along with pulse shape design considerations. Simulations of different pulse shaping methods are presented to motivate the choice of a specific technique, and an important application of pulse shaping methods to dispersion compensation is discussed.

Chapter III describes the application of pulse shaping methods to three-color two-photon fluorescence microscopy via linear unmixing techniques [31]. The challenges of performing such multicolor imaging with standard methods are discussed, and the use of linear unmixing is motivated. The theory of linear unmixing based on fluorescence image intensities recorded with selective excitation is derived. The experimental setup and results are presented and discussed, and potential future applications and extensions of the method are proposed.

Chapter IV begins with a review of the history and theory of Fluorescence Resonance Energy Transfer, as well as its application in microscopy. An experimental method for the detection of FRET using ultrafast pulse shaping in live-cell samples is presented and the results are discussed [32, 33].

In Chapter V the FRET stoichiometry technique is introduced with a focus on the

existing theory for one-photon microscopy. The changes required when transitioning to two-photon FRET stoichiometry are discussed and a new, entirely general theory for two-photon FRET stoichiometry is derived. Finally, current experimental results from the application of two-photon FRET stoichiometry are presented and avenues for future work are outlined.

Finally, Chapter VI reviews the work presented in this thesis. Future possibilities in the field of applications of ultrafast pulse shaping to two-photon fluorescence microscopy are discussed.

References

- [1] E. Keller and R. D. Goldman. Light microscopy. In D. L. Spector and R. D. Goldman, editors, *Basic Methods in Microscopy: Protocols and Concepts from Cells: a Laboratory Manual*, chapter 1, pages 1–42. Cold Spring Harbor Laboratory Press, 2006.
- [2] J. Mertz. *Introduction to Optical Microscopy*. Roberts and Company Publishers, 2010.
- [3] A. H. Coons and M. H. Kaplan. Localization of antigen in tissue cells ii. improvements in a method for the detection of antigen by means of fluorescent antibody. *The Journal of Experimental Medicine*, 91(1):1–13, 1950.
- [4] K. Berland. Basics of fluorescence. In A. Periasamy, editor, *Methods in Cellular Imaging*, Methods in Physiology Series, chapter 1, pages 5–19. American Physiological Society, 2001.
- [5] J. R. Lakowicz. *Principles of Fluorescence Spectroscopy*. Springer, 2007.
- [6] J. M. Murray. Confocal microscopy, deconvolution, and structured illumination methods. In D. L. Spector and R. D. Goldman, editors, *Basic Methods in Microscopy: Protocols and Concepts from Cells: a Laboratory Manual*, chapter 2, pages 43–81. Cold Spring Harbor Laboratory Press, 2006.
- [7] J. J. Lemasters, T. Qian, D. R. Trollinger, B. J. Muller-Borer, S. P. Elmore, and W. C. Cascio. Laser scanning confocal microscopy applied to living cells and tissues. In A. Periasamy, editor, *Methods in Cellular Imaging*, Methods in Physiology Series, chapter 5, pages 66–87. American Physiological Society, 2001.
- [8] M. Minsky. Microscopy apparatus, 1961.
- [9] J. Squier and M. Muller. High resolution nonlinear microscopy: A review of sources and methods for achieving optimal imaging. *Review of Scientific Instruments*, 72(7):2855–2867, 2001.
- [10] W. Min, C. W. Freudiger, S. Lu, and X. S. Xie. Coherent nonlinear optical imaging: beyond fluorescence microscopy. *Annual Review of Physical Chemistry*, 62:507–530, 2011.

- [11] S. W. Hell, K. Bahlmann, M. Schrader, A. Soini, H. M. Malak, I. Gryczynski, and J. R. Lakowicz. Three-photon excitation in fluorescence microscopy. *Journal of Biomedical Optics*, 1(1):71–74, 1996.
- [12] M. Göppert-Mayer. Über elementarakte mit zwei quantensprüngen. *Annalen der Physik*, 401(3):273–294, 1931.
- [13] B. R. Masters. English translations of and translator’s notes on Maria Goppert-Mayer’s theory of two-quantum processes. In B. R. Masters and P. T. C. So, editors, *Handbook of Biomedical Nonlinear Optical Microscopy*, chapter 4, pages 42–84. Oxford University Press, 2008.
- [14] W. Kaiser and C. G. B. Garrett. Two-photon excitation in $\text{CaF}_2:\text{eu}^{2+}$. *Physical Review Letters*, 7(6):229–231, Sep 1961.
- [15] W. Denk, D. W. Piston, and W. W. Webb. Two-photon molecular excitation in laser-scanning microscopy. In James B. Pawley, editor, *Handbook of Biological Confocal Microscopy*, chapter 28, pages 445–458. Plenum Press, 1995.
- [16] P. T. C. So, K. H. Kim, C. Buehler, B. R. Masters, L. Hsu, and C. Dong. Basic principles of multiphoton excitation microscopy. In A. Periasamy, editor, *Methods in Cellular Imaging*, Methods in Physiology Series, chapter 9, pages 147–161. American Physiological Society, 2001.
- [17] W. R. Zipfel, R. M. Williams, and W. W. Webb. Nonlinear magic: multiphoton microscopy in the biosciences. *Nature Biotechnology*, 21(11):1369–1377, 2003.
- [18] B. R. Masters and P. T. C. So. Classical and quantum theory of one-photon and multiphoton fluorescence spectroscopy. In B. R. Masters and P. T. C. So, editors, *Handbook of Biomedical Nonlinear Optical Microscopy*, chapter 5, pages 91–152. Oxford University Press, 2008.
- [19] W. Denk. Two-photon excitation in functional biological imaging. *Journal of Biomedical Optics*, 1(3):296–304, 1996.
- [20] W. Denk, J. H. Strickler, and W. W. Webb. Two-photon laser scanning fluorescence microscopy. *Science*, 248(4951):73–76, 1990.
- [21] E. Sahai, J. Wyckoff, U. Philippar, J. E. Segall, F. Gertler, and J. Condeelis. Simultaneous imaging of gfp, cfp, and collagen in tumors in vivo using multiphoton microscopy. *BMC Biotechnology*, 5(14), 2005.
- [22] H. Kawano, T. Kogure, Y. Abe, H. Mizuno, and A. Miyawaki. Two-photon dual-color imaging using fluorescent proteins. *Nature Methods*, 5(5):373–374, May 2008.
- [23] M. Drobizhev, N. S. Makarov, T. Hughes, and A. Rebane. Resonance enhancement of two-photon absorption in fluorescent proteins. *The Journal of Physical Chemistry B*, 111(50):14051–14054, 2007.

- [24] M. Drobizhev, N. S. Makarov, S. E. Tillo, T. E. Hughes, and A. Rebane. Two-photon absorption properties of fluorescent proteins. *Nature Methods*, 8(5):393–399, May 2011.
- [25] S.E. Tillo, T.E. Hughes, N.S. Makarov, A. Rebane, and M. Drobizhev. A new approach to dual-color two-photon microscopy with fluorescent proteins. *BMC Biotechnology*, 10(6), 2010.
- [26] D. Entenberg, J. Wyckoff, B. Gligorijevic, E. T. Roussos, V. V. Verkhusha, J. W. Pollard, and J. Condeelis. Setup and use of a two-laser multiphoton microscope for multichannel intravital fluorescence imaging. *Nature Protocols*, 6(10):1500–1520, October 2011.
- [27] P. Mahou, M. Zimmerley, K. Loulier, K. S. Matho, G. Labroille, X. Morin, W. Supatto, J. Livet, D. Debarre, and E. Beaurepaire. Multicolor two-photon tissue imaging by wavelength mixing. *Nature Methods*, 9(8):815–818, August 2012.
- [28] A. Hoppe, K. Christensen, and J. A. Swanson. Fluorescence resonance energy transfer-based stoichiometry in living cells. *Biophysical Journal*, 83(6):3652–3664, 2002.
- [29] V. V. Lozovoy, I. Pastirk, K. A. Walowicz, and M. Dantus. Multiphoton intrapulse interference. ii. control of two- and three-photon laser induced fluorescence with shaped pulses. *The Journal of Chemical Physics*, 118(7):3187–3196, 2003.
- [30] J. P. Ogilvie, D. Débarre, X. Solinas, J. Martin, E. Beaurepaire, and M. Joffre. Use of coherent control for selective two-photon fluorescence microscopy in live organisms. *Optics Express*, 14(2):759–766, 2006.
- [31] M. H. Brenner, D. Cai, J. A. Swanson, and J. P. Ogilvie. Two-photon imaging of multiple fluorescent proteins by phase-shaping and linear unmixing with a single broadband laser. *Optics Express*, 21(14):17256–17264, Jul 2013.
- [32] M. H. Brenner, D. Cai, S. R. Nichols, S. W. Straight, A. D. Hoppe, J. A. Swanson, and J. P. Ogilvie. Pulse shaping multiphoton fret microscopy. In *SPIE BiOS*. International Society for Optics and Photonics, 2012.
- [33] M. H. Brenner, D. Cai, S. W. Straight, J. A. Swanson, and J. P. Ogilvie. Pulse-shaping-based two-photon fret microscopy. In *EPJ Web of Conferences*, volume 41, page 11009. EDP Sciences, 2013.

CHAPTER II

Pulse Shaping

2.1 Introduction

Recently, many advances have been made in applications of two-photon microscopy to biological systems. This is due in large part to the fact that it has several unique advantages for tissue imaging, particularly its increased penetration depth and decreased photobleaching [1–3]. The surge in two-photon microscopy studies has contributed to an increase in the development of novel fluorescent proteins. Starting with the isolation of Green Fluorescent Protein (GFP) [4], a library of fluorescent proteins with a range of emission spectra and other photophysical properties now exist for application in various biological samples [5]. As fluorescent proteins cover more and more of the visible spectrum, multicolor two-photon microscopy experiments are becoming more common. However, these can often be difficult to implement due to problems in spectral and temporal resolution. Tunable titanium:sapphire (ti:sapph) oscillators are a popular choice for excitation in two-photon fluorescence microscopy studies [6]; however, they typically have narrow spectra (on the order of 10 nm) and can excite one fluorophore at a time. Multicolor imaging then requires tuning the laser, which can involve relatively long tuning times of seconds to minutes. This limits the researcher to studies that do not require faster timescales. It is also possible to use ultrabroadband oscillators with bandwidths on the order of 100 nm; while these

will excite multiple fluorophores, they will all be excited simultaneously, which may not be ideal for all experimental conditions [7].

The development of such ultrabroadband sources raises the possibility of ultrafast pulse shaping as a potential solution to the challenges of performing multicolor two-photon microscopy. As laser pulse durations have shortened and their spectral bandwidths have increased, pulse shaping methods to manipulate this bandwidth have proliferated. In particular, it is possible to adjust the interactions between different frequency components of the pulse to achieve specific desired results. Applications have been developed in a number of diverse fields including fiber optical communications, laser pulse compression and characterization, and control of quantum mechanical processes [8–10]. Notable work in the demonstration of pulse shaping for quantum coherent control has been performed by Meshulach and Silberberg [11–13]. By shaping a femtosecond pulse, they were able to control two-photon transitions in cesium. They observed the creation of “dark pulses” which eliminated the transitions, as well as shapes that could induce transitions nearly as efficiently as unshaped pulses [11–13].

Moving beyond relatively simple atomic systems, a number of experiments have been performed investigating applications of pulse shaping to fluorescent systems. A series of experiments by Tkaczyk and colleagues have demonstrated the utility of pulse shaping for selective excitation of fluorescent dyes [14, 15]. Using solutions of dyes popular in biological studies, they demonstrated that tailoring the shape of ultrafast pulses enabled relative enhancement or suppression of fluorescence from one fluorophore compared to another (alone or in complex with other biological structures), and compared to second harmonic generation signal [14]. This method also demonstrated the use of a genetic algorithm to identify the optimal pulse shapes. An extension of this work found that pulse shaping can be used to distinguish two fluorescent dyes in two-photon excited fluorescence that cannot easily be differentiated

by one-photon measurements; this method was even able to quantify the amount of each fluorophore present in a mixed solution [15].

Continuing the development of applications of pulse shaping, a variety of studies have been performed in microscopy. Dudovich *et al.* demonstrated the use of pulse shaping to perform single-pulse Coherent Anti-Stokes Raman Scattering (CARS) microscopy with high spectral resolution [16], showing that pulse shaping is not limited to fluorescence techniques. An early demonstration by Pastirk *et al.* [17] used pulse shaping to perform selective excitation of polymethylmethacrylate (PMMA) samples doped with two different synthetic fluorophores; images of the spatially distinct PMMA samples showed that different shapes successfully excited the different PMMA regions. A later study from the same group showed that pulse shapes could be used to image and identify regions of a pH-sensitive dye under different pH conditions [18]. An elegant demonstration in live biological tissues was performed by Ogilvie *et al.* [19]. Two pulse shapes were designed to perform selective excitation in *Drosophila* embryos, with one shape designed to excite enhanced Green Fluorescent Protein and one designed to excite the endogenous autofluorescence present in the yolk of the embryo. This study found that the use of pulse shaping for selective excitation improved fluorescence contrast by a factor of approximately 3 compared to using excitation filters [19]. A continuation of this work utilized a fast scanning mirror to alternate between the pulse shapes, improving the temporal resolution [20]. Further work in biological samples includes selective excitation of fluorophores in sections of mouse kidney tissue [21], and of fluorescent proteins in HeLa cells [22].

The number of potential applications of ultrafast pulse shaping to two-photon fluorescence microscopy of biological systems is large. The technique is particularly useful in situations requiring selective excitation, such as the applications to three-color fluorescence imaging and Fluorescence Resonance Energy Transfer (FRET) microscopy described in chapters III, IV, and V. As a foundation, this chapter outlines

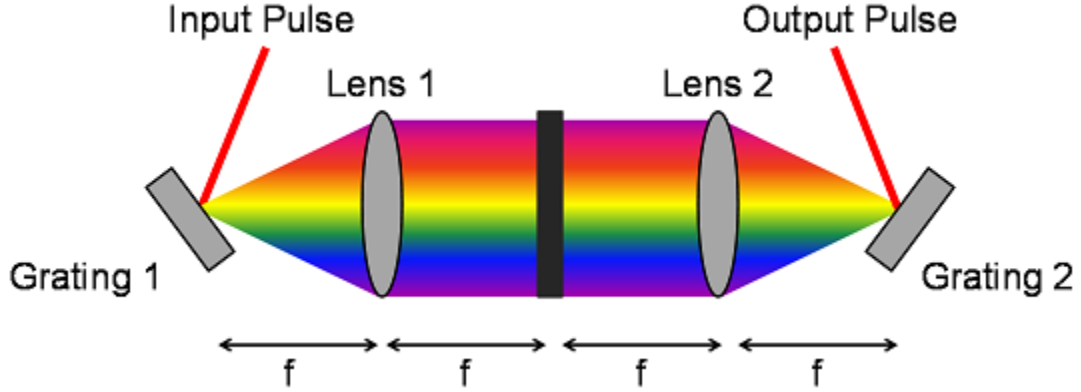


Figure 2.1: Diagram of a 4f pulse shaper. The input beam is spatially dispersed via a grating and lens onto the shaping mask located at the back focal plane of the lens, represented here by the black rectangle. The spectrum is then recombined as a shaped pulse. Figure adapted from [9].

the methodology behind 4f pulse shapers, one of the most widely-used ultrafast pulse shaping techniques and the one used in the studies presented in this thesis. The theory of pulse shaping as applied to two-photon fluorescence is discussed, as well as considerations in pulse shape design and important applications to dispersion compensation.

2.2 Basics of 4f Pulse Shaping

Although a variety of pulse shaping methods exist, the most widely used is Fourier transform pulse shaping [10]. This method relies on spatially dispersing the spectrum of the laser pulse so that its individual frequency components can be manipulated independently. The most common experimental setup for this is a 4f shaper, first proposed by Froehly *et al.* in 1983 [8–10, 23]. This is illustrated in figure 2.1, adapted from [9]. In the 4f shaper, the first grating disperses the frequency components of the input pulse. The lens then focuses the beam onto the pulse shaping mask placed at its back focal plane such that the different frequencies are spatially separated across the mask. After the desired manipulation by the mask, a second lens and grating are used to recombine the frequency components into a collimated beam with a shaped

output pulse [8–10]. The name “4f pulse shaper” comes from the fact that the setup comprises four focal lengths of the lenses used; however, it is also known as a “zero dispersion pulse shaper” [8–10]. This is because for the method to work correctly, no temporal dispersion should be introduced by the setup in the absence of a pulse shaping mask. This ensures that the setup is not causing unintended changes to the phases of the frequency components. When the gratings are placed one focal length from the lenses, the setup acts as a one-to-one magnification telescope and the output beam is unchanged from the input beam, adding no temporal dispersion [8–10].

Two important modifications to this setup exist and are commonly implemented. The first is that the use of ultrashort pulses with durations of a few tens of femtoseconds enhances unwanted effects from the optics in the setup. The lenses in particular can contribute unwanted aberrations or chromatic dispersion; to eliminate this, the lenses are replaced with spherical mirrors [9, 10, 24]. A second possible modification is to place a mirror behind the pulse shaping mask so that the dispersed beam is reflected back through the first lens and grating rather than using a second set [10, 25]. Because this requires fewer optical components, it simplifies the alignment of the setup.

Several options exist for the pulse shaping masks to be placed in the 4f setup; a key decision is whether to make them fixed or variable. Fixed masks have been used successfully in a number of experiments, particularly in fiber optics, but they make it challenging to use continuous functions for pulse shaping and have to be created for each experimental condition [9]. With the advent of computer-controlled variable pulse shapers, and because of the limitations of fixed masks, spatial light modulators (SLMs) have become the method of choice for creating pulse shaping masks. SLMs consist of arrays of pixels made of nematic liquid crystals, which are cylindrical in shape and align with their long axes pointing in the same direction in the absence of an applied electric field. This is defined as the optic axis. These

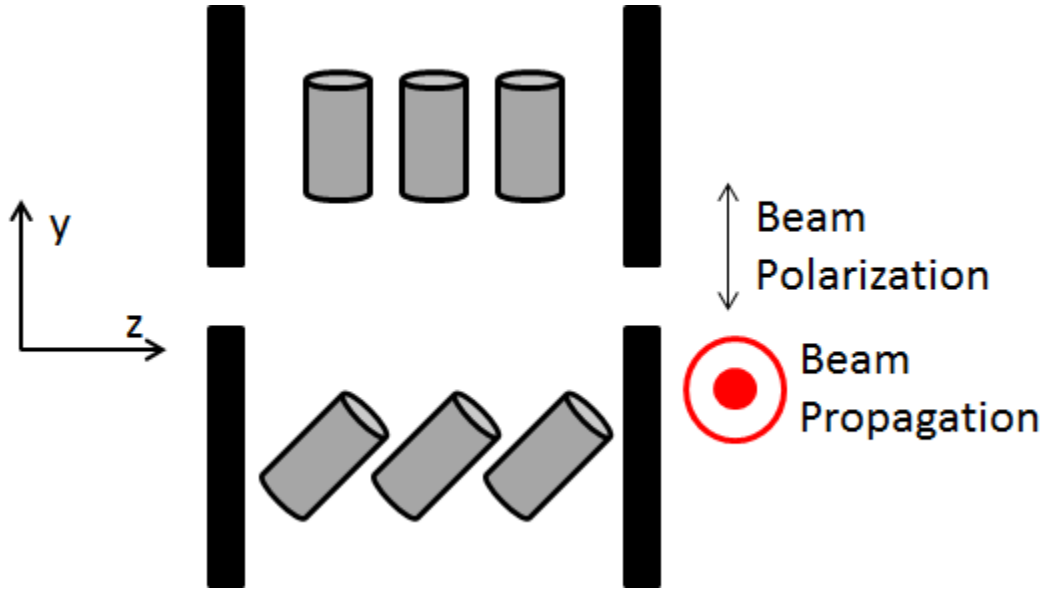


Figure 2.2: Schematic of the liquid crystal structure in an SLM. The top panel shows the SLM with no voltage applied; the crystals are aligned along the y -axis. The input laser beam is propagating out of the page along the x -axis but is linearly polarized along the y -axis. As voltage is applied across the SLM, the crystals rotate to align along the z -axis, changing the effective index of refraction and thus the phase. Adapted from [10].

crystals are birefringent, so they have two different indices of refraction depending on the polarization of the input light - light polarized parallel to the optic axis (and perpendicular to the direction of propagation) sees a larger index of refraction than light polarized perpendicular to both the optic axis and direction of propagation. A schematic illustration of the liquid crystals in an SLM is shown in figure 2.2, adapted from [10]. The top panel of the figure illustrates the SLM with no voltage applied, so the crystals are aligned along the y -axis. The input beam is polarized along this axis and is propagating out of the page along the x -axis. In the bottom panel, as the voltage is applied to the SLM, the crystals rotate such that they stay in the same plane but align more along the z axis than the y axis. This means that the crystals are no longer parallel to the polarization of the light and the index of refraction is reduced; this in turn changes the phase of the light transmitted through the SLM [10]. Since the applied electric field at each pixel is controlled independently and the laser

spectrum is dispersed across the pixels, it is possible to control the phase of individual frequency components of the pulse. Common SLMs have one-dimensional arrays of 128 or 640 pixels, with center-to-center pixel spacing on the order of 100 μm and gaps between pixels on the order of a few μm [10]. The time to change applied masks in the SLM is limited by the response time of the liquid crystal itself in addition to the electronics used, and switching times on the scale of milliseconds are common [9, 10].

An additional factor in the design of pulse shaping experiments is whether to shape the pulse in amplitude, phase, or both. Amplitude shaping relies on physically reducing the transmission of certain frequency components through the mask, potentially even blocking some entirely. Phase shaping leaves all frequencies in the pulse intact, and instead changes the relative phases between them. Both can be performed with SLMs, but simultaneous control of both requires a dual-mask SLM [9, 10]. Phase shaping has been shown to have unique benefits compared to amplitude shaping when applied to two-photon absorption processes, including improved signal amplitude [26], and as a result is the focus of the rest of this thesis. The next section outlines the application of phase shaping for manipulation of two-photon fluorescence and more closely considers the differences between phase and amplitude shaping.

2.3 Phase Shaping for Two-Photon Fluorescence

To understand the role of phase in shaping femtosecond pulses, it is helpful to consider theoretically the case of two-photon absorption. This is particularly relevant for applications of phase shaping to two-photon fluorescence microscopy, as the fluorophores are excited via absorption of two photons. The derivation of the two-photon absorption rate was originally published by Maria Goppert-Mayer in 1931 [27], and since then it has been summarized several times in the literature, including a thorough treatment by Boyd [28]. Meshulach and Silberberg [11–13, 29] laid out a slightly different version of the derivation that better emphasizes the role of phase-

shaped pulses in the process. This version of the derivation has been summarized in numerous other works investigating the role of phase shaping in two-photon processes and is briefly reviewed here following the explanation of Brixner *et al.* [30]. It considers a two-level system being excited by an ultrashort pulse from the ground state $|g\rangle$ to its final state $|f\rangle$ via a set of intermediate states $|n\rangle$. The pulse complex electric field in time is given by $E(t)$ and is non-resonant with any real intermediate or final states of the system. For these conditions, second order time-dependent perturbation theory yields for the amplitude a_f of the excited state [11, 29, 30]:

$$a_f = -\frac{1}{\hbar^2} \sum_n \mu_{fn} \mu_{ng} \int_{-\infty}^t \int_{-\infty}^{t_1} E(t_1) E(t_2) \exp(i\omega_{fn} t_1) \exp(i\omega_{ng} t_2) dt_2 dt_1 \quad (2.1)$$

In this equation, μ_{fn} and μ_{ng} are the dipole moment matrix elements between the final and intermediate states and intermediate and ground states respectively, and t_1 and t_2 are dummy time variables. $\omega_{fn} = (E_f - E_n)/\hbar$ and $\omega_{ng} = (E_n - E_g)/\hbar$ where E_f , E_n , and E_g are the energies of the final, intermediate, and ground states. Because the system is nonresonant, this can be rewritten as [29]

$$a_f = -\frac{1}{\hbar^2} \sum_n \frac{\mu_{fn} \mu_{ng}}{\omega_{ng} - \omega/2} \int_{-\infty}^{\infty} \tilde{E}(\Omega) \tilde{E}(\omega - \Omega) d\Omega \quad (2.2)$$

where $\tilde{E}(\Omega)$ is the Fourier transform of $E(t)$. This is the amplitude of the excited state, so the probability $p_{TPA}(\omega)$ can be found from $|a_f|^2$ [11, 12, 29, 30]:

$$p_{TPA}(\omega) = \frac{1}{\hbar^4} \left| \sum_n \frac{\mu_{fn} \mu_{ng}}{\omega_{ng} - \omega/2} \right|^2 \left| \int_{-\infty}^{\infty} \tilde{E}(\Omega) \tilde{E}(\omega - \Omega) d\Omega \right|^2 \quad (2.3)$$

This equation has the form of $p_{TPA}(\omega) = g_{TPA}(\omega)S_2(\omega)$, where [30]

$$g_{TPA}(\omega) = \frac{1}{\hbar^4} \left| \sum_n \frac{\mu_{fn}\mu_{ng}}{\omega_{ng} - \omega/2} \right|^2 \quad (2.4)$$

$$S_2(\omega) = \left| \int_{-\infty}^{\infty} \tilde{E}(\Omega)\tilde{E}(\omega - \Omega)d\Omega \right|^2 \quad (2.5)$$

If the excitation occurs into a distribution of final states with a spectra density of states $\rho(\omega)$, then the probability is given as the integral over the excitation probabilities to the individual sublevels [30] so that

$$p_{TPA} \approx \int g_{TPA}(\omega)\rho(\omega)S_2(\omega)d\omega \quad (2.6)$$

It should be noted that the term $g_{TPA}(\omega)\rho(\omega)$ here is directly related to the two-photon cross section, differing only by constants depending on the notation and units being used [28, 31].

For phase shaping, the term of interest is S_2 , the second order electric field spectrum [19, 20, 31]. This term contains the trademark E^2 dependence of two-photon absorption, which leads to the benefits for microscopy already discussed. To better show how phase shaping works, the electric field $\tilde{E}(\Omega)$ can be expanded as $\tilde{E}(\Omega) = A(\Omega)\exp[i\Phi(\Omega)]$ where $A(\Omega)$ and $\Phi(\Omega)$ are the spectral amplitude and spectral phase, respectively. It is also helpful to look at this term in slightly different notation, which emphasizes how the photons can combine. Now [32, 33]

$$S_2(\omega) = \left| \int_{-\infty}^{\infty} A(\omega/2 + \Omega)A(\omega/2 - \Omega)\exp[i(\Phi(\omega/2 + \Omega) + \Phi(\omega/2 - \Omega))]d\Omega \right|^2 \quad (2.7)$$

Thus, two photons centered around half the desired transition frequency ω can sum to reach the total frequency needed: $(\omega/2 + \Omega) + (\omega/2 - \Omega) = \omega$.

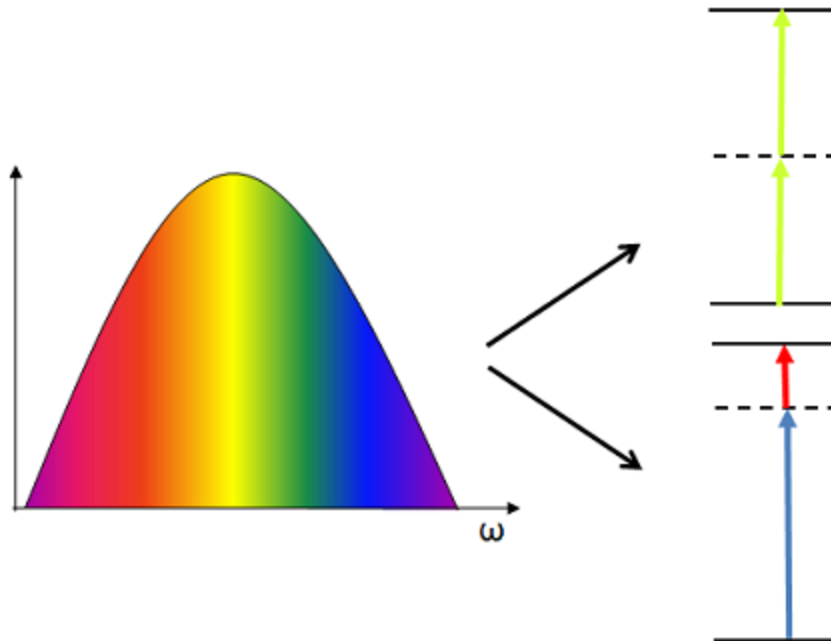


Figure 2.3: Example of photon combinations in two-photon absorption. The left shows the spectrum of a hypothetical Gaussian ultrashort pulse which contains many frequency components. The right shows two possible combinations of frequencies from this pulse that have the required energy to excite the system from its ground state to its final state. One option is two photons, both with half the necessary frequency. However, this same gap can be bridged with any two photons with frequencies that sum to the required total frequency. Adapted from [13].

This expanded equation for S_2 has some features of interest. The first is that there is an explicit dependence on the spectral phase. Thus, changes to the spectral phase function $\Phi(\omega)$ - such as those introduced by the SLM to different frequency components - directly affect S_2 and thus the transition probability [11–13, 30]. Furthermore, equation (2.7) demonstrates that all frequency components in the pulse can combine in the appropriate pairs to make the two-photon transition take place [11–13]. An example of this is shown in figure 2.3, where two such potential combinations are shown - one consisting of two photons of the same frequency, and the other consisting of two photons of different frequencies but which sum to the same final value. This realization that all frequencies present can contribute to two-photon absorption is critical to phase shaping. Pulses that are short in time, such as those used in pulse shaping,

contain many frequency components according to the time-bandwidth product. The manipulation of the phases of these components via pulse shaping leads to a process called Multiphoton Intrapulse Interference (MII) [31]. In MII, the phases applied to each frequency are chosen so that they constructively or destructively interfere when they combine for two-photon absorption [31, 34]. That is, the phases in equation (2.7) are chosen such that the exponential term is maximized or minimized.

MII was originally thought to apply only to systems such as atomic ones with sharp resonances [31]; the method was in fact elegantly demonstrated in cesium, just such an atomic system [11, 12]. However, it was subsequently shown that this is not the case, and MII can be implemented in systems that lack sharp resonances such as large dye molecules in solution [31]. In the case of two-photon excited fluorescence, the signal is proportional to equation (2.6) [14, 18, 20, 30, 31, 35], which accounts for both the second order electric field spectrum as well as the two-photon absorption cross-section of the fluorophore. Consequently, manipulation of the spectral phase via pulse shaping has a direct effect on the fluorescent signal from the system, opening the door for the use of MII via phase shaping in biological systems.

There are a number of experimental factors that must be considered when implementing this method, the first of which is how the effects of MII can be adequately measured in the laboratory. One common technique is the use of second harmonic generation (SHG) to view the effective spectra of the shaped pulses. Because the equations for the second harmonic (SH) spectrum and two-photon fluorescence signal both depend on the square of the electric field of the input pulse, they share similar functional forms, particularly the same spectral phase dependence [20, 30, 36, 37]. Consequently, changes to the pulse shape designed to affect the two-photon excited fluorescence will also affect the SHG intensity. This provides a straightforward method for testing different pulse shapes, as the SHG spectrum can be easily recorded.

Another important consideration is the phase function $\Phi(\omega)$ to apply. The sim-

plest case is a flat spectral phase, where $\Phi(\omega) = 0$ for each frequency component in the pulse. This yields a transform-limited (TL) pulse, so called because it has the shortest possible duration in time. Looking at equation (2.7), it is evident that for the situation of the flat spectral phase S_2 is maximized, leading to maximum two-photon fluorescence [11, 12]. An additional case is the use of phase functions that are antisymmetric about a specific frequency $\omega/2$. For antisymmetric functions,

$$\Phi(\omega/2 + \Omega) = -\Phi(\omega/2 - \Omega) \quad (2.8)$$

Again referring to equation (2.7), it can be seen that for antisymmetric phase functions, the exponential terms cancel and the two-photon fluorescence signal is again maximized [11, 12]. Aside from these two special cases, there are many potential phase functions - since the SLM is capable of gray-level phase control, continuous as well as discontinuous functions can be applied. Many early studies were performed with sinusoidal phase functions, including the initial demonstration in cesium [11] and the first study on dye molecules in solution [31]. Later studies modified the sinusoidal phase function by adding quadratic or cubic components [32] or even amplitude shaping [18]; cubic phase functions alone have been used as well [20].

An important class of phase masks are binary phase masks. In these, the phase value at all frequency components is either zero or pi. Early work looked at the effect of binary masks used in communication theory to investigate control of SHG [36, 37]. This type of binary shaping was extended to the control of two-photon fluorescence by Comstock *et al.* [26]. The utility of binary masks can be understood by symmetry arguments. It has already been established that a phase function that is antisymmetric about a certain frequency leads to maximized two-photon fluorescence excitation at twice that frequency, and because they share the same spectral phase dependence, this will also lead to maximum SHG intensity at the same doubled

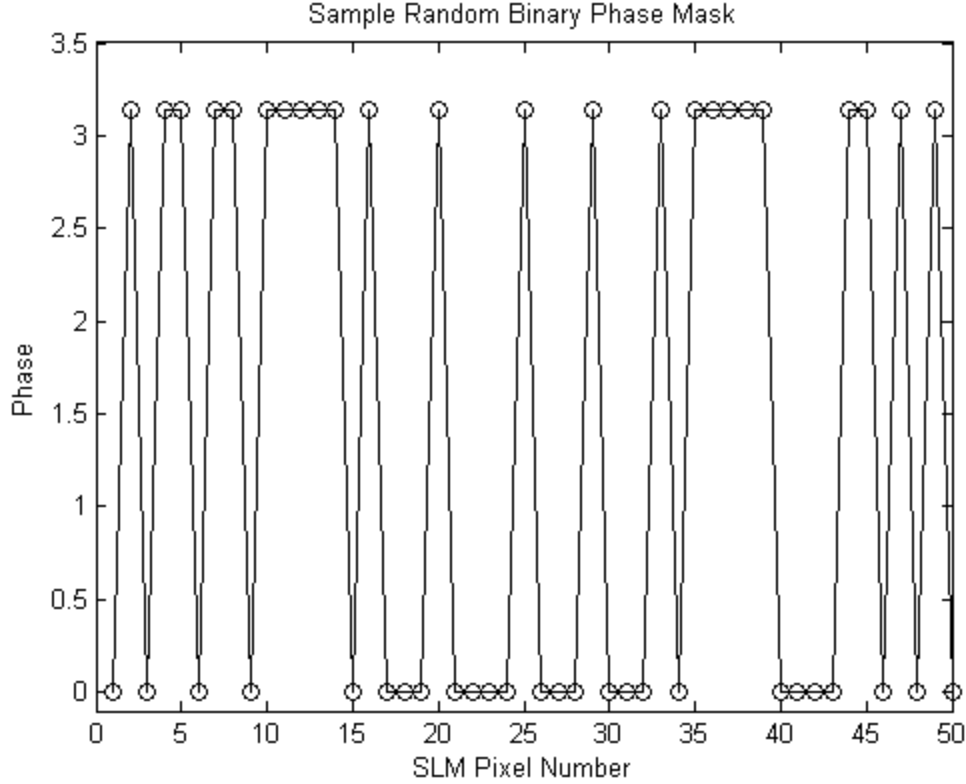


Figure 2.4: Section of a random binary phase mask. The phase switches between zero and pi at each pixel on the SLM, following a random pattern.

frequency. However, when the phases are only zero or pi, symmetric phase functions will also lead to constructive interference and maximized signal [26]. This can be seen again in the interference term of equation (2.7) - if both phases are either 0 or pi, the exponent is maximized. A section of a random binary phase mask, demonstrating the switching between zero and pi phases on the SLM pixels, is shown in figure 2.4. An additional desired feature is the ability to reduce the SHG intensity or effective two-photon fluorescence excitation in different regions of the spectrum. By designing the binary phase mask such that it is symmetric about the desired center frequency but asymmetric elsewhere across the spectrum, constructive interference will occur at the center but destructive interference will occur elsewhere [26]. The result is a shaped pulse which provides selective two-photon fluorescence excitation (or SHG intensity) in one region of the spectrum but little to none elsewhere. To achieve

selective excitation, phase masks are designed with a central flat phase region of a certain width, with symmetric random or semi-random patterns of zero and pi on either side. The first work was performed with prime number masks, where a switch between zero or pi phase occurred at every prime numbered SLM pixel [26]. For example, the mask could start with zero phase at the first pixel, switch to pi phase at the second pixel, switch back to zero phase at pixels three and four, switch to pi phase at pixels five and six, and so on for the desired length. The mask would then have its central flat phase section, followed by the mirror image of the binary phase section. This study found that the use of binary phase masks improved contrast between the desired central peak and unwanted background areas of the spectrum by a factor of 6 compared to sinusoidal phase masks [26]. It also demonstrated that the pulse shape can be tuned by adjusting the phase mask - the peak can be shifted by moving the center frequency of the flat phase section [26], and the width of the peak changes with the width of the flat phase section.

An example of a random binary phase mask and its resulting SHG spectrum found experimentally is shown in figure 2.5. The top panel shows the fundamental laser spectrum with the phase mask overlaid; the phase mask has a flat phase section of approximately 40 nm centered at approximately 836 nm. The bottom panel shows the resulting second harmonic spectra. The black dashed line is the SH from the unshaped, TL pulse; the blue line shows the SH from the shaped pulse. Note that the peak of the shaped SH spectrum is at approximately half the wavelength of the center of the flat phase portion of the phase mask. A demonstration of the tuning ability of such phase shaping is shown in figure 2.6. It is evident that shifting the phase mask allows the creation of shaped pulses across the spectrum. This flexibility in designing shaped pulses with large peaks in two-photon excitation at specific wavelengths and little to no excitation elsewhere is what makes binary phase shaping such a powerful tool for selective excitation of fluorophores in multicolor two-photon microscopy.

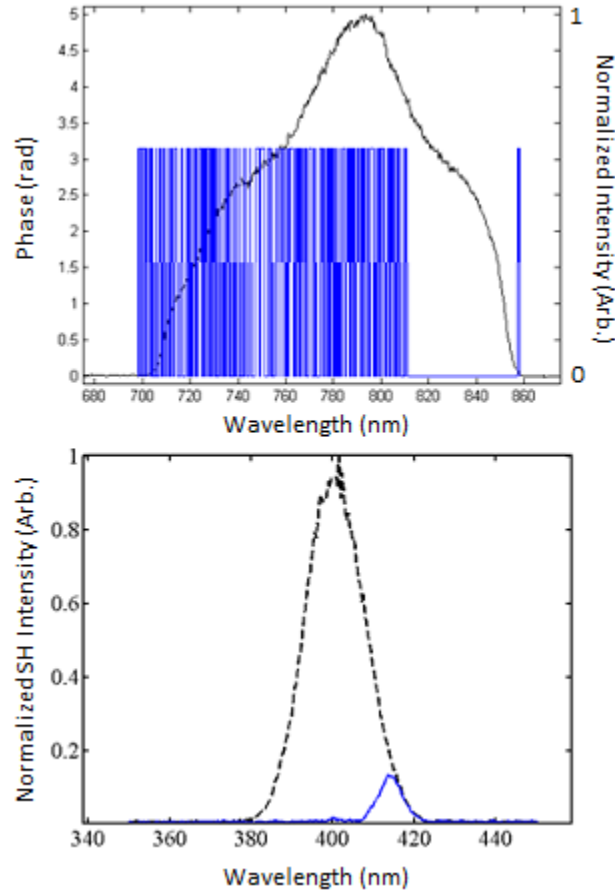


Figure 2.5: Example of random binary phase shaping. The top panel shows the random binary mask with a central flat phase section of 40 nm, centered at 836 nm, overlaid on the fundamental spectrum of the laser. The bottom panel shows the resulting SHG spectra. The black dashed line illustrates the unshaped second harmonic from the TL pulse, and the blue line shows the shaped spectrum resulting from application of the phase mask. Note that the shaped SH is centered at approximately half the wavelength of the center of the flat phase section of the phase mask.

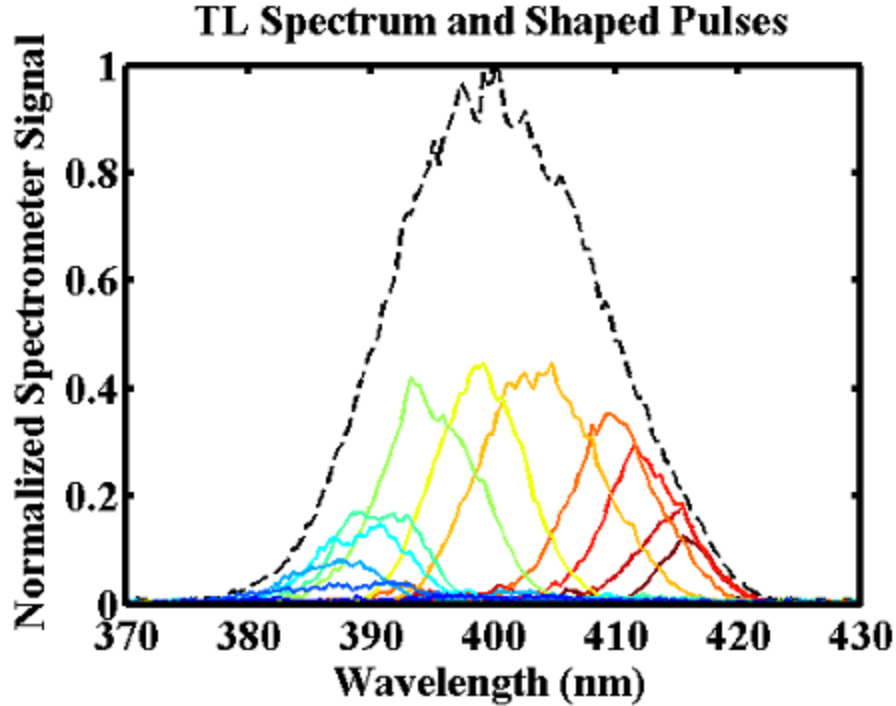


Figure 2.6: Tuning of phase masks. The central flat section of the phase mask can be shifted across the fundamental spectrum of the laser, leading to shaped pulses centered at different wavelengths in the SH spectrum.

To explore the differences between random binary phase shaping and amplitude shaping, a theoretical comparison is presented below. Simulations were performed as described in the literature [26] based on the equations described above. Here the effect of a symmetric random binary phase mask is compared to the effect of an equivalent amplitude shaped mask. First, a phase mask centered at 800 nm with a 20 nm central flat phase section is compared to an amplitude-shaped pulse with a 20 nm spectrum, as shown in figure 2.7. This shows the fundamental laser spectrum, this same spectrum limited to the 20 nm bandwidth, and the random binary phase mask. The right hand side of the phase mask appears to be stretched out due to the conversion between frequency space, where the mask is designed, and wavelength space. The simulated second harmonic spectra that result from these shapes are shown in the top panel of figure 2.8. The red line shows the TL result; this is a broad SH spectrum centered at half the wavelength of the fundamental laser spectrum. The

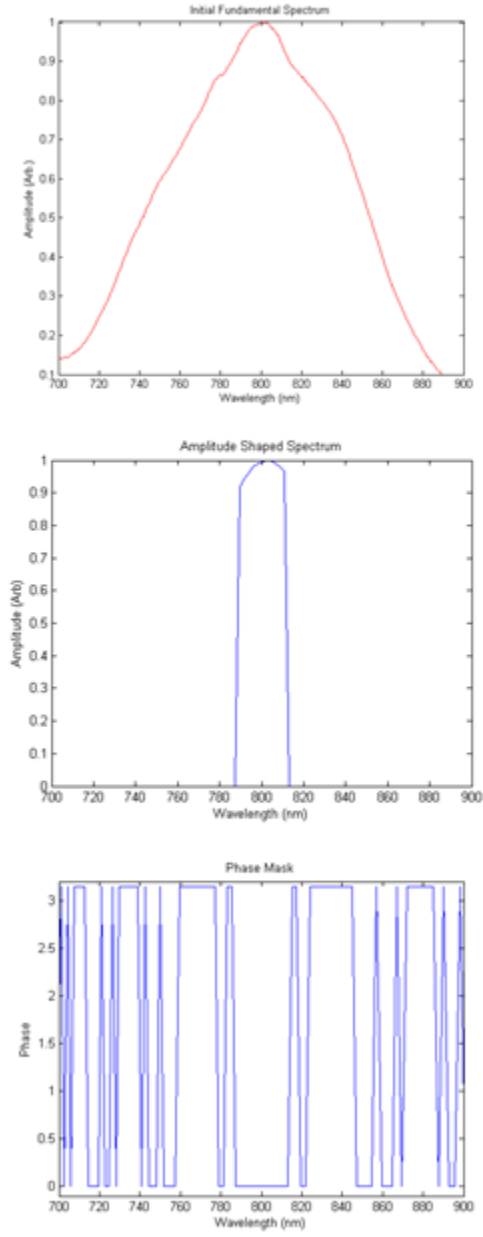


Figure 2.7: Fundamental laser spectrum, amplitude shaped spectrum, and phase mask used in simulation of random binary shaping.

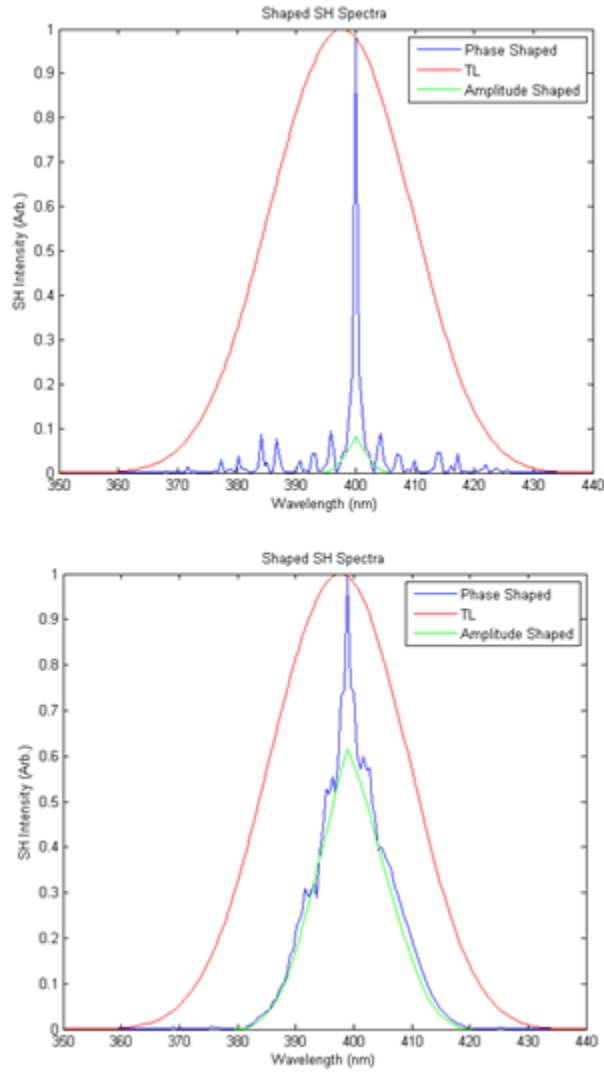


Figure 2.8: Comparison of different flat-phase widths. The top panel shows the calculated SH results for a phase mask with a 20 nm central flat section and amplitude shaping with the same bandwidth. The bottom panel shows the results for an 80 nm central flat section and the corresponding amplitude shaping. Both masks are centered at 800 nm. Increasing width results in increased SH peak width for both the amplitude- and phase-shaped pulses. However, the peak SH intensity of the amplitude-shaped pulse decreases dramatically with width while the phase-shaped pulse consistently approaches the TL envelope.

green line shows the amplitude shaped result, which is correctly centered at 400 nm. The blue line shows the phase shaped result which is also centered at 400 nm. From this plot, it is evident that the phase shaped pulse produces a higher SH intensity than the amplitude shaped pulse.

The effect of the size of the central flat section in the mask can also be investigated. The bottom panel of figure 2.8 shows the calculated SH spectra from a mask with an 80 nm flat section, still centered at 800 nm, along with the amplitude shaped and TL results. These figures show that the width of the SH peak increases with increasing flat phase width or amplitude-shaped width. This makes sense, as allowing more wavelengths through amplitude shaping increases the number of frequency components available to combine. For phase shaping, increasing the portion of the bandwidth with zero phase moves the pulse closer to the TL limit. The more notable behavior is in the peak intensity of the shaped pulses. The phase-shaped pulse consistently approaches the TL envelope regardless of the width of the central flat section, while decreasing bandwidth in the amplitude-shaped pulses decreases the peak intensity strongly. The stronger effect on the intensity of the amplitude-shaped pulse seen here is consistent with results presented in the literature [26]. This is one of the unique benefits of phase shaping over amplitude shaping, as phase shaping provides the narrow SH peaks of amplitude shaping but with much larger SH intensities, increasing the signal seen in experiments.

It is also possible to use these simulations to investigate the temporal behavior of the shaped pulses. The electric field intensities of the phase shaped, amplitude shaped, and TL pulses in time for a 40 nm mask centered at 800 nm are plotted in figure 2.9. From top to bottom, this shows the pulse durations of the TL, amplitude shaped, and phase shaped pulses as the full width at half max values of the curves. The TL pulse has a duration of approximately 12 fs, in good agreement with what is expected from the time-bandwidth product for a Gaussian pulse with the fundamental spectral

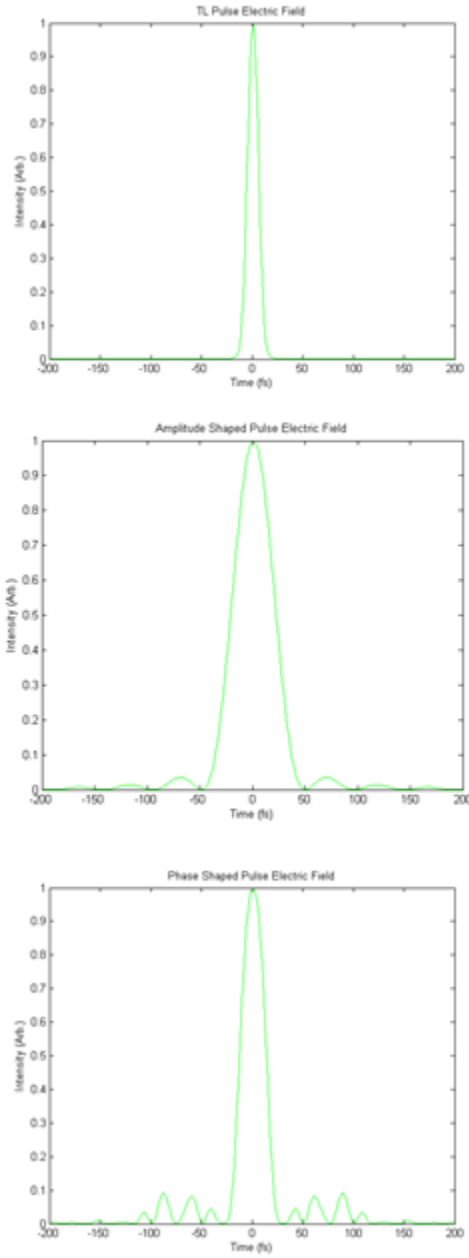


Figure 2.9: Temporal behavior of shaped pulses. From top to bottom, the electric field intensities of the TL, amplitude shaped, and phase shaped pulses. The pulse duration is shortest for the TL pulse and longest for the amplitude shaped pulse.

bandwidth used in this simulation. Under amplitude shaping, it is expected that the pulse duration will lengthen because bandwidth is being removed from the pulse. This is seen in the simulation, with the pulse duration increasing to approximately 40 fs. Phase shaping should not have as large of an effect on pulse durations - although the phase manipulation will lengthen the pulse in time, all bandwidth contained in the TL pulse is still present. The simulations show that the pulse duration lengthens to about 24 fs, roughly half of the amplitude-shaped duration. In the phase shaped plot, there are features outside of 200 fs, but these are small.

Because the phase mask design is random, the specific details of the SH intensities and pulse durations can change. However, the general pattern of the phase shaped pulse providing second harmonic intensities closer to the TL envelope than the amplitude shaped pulses is consistent. In addition, the electric field of the phase shaped pulse in time can show very complex behavior, consisting of several clustered smaller features. An example of this is shown in figure 2.10, which illustrates the case of a 40 nm wide phase mask centered at 820 nm. As shown in the top panel, the phase shaped pulse produces higher SH intensity than the amplitude shaped pulse, as expected. The bottom panel illustrates the more complex behavior of the electric field intensity of the phase shaped pulse. The individual features here are approximately 15 fs in duration, and thus shorter than the approximately 40 fs duration of the amplitude shaped pulse (not shown). This may have implications for photodamage in biological samples, as longer pulses have lower peak intensities and thus may cause less damage [38, 39]. The temporal behavior of phase shaped pulses has not been thoroughly investigated, but it is apparent that phase shaping does provide selective excitation with improved SH intensity (and thus two-photon excitation) compared to amplitude shaping. This, along with the flexibility in design of phase masks, makes phase shaping a promising tool for selective excitation in multiphoton microscopy.

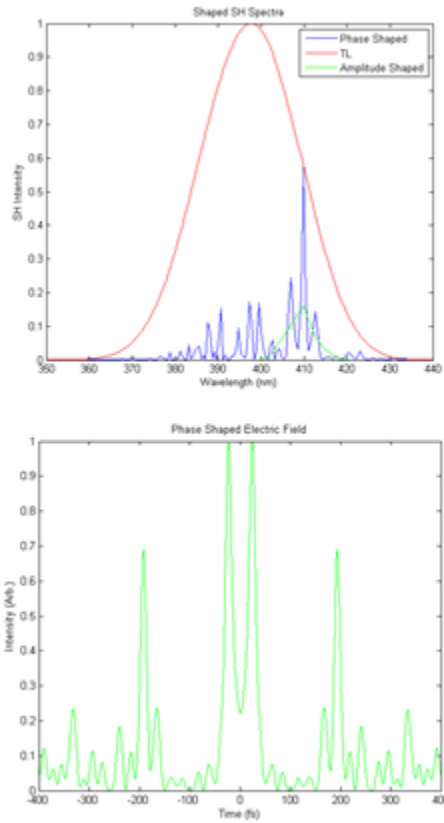


Figure 2.10: Simulated SH intensities and electric field for a phase shaped pulse centered at 820 nm with a 40 nm central flat section. The top panel shows the SH results; again, the phase shaped pulse shows higher SH intensity than the amplitude shaped pulse but with larger background here. The bottom panel shows the electric field intensity in time of the phase shaped pulse, illustrating its complex structure. Note that the individual features are still narrow.

2.4 Multiphoton Intrapulse Interference Phase Scan

Experiments involving ultrashort pulses often encounter problems with dispersion, which can dramatically lengthen the pulses in time by distorting the spectral phase. This is an important issue in multiphoton microscopy, as broadened pulses lead to lower fluorescence signal compared to TL pulses [21, 40] - and high numerical aperture microscope objectives cause significant dispersion. A number of techniques for dispersion compensation exist, such as chirped mirrors and grating- or prism-based pulse compressors, but these have the downsides of complex alignment and low laser power throughput. The Dantus group has developed a dispersion compensation method based on phase-shaping that helps mitigate these problems. Their technique, called Multiphoton Intrapulse Interference Phase Scan (MIIPS), takes advantage of the MI process described above to not only characterize the spectral phase distortion in the pulse but also correct for it [41–44]. The method has the advantage of relying only on the SLM, which reduces alignment complexity and improves power transmission.

As discussed in the previous section, maximum SH signal - or maximum two-photon excitation - occurs for TL pulses when the spectral phase is uniformly zero across the spectrum; dispersion makes the spectral phase non-zero. Spectral phase is typically a continuous function and can thus be expanded in a Taylor Series [42, 43]. For the sum of the phases at positive and negative detuning, this Taylor expansion is [42]

$$\Phi\left(\frac{\omega_0}{2} + \Omega\right) + \Phi\left(\frac{\omega_0}{2} - \Omega\right) = 2\Phi\left(\frac{\omega_0}{2}\right) + \Phi''\left(\frac{\omega_0}{2}\right)\Omega^2 + \dots + \frac{2}{(2n)!}\Phi^{2n'}\left(\frac{\omega_0}{2}\right)\Omega^{2n} \quad (2.9)$$

where $\Phi^{n'}(\omega) \equiv d^n\Phi(\omega)/d\omega^n$. The first term in this expansion, the absolute phase, is related to the position of the carrier wave in the pulse envelope [43]. Changes in this term do not affect the pulse shape; thus it is of little interest [41–43]. Consequently, when approximated to the first term in this expansion, the SH signal has a maximum

when the second derivative of the spectral phase is zero [41–44].

MIIPS works by implementing a known reference phase, $f(\omega)$, such that the total phase in the system $\Phi(\omega)$ is the sum of the reference phase and the unknown phase $\varphi(\omega)$ caused by dispersion:

$$\Phi(\omega) = f(\omega) + \varphi(\omega) \quad (2.10)$$

When the applied reference phase cancels the unknown phase, maximum SH signal is observed and the pulse approaches its minimum duration [41]. To first approximation in the Taylor expansion above, then, the maximum signal is seen when

$$\Phi''(\omega) = f''(\omega) + \varphi''(\omega) = 0 \quad (2.11)$$

Because the function $f(\omega)$ and its second derivative $f''(\omega)$ are known, the unknown phase $\varphi''(\omega)$ can be calculated [41–44].

With an SLM to apply reference phases, almost any phase function can be used [43]. However, the most common choice is a sinusoidal function. The first demonstration of MIIPS used the function $f(\omega) = \alpha \cos(\gamma\omega - \delta)$, where α determines the amplitude of the function and γ is an estimate of the compensated pulse duration [41]. δ is a parameter that is scanned; the SH spectrum is recorded across all frequencies for each value of δ . The result is a MIIPS trace which plots the SH intensity as a function of both frequency and δ . The value of δ at which the SH intensity is maximized is recorded and used to find the unknown phase. For the cosine phase function defined above,

$$\varphi''(\omega) = -f''(\omega) = \alpha\gamma^2 \cos[\gamma\omega - \delta_{max}(\omega)] \quad (2.12)$$

using the second derivative of the cosine function and equation (2.11) [41]. This equa-

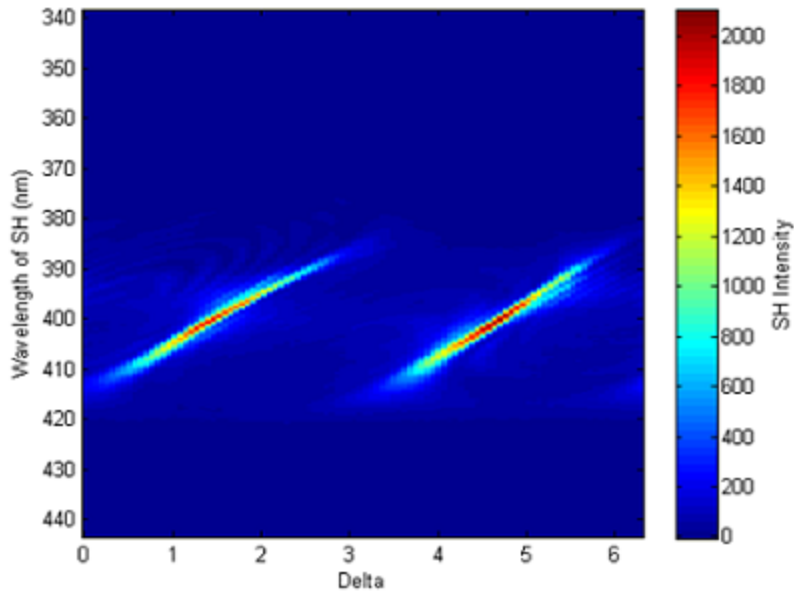


Figure 2.11: Sample MIIPS trace. This shows the SH intensity as a function of the parameter delta and the SH wavelength. The features of the plot reflect the phase characteristics of the pulse - spacing between the lines indicates the amount of second-order phase present, and the angle of the line indicates third-order phase.

tion is then integrated twice to find the spectral phase $\varphi(\omega)$, and then the opposite phase $-\varphi(\omega)$ is applied to the SLM to compensate the dispersion [41]. An example MIIPS trace is shown in figure 2.11; the placement of features in the trace contains information about the dispersion of the pulse [41–43]. For TL pulses, the lines will be separated by π along the delta axis; the presence of linear chirp changes this separation. When quadratic chirp is present, the slope of the lines is altered and they are no longer parallel.

This explanation ignored the higher order terms in the Taylor expansion in equation (2.9). These terms add some systematic error to the phase measurement, but this can be corrected by using an iterative MIIPS process [41, 42]. That is, one round of MIIPS is performed as described above and the resulting calculated phase is applied to the SLM. The reference function is then altered to have a smaller amplitude and the MIIPS process is repeated. The resulting phase from this round is added to the

result from the first round, and the process is repeated for any number of iterations. Results have shown that MIIPS converges to a near-TL result in as little as 3-5 iterations [41, 42]. The final correction phase is given by the sum of the results of all iterations.

MIIPS has the benefit of requiring a relatively simple setup. Aside from the SLM, implementation needs a beta barium borate (BBO) or similar crystal for second harmonic generation, collection optics, a spectrometer, and a computer to run the MIIPS algorithm. However, it is important to note that for MIIPS to accurately compensate for all dispersion in a setup, the second harmonic generation and detection must take place after all optics that could introduce phase distortions. In microscopy, this means that MIIPS should be measured at the sample position so the effect of the microscope objective is included. A demonstration of the effectiveness of MIIPS in the microscope is shown in figure 2.12. In this figure, the red line shows the initial SH intensity recorded through the microscope with no phase correction applied by the SLM. The blue line shows the final SH intensity after six iterations of MIIPS; there is a significant improvement.

One of the chief benefits of MIIPS compared to other pulse compression schemes is its flexibility. The amount of phase applied, the number of iterations used, and even the reference function can be changed. Although most work has been done with sinusoidal phase functions like that described here, other studies have used quadratic phase functions [44]. MIIPS is also straightforward to implement in the microscope, as demonstrated here and in studies from the Dantus group [21, 40]. Because MIIPS relies on an SLM in the same alignment as that used for phase shaping, it is an obvious choice for dispersion compensation in pulse shaping microscopy experiments, and is the method used in the studies described in this thesis.

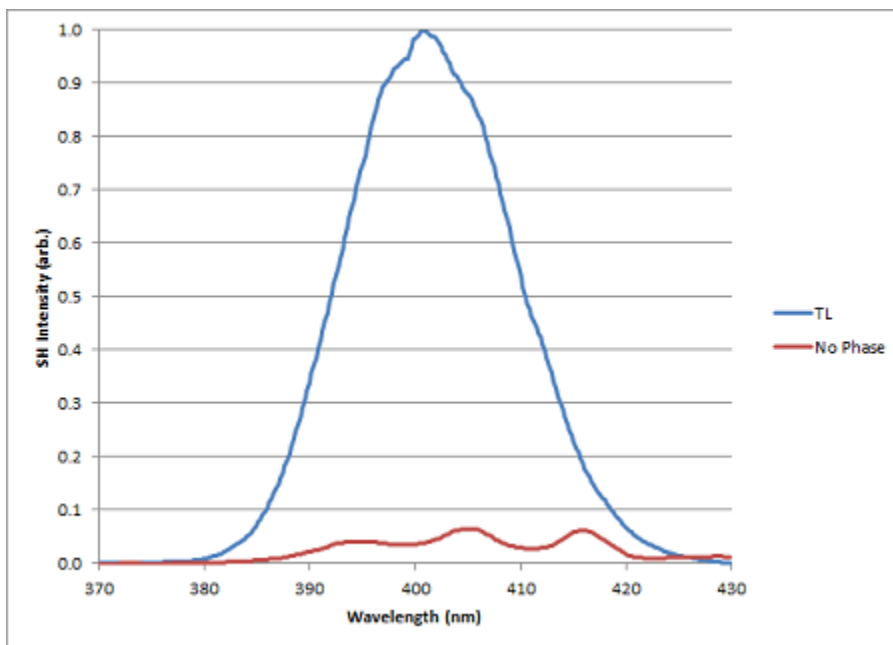


Figure 2.12: Improvement in SH intensity achieved with MIIPS. The blue plot shows the SH intensity seen after implementation of MIIPS. The red plot shows the initial SH intensity before any phase correction was applied to the pulse.

2.5 Conclusion

The phase shaping methods outlined in this chapter have proven to be a powerful tool for improving aspects of multiphoton microscopy. The ability to selectively excite individual fluorophores in multiply-labeled samples has led to identification of different solution pH environments [18] and regions of dyes embedded in PMMA [17]. Biological samples imaged with this type of selective excitation include HeLa cells [22] and *Drosophila* embryos [20]. In combination with the MIIPS technique, signal from biological samples was increased by a factor of 7 compared to non-compressed pulses [21] and the method worked even through scattering biological tissue [40]. The use of these pulse shaping techniques also has implications for photodamage rates in biological samples, as phase shaped pulses may cause reduced photodamage compared to TL pulses [39]. The next chapters of this thesis explore the application of these pulse shaping methods to two challenging problems in multiphoton microscopy,

namely multicolor imaging and quantitative FRET microscopy.

References

- [1] W. Denk, J. H. Strickler, and W. W. Webb. Two-photon laser scanning fluorescence microscopy. *Science*, 248(4951):73–76, 1990.
- [2] W. Denk. Two-photon excitation in functional biological imaging. *Journal of Biomedical Optics*, 1(3):296–304, 1996.
- [3] W. R. Zipfel, R. M. Williams, and W. W. Webb. Nonlinear magic: multiphoton microscopy in the biosciences. *Nature Biotechnology*, 21(11):1369–1377, 2003.
- [4] R. Y. Tsien. The green fluorescent protein. *Annual Review of Biochemistry*, 67(1):509–544, 1998. PMID: 9759496.
- [5] N. C. Shaner, P. A. Steinbach, and R. Y. Tsien. A guide to choosing fluorescent proteins. *Nature Methods*, 2(12):905–909, 2005.
- [6] D. Entenberg, J. Wyckoff, B. Gligorijevic, E. T. Roussos, V. V. Verkhusha, J. W. Pollard, and J. Condeelis. Setup and use of a two-laser multiphoton microscope for multichannel intravital fluorescence imaging. *Nature Protocols*, 6(10):1500–1520, October 2011.
- [7] M. Drobizhev, N. S. Makarov, S. E. Tillo, T. E. Hughes, and A. Rebane. Two-photon absorption properties of fluorescent proteins. *Nature Methods*, 8(5):393–399, May 2011.
- [8] A. M. Weiner. Femtosecond optical pulse shaping and processing. *Progress in Quantum Electronics*, 19(3):161–237, 1995.
- [9] A. M. Weiner. Femtosecond pulse shaping using spatial light modulators. *Review of Scientific Instruments*, 71(5):1929–1960, 2000.
- [10] A. M. Weiner. Ultrafast optical pulse shaping: A tutorial review. *Optics Communications*, 284(15):3669–3692, 2011.
- [11] D. Meshulach and Y. Silberberg. Coherent quantum control of two-photon transitions by a femtosecond laser pulse. *Nature*, 396(6708):239–242, 1998.
- [12] D. Meshulach and Y. Silberberg. Coherent quantum control of multiphoton transitions by shaped ultrashort optical pulses. *Physical Review A*, 60(2):1287–1292, 1999.

- [13] Y. Silberberg. Quantum coherent control for nonlinear spectroscopy and microscopy. *Annual Review of Physical Chemistry*, 60:277–292, 2009.
- [14] E. R. Tkaczyk, A. H. Tkaczyk, K. Mauring, J. Y. Ye, J. R. Baker Jr, and T. B. Norris. Control of two-photon fluorescence of common dyes and conjugated dyes. *Journal of Fluorescence*, 19(3):517–532, 2009.
- [15] E. R. Tkaczyk, A. H. Tkaczyk, K. Mauring, J. Y. Ye, J. R. Baker Jr, and T. B. Norris. Quantitative differentiation of dyes with overlapping one-photon spectra by femtosecond pulse-shaping. *Journal of Luminescence*, 130(1):29–34, 2010.
- [16] N. Dudovich, D. Oron, and Y. Silberberg. Single-pulse coherently controlled nonlinear raman spectroscopy and microscopy. *Nature*, 418(6897):512–514, 2002.
- [17] I. Pastirk, J. M. Dela Cruz, K. A. Walowicz, V. V. Lozovoy, and M. Dantus. Selective two-photon microscopy with shaped femtosecond pulses. *Optics Express*, 11(14):1695–1701, 2003.
- [18] J. M. Dela Cruz, I. Pastirk, V. V. Lozovoy, K. A. Walowicz, and M. Dantus. Multiphoton intrapulse interference 3: Probing microscopic chemical environments. *The Journal of Physical Chemistry A*, 108(1):53–58, 2004.
- [19] J. P. Ogilvie, D. Débarre, X. Solinas, J. Martin, E. Beaurepaire, and M. Joffre. Use of coherent control for selective two-photon fluorescence microscopy in live organisms. *Optics Express*, 14(2):759–766, 2006.
- [20] R. S. Pillai, C. Boudoux, G. Labroille, N. Olivier, I. Veilleux, E. Farge, M. Joffre, and E. Beaurepaire. Multiplexed two-photon microscopy of dynamic biological samples with shaped broadband pulses. *Optics Express*, 17(15):12741–12752, 2009.
- [21] L. T. Schelhas, J. C. Shane, and M. Dantus. Advantages of ultrashort phase-shaped pulses for selective two-photon activation and biomedical imaging. *Nanomedicine: Nanotechnology, Biology, and Medicine*, 2(3):177–181, 2006.
- [22] K. Isobe, A. Suda, M. Tanaka, F. Kannari, H. Kawano, H. Mizuno, A. Miyawaki, and K. Midorikawa. Multifarious control of two-photon excitation of multiple fluorophores achieved by phase modulation of ultra-broadband laser pulses. *Optics Express*, 17(16):13737–13746, 2009.
- [23] C. Froehly, B. Colombeau, and M. Vampouille. {II} shaping and analysis of picosecond light pulses. volume 20 of *Progress in Optics*, pages 63 – 153. Elsevier, 1983.
- [24] D. H. Reitze, A. M. Weiner, and D. E. Leaird. Shaping of wide bandwidth 20 femtosecond optical pulses. *Applied Physics Letters*, 61(11):1260–1262, 1992.

- [25] R. Nelson, D. Leaird, and A. Weiner. Programmable polarization-independent spectral phase compensation and pulse shaping. *Optics Express*, 11(15):1763–1769, 2003.
- [26] M. Comstock, V. Lozovoy, I. Pastirk, and M. Dantus. Multiphoton intrapulse interference 6; binary phase shaping. *Optics Express*, 12(6):1061–1066, 2004.
- [27] M. Göppert-Mayer. Über elementarakte mit zwei quantensprüngen. *Annalen der Physik*, 401(3):273–294, 1931.
- [28] R. W. Boyd. *Nonlinear Optics*. Nonlinear Optics Series. Elsevier Science, 2008.
- [29] N. Dudovich, B. Dayan, S. M. Gallagher Faeder, and Y. Silberberg. Transform-limited pulses are not optimal for resonant multiphoton transitions. *Physical Review Letters*, 86(1):47–50, 2001.
- [30] T. Brixner, N. H. Damrauer, B. Kiefer, and G. Gerber. Liquid-phase adaptive femtosecond quantum control: Removing intrinsic intensity dependencies. *The Journal of Chemical Physics*, 118(8):3692–3701, 2003.
- [31] K. A. Walowicz, I. Pastirk, V. V. Lozovoy, and M. Dantus. Multiphoton intrapulse interference. 1. control of multiphoton processes in condensed phases. *The Journal of Physical Chemistry A*, 106(41):9369–9373, 2002.
- [32] V. V. Lozovoy, I. Pastirk, K. A. Walowicz, and M. Dantus. Multiphoton intrapulse interference. ii. control of two-and three-photon laser induced fluorescence with shaped pulses. *The Journal of Chemical Physics*, 118(7):3187–3196, 2003.
- [33] E. R. Tkaczyk. *Femtosecond laser pulse optimization for multiphoton cytometry and control of fluorescence*. PhD thesis, The University of Michigan, 2008.
- [34] B. Broers, L.D. Noordam, and H.B. van Linden van den Heuvell. Diffraction and focusing of spectral energy in multiphoton processes. *Physical Review A*, 46(5):2749–2756, 1992.
- [35] V. V. Lozovoy and M. Dantus. Systematic control of nonlinear optical processes using optimally shaped femtosecond pulses. *ChemPhysChem*, 6(10):1970–2000, 2005.
- [36] Z. Zheng and A. M. Weiner. Spectral phase correlation of coded femtosecond pulses by second-harmonic generation in thick nonlinear crystals. *Optics Letters*, 25(13):984–986, 2000.
- [37] Z. Zheng and A. M. Weiner. Coherent control of second harmonic generation using spectrally phase coded femtosecond waveforms. *Chemical Physics*, 267(1):161–171, 2001.
- [38] H. J. Koester, D. Baur, R. Uhl, and S. W. Hell. Ca²⁺ fluorescence imaging with pico-and femtosecond two-photon excitation: signal and photodamage. *Biophysical Journal*, 77(4):2226–2236, 1999.

- [39] D. Pestov, Y. Andegeko, V. V. Lozovoy, and M. Dantus. Photobleaching and photoenhancement of endogenous fluorescence observed in two-photon microscopy with broadband laser sources. *Journal of Optics*, 12(8), 2010.
- [40] J. M. Dela Cruz, V. V. Lozovoy, and M. Dantus. Coherent control improves biomedical imaging with ultrashort shaped pulses. *Journal of Photochemistry and Photobiology A: Chemistry*, 180(3):307–313, 2006.
- [41] V. V. Lozovoy, I. Pastirk, and M. Dantus. Multiphoton intrapulse interference. iv. ultrashort laser pulse spectral phase characterization and compensation. *Optics Letters*, 29(7):775–777, 2004.
- [42] B. Xu, J. M. Gunn, J. M. Dela Cruz, V. V. Lozovoy, and M. Dantus. Quantitative investigation of the multiphoton intrapulse interference phase scan method for simultaneous phase measurement and compensation of femtosecond laser pulses. *JOSA B*, 23(4):750–759, 2006.
- [43] Y. Coello, V. V. Lozovoy, T. C. Gunaratne, B. Xu, I. Borukhovich, C. Tseng, T. Weinacht, and M. Dantus. Interference without an interferometer: a different approach to measuring, compressing, and shaping ultrashort laser pulses. *JOSA B*, 25(6):A140–A150, 2008.
- [44] V. V. Lozovoy, B. Xu, Y. Coello, and M. Dantus. Direct measurement of spectral phase for ultrashort laser pulses. *Optics Express*, 16(2):592–597, 2008.

CHAPTER III

Linear Unmixing

3.1 Introduction

The rise of fluorescent proteins has revolutionized the use of microscopy techniques in biological studies. They have the potential to provide several benefits over the use of artificial fluorophores, including improved labeling specificity and reduced toxicity in live-cell samples; fluorescent proteins may also cause fewer perturbations to the biological system being studied [1, 2]. There has been a great deal of research in developing new fluorescent proteins and improving the photophysical properties of existing ones, and as a result there is now a library of fluorescent proteins whose emission spectra span the visible wavelength range [3]. This has led to a number of innovative studies using multiple colors of fluorescent proteins, with applications including multi-color flow cytometry [4], simultaneously tracking multiple organelles [5] and/or single proteins [6], revealing super-resolution structures [7] or protein conformation changes [8, 9], accessing protein-protein colocalization [1] and interaction [10], and tracing neuronal networks [11] and cell colonial expansions [12, 13]. Fluorescent proteins provide convenient labeling for live animal imaging because they are expressed strongly in specific organs or cells [14, 15].

Although this rainbow of fluorescent proteins has been developed over recent years, the integration of multicolor imaging with two-photon microscopy methods has been

slow. Two-photon microscopy has several well-known benefits when compared to one-photon microscopy, including increased penetration depth into tissues, reduced photobleaching and phototoxicity, and inherent three-dimensional sectioning [16–18], as discussed in Chapter I. This method has been used successfully with two fluorescent proteins in a number of studies, such as simultaneous imaging of Green Fluorescent Protein (GFP) and Cyan Fluorescent Protein (CFP) in live cells by Sahai *et al.* in 2005 [19]. Kawano *et al.* [20] used Enhanced Green Fluorescent Protein (EGFP) and mKeima, a red fluorescent protein with a large Stokes shift, to perform two-color imaging with a single excitation wavelength. Tillo *et al.* [21] removed the requirement for one of the two fluorophores to have a large Stokes shift by taking advantage of the recently-discovered transitions to higher electronic states present in some red fluorescent proteins [22] to again allow simultaneous excitation of green and red fluorescent proteins by a single excitation wavelength.

Moving past two-color imaging to the use of three or more fluorescent proteins in two-photon fluorescence microscopy has proven challenging due to the need for multiple excitation wavelengths. A handful of techniques have been proposed, but they each have significant drawbacks. One method is the use of tunable femtosecond laser sources [23]; however, the tuning time, on the scale of seconds to minutes, limits the application of this method to experiments with low time resolution requirements. Another approach is to overlap multiple laser beams in the experimental setup. For example, Mahou *et al.* [24] used a titanium:sapphire (ti:sapph) oscillator coupled to an optical parametric oscillator (OPO) to generate two distinct excitation wavelengths, one from each laser, and a third effective excitation wavelength from the combination of the two independent beams. Other groups have proposed the use of two ti:sapph oscillators with a coupled OPO to generate three simultaneous, independent beams [23]. These setups, while powerful, come at a great cost due to the number of laser systems involved and can be challenging to align and maintain,

making their implementation in biological laboratories difficult.

The use of ultrabroadband laser sources with bandwidths on the order of 100 nm or greater is another approach to the problem of multicolor imaging. The transform-limited (TL) pulse from such a laser will generally overlap with the two-photon excitation spectra of numerous fluorescent proteins [22]. An example of this is shown in figure 3.1. This shows the simulated second harmonic (SH) spectra of TL pulses from two ultrabroadband lasers, a Venteon Pulse:One with approximately 300 nm bandwidth and a Femtolasers Synergy with approximately 100 nm bandwidth. Also plotted are several hypothetical shaped pulses designed to excite various fluorophores at the peaks of their two-photon absorption spectra. This figure shows that the TL spectra will simultaneously excite multiple fluorophores unless they are modified by pulse shaping. The fluorophores will also be excited at fixed efficiency ratios; this is undesirable as it means that relative fluorophore brightness cannot be adjusted, and autofluorescence or other unwanted signals may be amplified. Phase shaping of the Femtolasers Synergy spectrum is the method used in the experiments presented here, which enables selective excitation for multicolor imaging.

Aside from the technical challenges of generating enough excitation wavelengths to perform multicolor two-photon microscopy with several fluorescent proteins, challenges exist on the detection side of the setup as well. Efficient multicolor imaging requires the ability to distinguish the different colors present - otherwise, it is not possible to identify differently-labeled structures or recognize specific features of interest. One obvious solution to this problem is the use of multiple detection channels or filter sets to separate the different fluorescent colors - ideally a separate channel for each fluorophore present. However, as more and more colors are used to label the sample, this method becomes prohibitively expensive, and may run into space constraints in the physical setup. In addition, as more and more fluorophores are added to the biological system of interest, their emission spectra are more and more likely

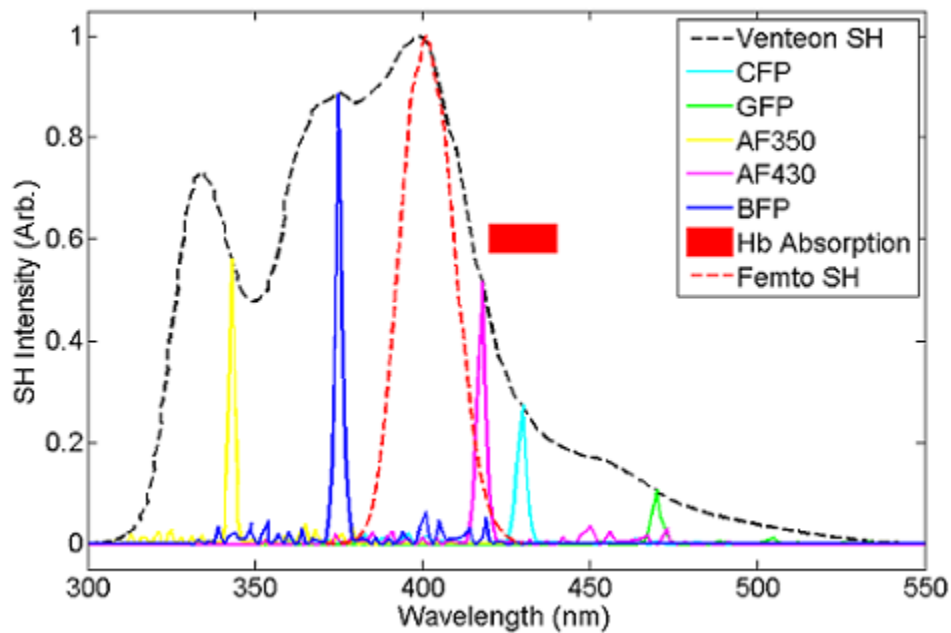


Figure 3.1: Simulated SH spectra of ultrabroadband lasers. This shows theoretical TL spectra of two ultrabroadband lasers, a Venteon with approx. 300 nm bandwidth and a Femtolasers Synergy with approx. 100 nm bandwidth. Also plotted are several possible pulse shapes to excite various fluorophores. Note that the TL spectra will not selectively excite individual fluorophores without modification via pulse shaping.

to overlap. Simply adding more detection channels does not resolve this, and filtering will not separate the signal from two fluorophores with overlapping emission spectra. In addition, filtering is not optimal for deep tissue imaging. Because fluorescence photons are easily lost to scattering in tissues, filtering the emission further degrades the signal and thus the resulting images.

An existing solution to this detection problem is linear spectral unmixing. This method was first used in geological remote sensing [25], but it has found extensive use in separating the fluorescence signal from multiple fluorescent proteins in biological samples [26]. In this method, a fluorescence emission spectrum is recorded from each pixel in the image. The output spectrum from any given pixel is considered to be a linear combination of the emission spectra of the fluorophores present in the sample, weighted according to the concentration of each fluorophore in that pixel. This method requires a separate detection channel for each fluorophore present, and the emission spectrum of each fluorophore must be found from reference samples containing just one of the fluorophores. The equation $S = \sum_i A_i \times R_i$ is solved for each measured spectrum S (i.e. from each detection channel) where R is the reference spectrum of a single fluorophore i and A is the weighting constant quantifying the amount of each component spectrum present. The weighting constants can be found for each pixel in the image and used to image how much of each fluorophore is present [26, 27]. This method has been used to separate fluorescence signals whose emission maxima are separated by just 7 nm [27], up to seven separate fluorescent colors [28], in live cells [29], and by measuring excitation spectra rather than detecting separate emission spectra [30]. While these methods are powerful, they suffer from the experimental complexity of setups designed to record whole emission spectra and the relatively long acquisition times needed to do so.

The work presented here uses a combination of ultrafast pulse shaping and linear unmixing to overcome the disadvantages described above [31]. Ultrafast pulse

shaping, already discussed in Chapter II of this thesis, is used to achieve selective excitation of multiple fluorescent proteins in live cell samples. This method has improved time resolution compared to the use of tunable lasers, a simpler set up and alignment compared to systems that use multiple lasers, and improved selectivity with flexibility in wavelength choice compared to techniques that rely on ultrabroadband sources. This work also utilizes a simplified version of linear unmixing that directly unmixes the pixel intensities of recorded images, resolving the problem of emission spectrum overlap. A key benefit achieved in the combination of ultrafast pulse shaping and linear unmixing is that the need to have a dedicated detection channel for each fluorophore present is eliminated - instead, distinct imaging conditions that are combinations of applied pulse shapes and existing detection channels can be used to create the necessary number of equations for the unknowns in the system. This chapter begins by detailing the theory of the linear unmixing method, then describes the experimental setup used and the results achieved. Selective excitation and separation of three fluorophores in live cells using just two pulse shapes and two detection channels is demonstrated, as published in [31].

3.2 Theory of Linear Unmixing

As described briefly above, linear spectral unmixing is an established method that solves a system of linear equations to determine the amount of each individual fluorophore present at each pixel in an image of a sample containing multiple fluorescent proteins [26, 27]. However, this method is based on acquisition of the actual fluorescence emission spectra, which can be difficult and time consuming. Instead, this work uses a simpler method that directly unmixes the image pixel intensities. Similar methods have been used in live cells to identify new proteins [32] and remove unwanted fluorescence signal [33].

This theory considers a sample containing three fluorescent proteins, although it

can be expanded for a larger number of fluorophores. Any given pixel in an image of this sample will contain some amount of signal from each of the three colors; the goal of this linear unmixing process is to determine the magnitudes of the contributions from each fluorophore. A recorded image taken under some combination of excitation and detection conditions (that is, a specific imaging condition) can be described as:

$$I = C_1F_1 + C_2F_2 + C_3F_3 = \sum_i C_i \times F_i \quad (3.1)$$

where I is the intensity of the image at any given pixel, F is the unknown intensity of one of the three fluorophores at that pixel, and C is a constant quantifying how much signal from fluorophore i is present under that specific imaging condition. Determining the three F values for each pixel will create three images - one for each fluorophore - that map out the intensities of the fluorophores across the image, and consequently map out their locations. The system as described right now cannot be solved, as there are three unknowns and just one equation. However, creating more imaging conditions to measure more I 's will increase the number of equations in the system. This linear unmixing process uses two detection channels and two excitation pulse shapes to create a total of four different imaging conditions, providing more than enough information to find the three unknown F values. The conditions are combinations of exciting with pulse shapes centered at wavelengths λ_1 and λ_2 and detecting long or short fluorescence wavelengths:

1. Excite with λ_1 and detect long wavelengths
2. Excite with λ_1 and detect short wavelengths
3. Excite with λ_2 and detect short wavelengths
4. Excite with λ_2 and detect long wavelengths

The result is four equations for four different image intensities:

$$I_{\lambda_1,L} = \sum_i Y_i \times F_i \quad (3.2)$$

$$I_{\lambda_1,S} = \sum_i X_i \times F_i \quad (3.3)$$

$$I_{\lambda_2,S} = \sum_i Z_i \times F_i \quad (3.4)$$

$$I_{\lambda_2,L} = \sum_i \Phi_i \times F_i \quad (3.5)$$

Here the notation is $I_{\lambda_n,M}$, where I is the image pixel intensity excited by the pulse shape centered at λ_n and detected in channel M. This system of equations can be written as a matrix equation:

$$\begin{pmatrix} I_{\lambda_1,L} \\ I_{\lambda_1,S} \\ I_{\lambda_2,S} \\ I_{\lambda_2,L} \end{pmatrix} = \begin{pmatrix} Y_A & Y_B & Y_C & Y_D \\ X_A & X_B & X_C & X_D \\ Z_A & Z_B & Z_C & Z_D \\ \Phi_A & \Phi_B & \Phi_C & \Phi_D \end{pmatrix} \times \begin{pmatrix} F^A \\ F^B \\ F^C \\ F^D \end{pmatrix} \quad (3.6)$$

In this form, it is clear that the weighting constants X, Y, Z, and Φ need to be determined in order to solve for the various F values, and that they will have different values for each fluorophore.

The first step in finding these weighting constants is to define the amount of crosstalk between detection channels (i.e. how much fluorescence accidentally leaks into the wrong detection channel) and the differences in excitation between the two pulse shapes (i.e. how well each shape excites the fluorophore). The two constants used are:

$$\alpha = \frac{I_{\lambda_1,S}}{I_{\lambda_2,S}} = \frac{I_{\lambda_1,L}}{I_{\lambda_2,L}} \quad (3.7)$$

and

$$\beta = \frac{I_{\lambda_1,S}}{I_{\lambda_1,L}} = \frac{I_{\lambda_2,S}}{I_{\lambda_2,L}} \quad (3.8)$$

Alpha compares image intensities under different excitation conditions, and beta compares image intensities between different detection channels. The equalities in the definitions of alpha and beta above hold because the filters used are consistent between imaging conditions. It is also important to note that each of the fluorophores to be unmixed has its own alpha and beta due to the fact that each fluorophore has its own excitation and emission characteristics. Experimentally, alpha and beta are determined from reference samples containing each fluorophore individually and imaged under all four conditions.

The system in this theory consists of fluorophores A, B, and C. The total fluorescence emitted by one of these fluorophores can be defined as the sum of the contributions from that fluorophore under all 4 imaging conditions:

$$F^A = I_{\lambda_1,S}^A + I_{\lambda_2,S}^A + I_{\lambda_1,L}^A + I_{\lambda_2,L}^A \quad (3.9)$$

where F^A is the total pixel intensity of fluorophore A and $I_{\lambda_n,M}^A$ is the pixel intensity of that fluorophore under those imaging conditions. The recorded images are the $I_{\lambda_n,M}^A$ but the desired result is F^A . It is not possible to simply add the four different images in practice, however, because in a generic sample containing all three fluorophores, each pixel may contain some mixture of signal from more than one fluorophore. However, this can be recast in terms of the previously defined crosstalk constants alpha and beta, which makes it possible to determine the weighting of the component fluorescent signals in each pixel. As an example, consider isolating the contribution from the $I_{\lambda_1,L}^A$

term:

$$F^A = I_{\lambda_1,S}^1 + I_{\lambda_2,S}^1 + I_{\lambda_1,L}^1 + I_{\lambda_2,L}^1 \quad (3.10)$$

$$= \beta I_{\lambda_1,L}^A + I_{\lambda_1,L}^A + \frac{\beta}{\alpha} I_{\lambda_1,L}^A + \frac{1}{\alpha} I_{\lambda_1,L}^A \quad (3.11)$$

$$= \frac{1}{\alpha} (\alpha\beta I_{\lambda_1,L}^A + \alpha I_{\lambda_1,L}^A + \beta I_{\lambda_1,L}^A + I_{\lambda_1,L}^A) \quad (3.12)$$

$$= \frac{I_{\lambda_1,L}^A}{\alpha} (\alpha\beta + \alpha + \beta + 1) \quad (3.13)$$

$$I_{\lambda_1,L}^A = \frac{\alpha}{(\alpha\beta + \alpha + \beta + 1)} F^A \quad (3.14)$$

Similar derivations can isolate each of the other three components. The final set of four equations relating the images to the constants are:

$$F^A = \frac{I_{\lambda_1,L}^A}{\alpha} (\alpha\beta + \alpha + \beta + 1) \quad (3.15)$$

$$F^A = I_{\lambda_2,L}^A (\alpha\beta + \alpha + \beta + 1) \quad (3.16)$$

$$F^A = \frac{I_{\lambda_1,S}^A}{\alpha\beta} (\alpha\beta + \alpha + \beta + 1) \quad (3.17)$$

$$F^A = \frac{I_{\lambda_2,S}^A}{\beta} (\alpha\beta + \alpha + \beta + 1) \quad (3.18)$$

However, $I_{\lambda_n,M}^A$ cannot be measured directly - a mixture of the three fluorophores is always imaged:

$$I_{\lambda_1,L} = F_{\lambda_1,L}^A + F_{\lambda_1,L}^B + F_{\lambda_1,L}^C \quad (3.19)$$

where $I_{\lambda_1,L}$ is an actual recorded image in an experiment. Note that this is the same as equation (3.1). Including all constants, then, the actual recorded images can be written as linear combinations of the signal from the three fluorophores weighted

according to the magnitudes of the crosstalk constants:

$$I_{\lambda_1,L} = \frac{\alpha_A}{(1 + \alpha_A + \beta_A + \alpha_A\beta_A)} F^A + \frac{\alpha_B}{(1 + \alpha_B + \beta_B + \alpha_B\beta_B)} F^B + \frac{\alpha_C}{(1 + \alpha_C + \beta_C + \alpha_C\beta_C)} F^C \quad (3.20)$$

$$I_{\lambda_1,S} = \frac{\alpha_A\beta_A}{(1 + \alpha_A + \beta_A + \alpha_A\beta_A)} F^A + \frac{\alpha_B\beta_B}{(1 + \alpha_B + \beta_B + \alpha_B\beta_B)} F^B + \frac{\alpha_C\beta_C}{(1 + \alpha_C + \beta_C + \alpha_C\beta_C)} F^C \quad (3.21)$$

$$I_{\lambda_2,L} = \frac{1}{(1 + \alpha_A + \beta_A + \alpha_A\beta_A)} F^A + \frac{1}{(1 + \alpha_B + \beta_B + \alpha_B\beta_B)} F^B + \frac{1}{(1 + \alpha_C + \beta_C + \alpha_C\beta_C)} F^C \quad (3.22)$$

$$I_{\lambda_2,S} = \frac{\beta_A}{(1 + \alpha_A + \beta_A + \alpha_A\beta_A)} F^A + \frac{\beta_B}{(1 + \alpha_B + \beta_B + \alpha_B\beta_B)} F^B + \frac{\beta_C}{(1 + \alpha_C + \beta_C + \alpha_C\beta_C)} F^C \quad (3.23)$$

Thus, the system is described by four equations with the three unknowns F_A , F_B , and F_C . Comparing this to equation (3.6) shows that the X, Y, Z, and Φ constants can be found explicitly from the alpha and beta constants. Once the constants are known and the images from the four different conditions are taken, the matrix equation is solved for the unknown fluorescence intensities and the signals are fully unmixed.

3.3 Experimental Methods

The experimental setup is shown in figure 3.2 [31]. A Femtolasers Synergy ti:sapph oscillator (75 MHz repetition rate, 80 nm pulse bandwidth centered at 790 nm) was aligned into a Biophotonic Solutions Inc. femtoJock pulse shaper. This shaper utilized a single-mask 128-pixel spatial light modulator (SLM) in a reflective 4f alignment to phase-shape the input pulses. The beam was then sent through a variable neutral density filter to control the laser power at the sample and aligned into the microscope. The microscope used was an Olympus BX51WI upright microscope modified with a

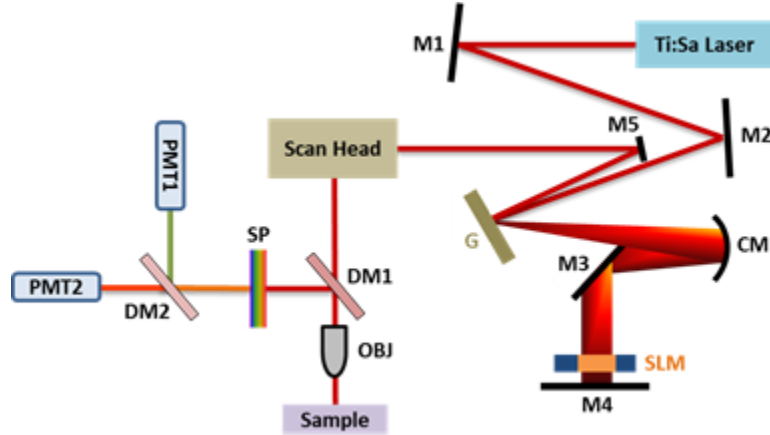


Figure 3.2: Experimental setup for linear unmixing. M1-M5: mirrors, G = grating, CM = curved mirror, SLM = spatial light modulator, DM1 = 660DCXR dichroic mirror, DM2 = 595DCXR dichroic mirror, OBJ = 60x NA1.2 water immersion objective; SP = 650 nm short pass filter [31].

Prairie Technologies scanning mirror assembly. The input beam was focused with an Olympus UPlanApo 60x, 1.2NA water-immersion objective and fluorescence signal was recollected with the same objective. The fluorescence was then separated from the input laser light with a 660DCXR dichroic mirror; an additional short-pass filter with a cutoff at 650 nm further blocked input laser light. The fluorescence signal was split into two channels with a 595DCXR dichroic for simultaneous multicolor detection with two photomultiplier tubes (PMTs).

A major concern in the setup is the introduction of dispersion by the microscope optics, which can decrease two-photon fluorescence signal [34]. To correct for this effect, the femtoJock pulse shaper was used to perform Multiphoton Intrapulse Interference Phase Scan (MIIPS) [35–37]. MIIPS measures the output signal from second harmonic generation (SHG) as the SLM applies various amounts of phase; when the maximum SHG signal is detected, the setup dispersion has been corrected and TL pulses are achieved. The theory of this technique was described in more detail in Chapter II of this thesis. For MIIPS to work efficiently in a microscope, the SHG detection must take place after all optics that need to be corrected, including the

objective. To accomplish this, a 1 mm thick beta barium borate (BBO) crystal was mounted on a #1 glass coverslip and placed at the focus of the microscope. The coverslip was used to protect the BBO crystal from the water needed for the water immersion microscope objective. After the crystal, the fundamental was filtered out using a short pass filter with a 670 nm cutoff and the SHG light was sent into a fiber-coupled Ocean Optics compact spectrometer. The femtoJock box and its software then performed the MIIPS routine and the final pulse shape was applied to the SLM to create a TL baseline before application of additional shapes. MIIPS was run in conjunction with the use of chirped mirrors for further dispersion compensation; a total of 8 pairs of bounces with -200 fs^2 per bounce was used.

To perform multicolor two-photon imaging, fluorescent proteins must be chosen carefully such that their two-photon excitation spectra overlap with the laser bandwidth. The three fluorophores used in this experiment were mAmetrine, TagRFpT, and mKate2. mAmetrine is a yellow-fluorescing protein with a large Stokes shift [9]. mKate2 fluoresces in the far-red with improved brightness compared to several other far-red proteins [38]. TagRFpT is a variant of the red fluorescent protein TagRFP with improved photostability [39, 40]. Both mKate2 and TagRFpT exhibit large peaks in their two-photon absorption spectra at shorter wavelengths than would be expected by simply doubling their optimal one-photon excitation wavelength; this is thought to be due to transitions to higher excited states than S_1 [22, 41]. By taking advantage of this fact and mAmetrine's large Stokes shift, all three of these fluorophores can be easily excited by the laser bandwidth used here. The relevant spectra are plotted in figure 3.3 [31]. This figure shows the two-photon brightness curves, defined as the two-photon absorption spectrum of each fluorophore multiplied by its quantum yield, in the dashed green, orange, and red lines for mAmetrine, TagRFP, and mKate2 respectively; spectra are adapted from [22]. TagRFpT is known to be spectrally similar to TagRFP [40, 42]. Also plotted are the fluorophores' emission spectra (solid green,

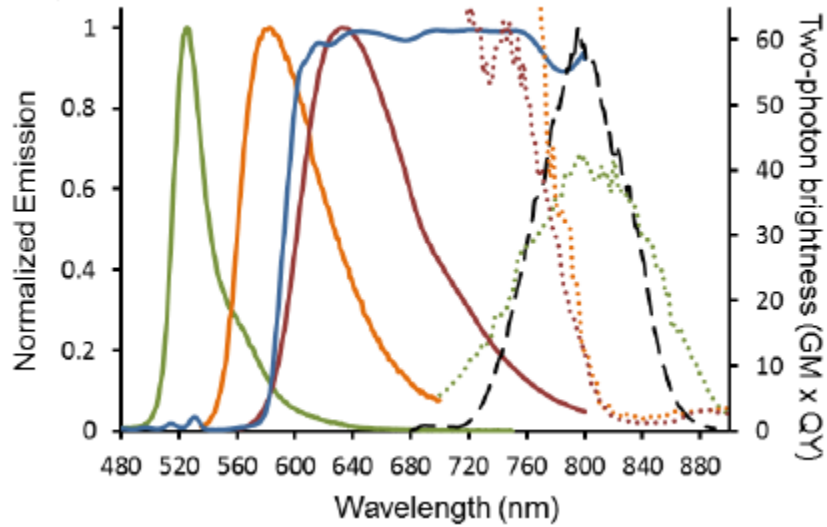


Figure 3.3: Spectra of fluorescent proteins used for linear unmixing. Two-photon brightness (dashed lines) and fluorescent emission spectra of mAmetrine (green), TagRFP (orange), and mKate2 (red). TagRFP is spectrally similar to TagRFPt [40, 42]. Also shown are the fundamental laser spectrum (black dashed line) and dichroic cutoff (blue solid line) [31]. Spectra are adapted from [22].

orange, and red lines), the normalized fundamental laser spectrum (dashed black line), and the cutoff position of the 595 dichroic used to separate the fluorescence (solid blue line). It can be seen that all three fluorophores' brightness curves overlap with the laser, with the potential to selectively excite mAmetrine with longer wavelengths and TagRFPt and mKate2 with shorter wavelengths. Furthermore, the emission spectra are sufficiently distinct to be separated by the dichroic into two channels and further separated by linear unmixing.

Two binary phase masks were created and applied to the SLM to perform the required selective excitation, designed similarly to those described in Comstock *et al.* [43]. The masks themselves are shown in figures 3.4 and 3.5. They were 128 elements long, consisting of a zero-phase section 40 nm wide centered around twice the desired two-photon excitation wavelength maximum. The masks had a semi-random choice of zero or pi elsewhere, based on a prime number sequence such that a flip between

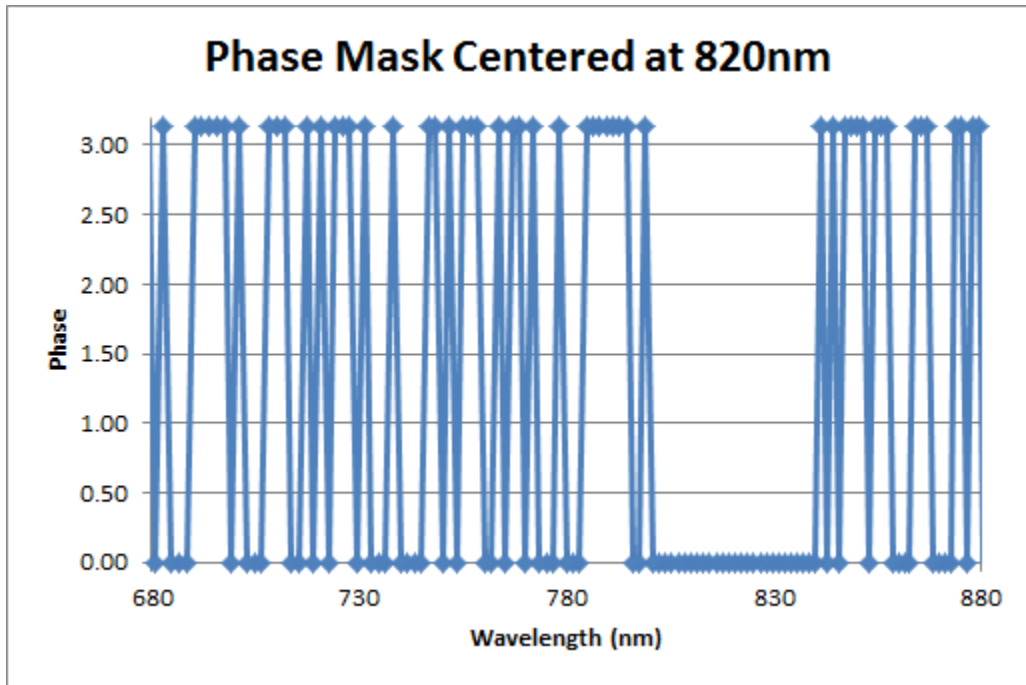


Figure 3.4: Linear unmixing binary phase mask centered at 820 nm.

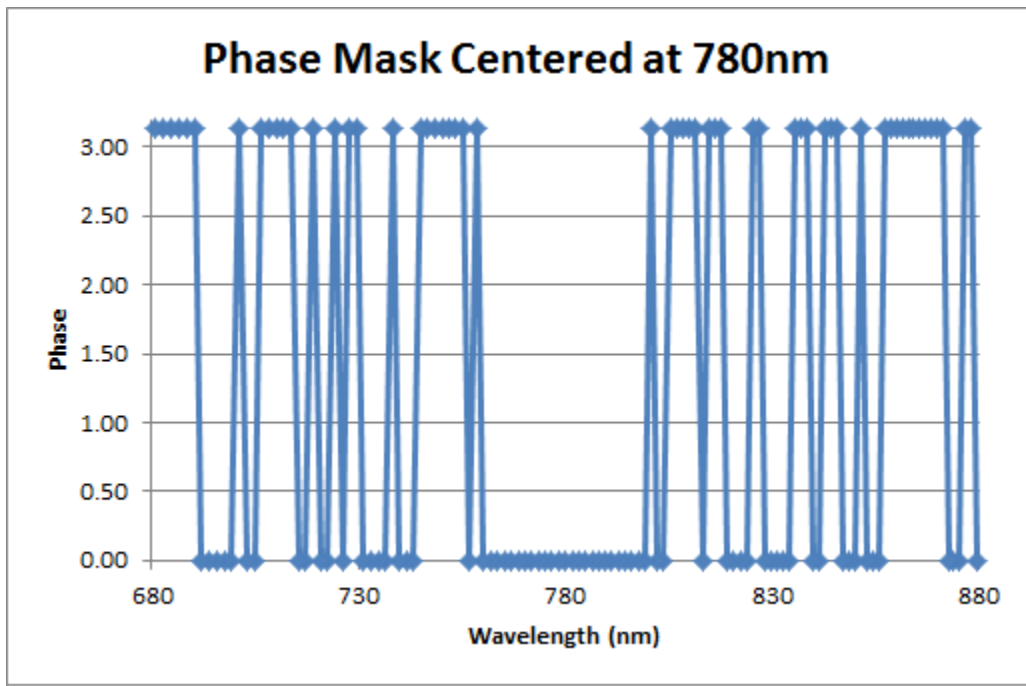


Figure 3.5: Linear unmixing binary phase mask centered at 780 nm.

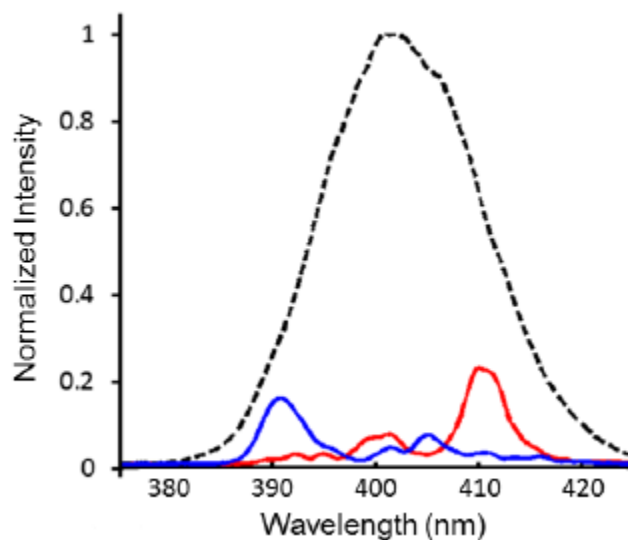


Figure 3.6: Second harmonic spectra of shaped pulses. The red and blue lines show the SH spectra of the red and blue shaped pulses, respectively; the black dashed line shows the SH spectrum of the TL pulse [31].

zero and π occurred at every prime number. This sequence could then be multiplied by a spacing factor to adjust the number of pixels in each flip; these masks used a spacing factor of 2 chosen to improve the ratio of signal in the main desired peak to signal in undesired side peaks. The prime number sequence could also start at different integers, providing another parameter that was similarly optimized. The binary portion of the mask was roughly symmetric about the central flat section. The two masks were centered at 780 nm (the blue shaped pulse) and 820 nm (the red shaped pulse), generating second harmonic peaks at 390 nm and 410 nm respectively. As a test, these masks were applied to the SLM and the resulting second harmonic spectra were recorded; these are shown in figure 3.6 [31]. The blue and red lines show the blue and red shaped pulses, respectively; the black dashed line shows the SH spectrum of the TL pulse. This figure clearly shows that the SH spectrum is shaped as expected and centered at the desired wavelengths.

These shapes, in addition to the TL pulse, were used to image multiple cells in

multiple sample types. Samples consisted of COS-7 cells grown in 100 mm tissue culture dishes with 10 mL Dulbecco's Modified Eagle's Medium (DMEM) supplemented with 10% fetal bovine serum and 1% each Penicillin-Streptomycin and GlutaMAX glutamine. Once confluent, the media was removed and the dish was rinsed with 5 mL Phosphate-Buffered Saline (PBS) at pH 7.4. After rinsing, 1 mL of 0.25% Trypsin-EDTA was added and the dish was placed in the incubator for a few minutes to loosen the cells. Once the cells detached, the Trypsin-EDTA was nullified by the addition of 9 mL of media. The concentration of the cell solution was then counted with a hemacytometer, and approximately 60,000 cells were added to each of three 35 mm tissue culture dishes. The dishes were filled to approximately 2 mL total volume with media. These were placed in the incubator for 24 hours to allow the cells to reattach to the dish. To prepare transfections, 100 μ L of Opti-Mem reduced serum media was placed in each of three small eppendorf tubes. For each of the three fluorophores used, approximately 0.5 μ g of purified plasmid DNA was added to one of the eppendorfs. Finally, 3 μ L of FuGene 6 transfection reagent was added directly to the liquid in each tube, the tubes were shaken to mix, and allowed to incubate at room temperature for 15 minutes. After incubation, the solutions were re-mixed gently by pipetting and were added drop-wise onto the three tissue culture dishes from the previous day such that each dish contained DNA for a single fluorophore. The dishes were placed in the incubator for an additional 24 hours to allow for protein expression.

To create a single tissue culture dish containing a mixture of cells, each expressing a single fluorophore, the transfected cells were further passaged. Each of the three single-color transfected dishes was rinsed with 1 mL PBS, then 200 μ L Trypsin-EDTA was used to remove them from the dish. Once loose, 2 mL media was added to each plate to stop the reaction, then 800 μ L of each of the single-color cell solutions was added to a 50 mm tissue culture dish. Finally, an additional 3 mL of media was added

to the dish and it was placed in the incubator for an additional 24 hours. Just before imaging, the media was removed from the dish and replaced with 5 mL of Ringer's Buffer. Additional samples were made that contained mixed transfections of the three fluorophores. The same protocol described above was followed, but approximately one-third of the amount of each plasmid DNA used for the single-color transfections was added to a single eppendorf tube. This was added to a 35 mm tissue culture dish which was then allowed to incubate for an additional 48 hours prior to imaging.

During imaging, the tissue culture dish was placed on the microscope stage and the objective was immersed directly into the buffer. Areas of interest to image were found using an Exfo fluorescence lamp for excitation and the microscope eyepiece; a pulse shape was then applied and the microscope was switched to laser excitation and PMT detection. The incident power at the sample was approximately 3.5 mW. Prairie Technologies' PrairieView software was used for visualization and image acquisition. Once the cells were in focus, an image was taken with the first pulse shape. The beam was blocked while the second pulse shape was applied to minimize exposure to the laser, then the second shaped pulse image was taken. Finally, the beam was blocked again to apply the TL pulse, and a final image was taken. The order in which the shaped pulses was applied was alternated to ensure that the results seen were not a result of potential photobleaching or photodamage effects. The microscope objective was cleaned with lens tissue and a mixture of acetone and ethanol between samples. All images were 512x512 pixels, covering approximately 220x220 μm , taken as averages of 16 frames with a dwell time of 4 μs per pixel.

After acquisition, images were loaded into Matlab for analysis. First, the images were filtered to smooth noise using a 5 pixel by 5 pixel Gaussian filter with a sigma of 1 pixel. Next, the filtered images were background subtracted. The sum of the images from the two channels with the TL pulse applied was used to identify background regions without cells in the field of view and create a mask selecting two such regions.

Both channels of the TL pulse were used for this to ensure that all cells were visible in the image and the areas chosen as background did not contain fluorescence. This mask was then applied to the images taken with the shaped pulses; the pixels in the mask were averaged and this value was subtracted from each pixel in the image. A different mask was chosen for each field of view imaged, and the background value subtracted from each image was determined by the backgrounds in that image itself.

Cells expressing single colors were then used to calculate the alpha and beta parameters for each fluorophore as described in the theory section above. Fields of view were first masked to ensure that only cells expressing a particular fluorophore and with non-saturating intensities were included in calculations. To do this, the two images (one from each PMT) taken with the blue shaped pulse were used to create two independent masks including non-saturating cells. This shape was used because it excited all three fluorophores, but the fluorophores could be distinguished by the fact that mAmetrine appeared in the short-wavelength detection channel only, mKate2 appeared in the long-wavelength detection channel only, and TagRFpT appeared in both detection channels. The separate masks were then summed to create a final mask with parameters set such that only one of the three fluorophores was measured at a time. The alpha and beta calculations were performed on each pixel in the image, and then pixels that passed the final mask were averaged to a final value. This was repeated for each region of interest imaged, and the final alpha and beta values were the averages of these results. The final values are discussed in detail in the results section below. Finally, these values were used in a separate Matlab code to solve the final linear equation and perform the unmixing. Because three fluorophores are present, three equations are needed to find a solution. With the two excitation pulse shapes used here and two detection channels, four imaging conditions are available. The images acquired using the red-shaped pulse and recorded in the red detection channel were ignored for unmixing purposes. This is because the red-

shaped pulse primarily excites mAmetrine, but its fluorescence primarily appears in the green detection channel. Thus this image is the dimmest of the four available and was not used for unmixing.

3.4 Results

First, the ability to perform selective excitation was tested. A sample of cells was created where each cell expressed a single fluorophore, but cells of all three colors were present. This was used to confirm that the shaped pulses would selectively excite fluorophores compared to the use of a TL pulse; figure 3.7 shows a series of images demonstrating this [31]. Panels (a), (c), and (e) show images taken in the Green fluorescence detection channel; panels (b), (d), and (f) show images taken in the Red fluorescence detection channel. The first column, panels (a) and (b), show images taken with the TL pulse applied. It is shown that all three fluorophores are excited, as expected; the fluorescence signal is also separated between the Green and Red channels as expected. The mKate2 cells, indicated by the solid arrowheads, appear predominantly in the Red detection channel. The mAmetrine cells, indicated by the solid arrows, appear predominantly in the Green detection channel. The TagRFPT cells, indicated by the open arrows, appear in both channels, reflecting the fact that the dichroic splits the TagRFPT fluorescence. Use of the TL pulse leads to higher fluorescence intensities than the shaped pulses, due to the fact that there are many more potential combinations of photons leading to excitation. As a result, lower PMT voltages were used to acquire the TL images than were used for the shaped pulse images, decreasing the overall intensity by a factor of approximately 7. The TL image intensities shown here were multiplied by this scaling factor to make them comparable to the shaped pulse images; however, they were then decreased by a factor of 10 to prevent saturation.

The middle column, panels (c) and (d), are images taken using the blue phase

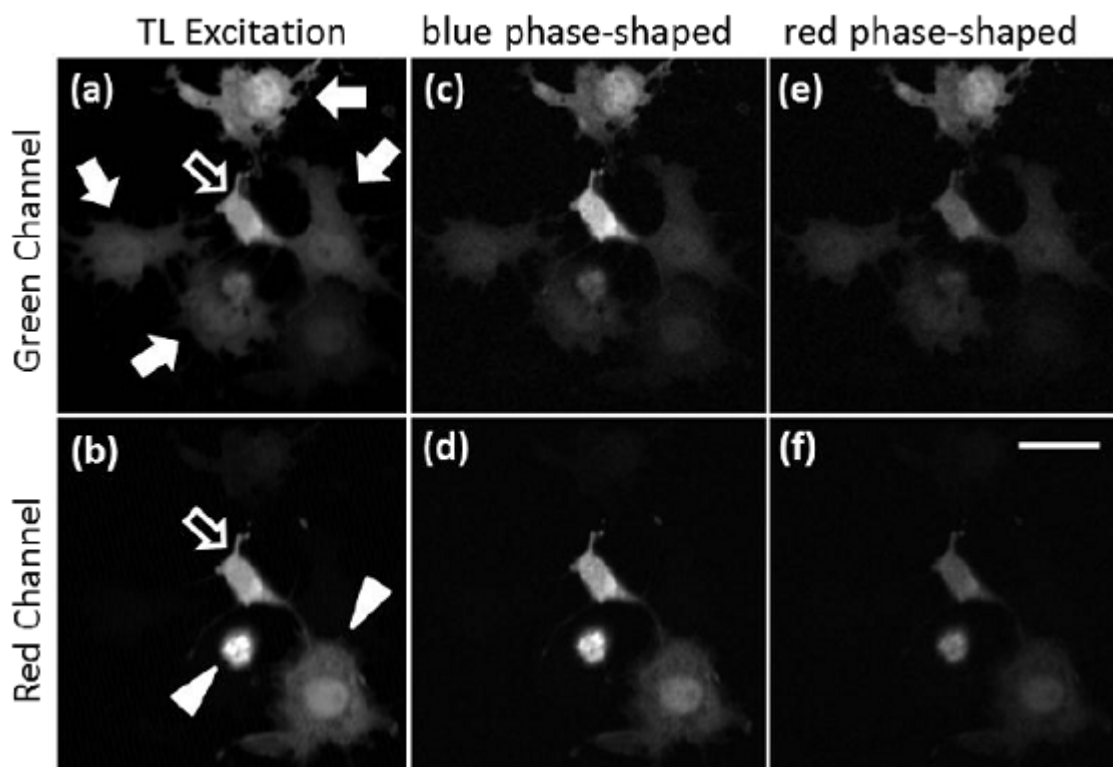


Figure 3.7: Demonstration of selective excitation using shaped pulses. This is a mixed sample where all 3 fluorophores are present, but each cell expresses only one. Cells were excited by the TL (left column), blue phase shaped (middle column) and red phase shaped (right column) pulses. The top and bottom rows indicate images acquired in the Green and Red detection channels, respectively. The solid arrows indicate mAmetrine cells, the open arrows indicate TagRFPT cells, and the solid arrowheads indicate mKate2 cells. The TL pulses lead to higher image intensities than the shaped pulses; as a result, to avoid saturation, lower PMT voltages were used to decrease the fluorescence intensity by a factor of 7. Additionally, the brightness and contrast of panels (a) and (b) were scaled down by 10 fold to avoid saturation in display. Scale bar is 20 μm [31].

shaped pulse (centered at 780 nm in the fundamental spectrum and 390 nm in the second harmonic spectrum). The right column, panels (e) and (f), are images taken using the red phase shaped pulse (centered at 820 nm in the fundamental spectrum and 410 nm in the second harmonic spectrum). Comparison of the images across these two columns shows that the shaped pulses do provide selective excitation. Comparing panels (d) and (f) shows the effect of this on the TagRFPt and mKate2 cells. Their fluorescence signal is noticeably brighter when excited with the blue phase shaped pulse than when excited by the red phase shaped pulse. This corresponds to the fact that the fluorophores' two-photon brightness spectra are much larger at 390 nm than 410 nm, as shown in figure 3.3. In contrast, panels (c) and (e) show the effect of the different shaped pulses on mAmetrine. As indicated in figure 3.3, the two-photon brightness of mAmetrine is roughly equal at 390 nm and 410 nm. Consequently, the images taken with the two different pulse shapes do not show dramatic differences in signal intensities. The results presented in figure 3.7 demonstrate that the two pulse shapes used in this experiment do provide selective excitation of the fluorophores, particularly when compared to excitation from the unshaped TL pulse.

Using populations of the cells expressing single colors, the alpha and beta constants for each fluorophore were determined. Alpha is defined as $\alpha = \frac{I_{Blue,G}}{I_{Red,G}} = \frac{I_{Blue,R}}{I_{Red,R}}$ and $\beta = \frac{I_{Blue,G}}{I_{Blue,R}} = \frac{I_{Red,G}}{I_{Red,R}}$ where Blue or Red denote the blue or red shaped pulses, respectively, and G and R denote the green and red detection channels. Approximately 10 cells expressing each fluorophore were imaged, the calculations were performed, and then the results were averaged to give a final value; this average value was used in the subsequent unmixing. All results are presented here as the average value plus/minus the standard deviation. For mAmetrine, the calculated alpha value was $\alpha = 1.09 \pm 0.06$ found by comparing images excited by the two shaped pulses and recorded in the green detection channel. The mAmetrine beta value was $\beta = 17.05 \pm 0.74$, found by comparing images excited by the blue-shaped pulse and

recorded in the two different channels. These two values are consistent with expectations given the fluorophore spectra and filters used - the alpha value close to one reflects the fact that mAmetrine is excited similarly by both shaped pulses, and the large beta value reflects the fact that much more mAmetrine signal is present in the green detection channel than in the red. For mKate2, the values found were $\alpha = 2.08 \pm 0.06$ and $\beta = 0.32 \pm 0.03$. The alpha was found by comparing images taken in the red detection channel, and the beta value was found by comparing images taken with the blue-shaped pulse. Again, these results display the expected behavior - the alpha value of approximately 2 indicates that mKate2 is excited roughly twice as efficiently by the blue-shaped pulse than by the red-shaped pulse, and the beta value less than one is indicative of the fact that more mKate2 signal appears in the red detection arm than the green detection arm. Finally, for TagRFpT, the constant values were $\alpha = 2.4 \pm 0.17$ and $\beta = 1.11 \pm 0.02$. The alpha value was found by comparing images recorded in the green detection channel, and its value reflects the expected behavior that TagRFpT is preferentially excited by the blue-shaped pulse. The beta value was found by comparing images in the two detection channels taken with the blue-shaped pulse and its value near one reflects the fact that its fluorescence signal is split between the two channels.

It should be noted that the definitions of alpha and beta given in the theory section above can be applied to comparisons across either detection channel or shaped pulse - that is, alpha can be defined as the ratio of images taken with the two shaped pulses and recorded in either the green or red detection channel, and beta can be defined as the ratio of images recorded in the two detection channels and taken with either shaped pulse applied. When compared, the alphas and betas calculated with the two different comparisons were similar for all three fluorophores. The choice of which value to use was determined by which produced the smallest standard deviation in the final averaged result. This was physically related to which detection

channel or shaped pulse provided higher signal. For example, the mKate2 alpha value was based on comparisons in the red detection channel because much more signal is present there, giving reduced noise and a cleaner calculation result. Similarly, mKate2 is preferentially excited by the blue-shaped pulse, so its beta was calculated from comparisons using that shaped pulse for excitation.

Additionally, the images of the mixed sample (containing a mixture of cells expressing a single fluorophore) were taken on a different day from the images of the co-transfected sample (containing cells expressing a mixture of all three fluorophores). As a result, the alpha and beta values were recalculated for the co-transfected sample, again from populations of approximately 10 cells each expressing the single fluorophores. The values can fluctuate somewhat due to slight day-to-day differences in the laser spectrum and microscope alignment; however, all results from both days are the same within the standard deviations. The results were as follows: for mAmetrine, $\alpha = 1.06 \pm 0.03$ and $\beta = 17.15 \pm 0.45$; for mKate2, $\alpha = 2.09 \pm 0.03$ and $\beta = 0.32 \pm 0.01$; and for TagRFPT, $\alpha = 2.24 \pm 0.12$ and $\beta = 1.09 \pm 0.03$. The TagRFPT alpha result for this day was taken from the red detection channel rather than the green detection channel because it had a slightly lower standard deviation.

With the alpha and beta values determined for each of the three fluorophores, the linear equation was solved and the three unmixed images were created. Figure 3.8(a) shows the three unmixed images, as well as a false-color merged image, for the sample containing a mixture of singly-expressing cells [31]. The three unmixed images in this figure clearly show that the fluorescence colors can be well-separated using this technique. These results confirm the identifications of which cells express which fluorophores indicated in figure 3.7 and the unmixing shows little overlap between colors, which is expected when each cell expresses only one fluorophore. Furthermore, panel (b) shows the unmixing results when the method is applied to the sample consisting of co-transfected cells. In this sample, each individual cell expresses some

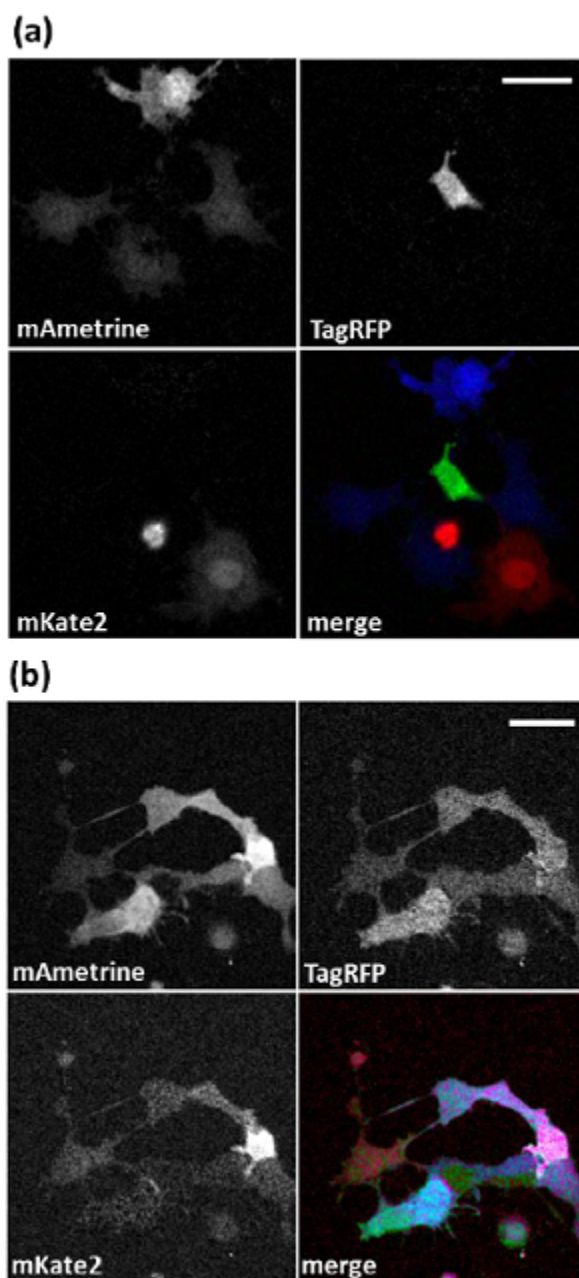


Figure 3.8: Images after linear unmixing. Panel (a) shows the three unmixed images, one for each fluorophore, and a merged image combining all three for the sample containing a mixture of singly-transfected cells. The three colors are well separated. Panel (b) shows the same set of images for the sample containing co-transfected cells; it is apparent here that a broad range of colors is produced. In both panels, mAmetrine, TagRFPt, and mKate2 are pseudo-colored in blue, green, and red respectively. A gamma correction of 0.5 was applied to better show the dimly-labeled cells. Scale bars are $20\ \mu\text{m}$ [31].

random combination of the three fluorophores; this is reflected by the fact that all cells appear in the single-color unmixed images. The mKate2 and TagRFPT fluorophores were not as strongly expressed in the cells as mAmetrine, leading to increased noise in those unmixed images. Because the cells express random mixtures of all three fluorophores, the pseudo-colored merge image of these results shows a wide spectrum of colors.

3.5 Discussion

The results above show the development of a two-photon imaging method that permits selective excitation of three fluorescent proteins using a single broadband femtosecond laser and ultrafast pulse-shaping techniques [31]. When combined with linear unmixing methods and two detection channels, the fluorescent signals from the three fluorophores were well separated and individual cells could be identified. Because this implementation used two phase-shaped pulses for excitation in combination with two detection channels, up to four distinct fluorescent proteins could be unmixed without modifying this technique. The phase-shaping used in this method may also offer benefits in reduced photodamage, depending on the experiment. Photodamage may scale linearly or nonlinearly with peak intensity depending on the sample composition (for example, pigment-rich samples may see predominantly linear photodamage) [44, 45]. The phase-shaped pulses used to achieve high two-photon fluorescence signal have lower peak intensities than TL pulses; this reduces photodamage in samples where nonlinear absorption processes are a significant photodamage mechanism.

An additional benefit to the technique presented here is that it can be easily extended with minimal cost. The key is to have as many imaging conditions as fluorophores to be unmixed. The theory can be adjusted by adding more equations to the set and solving for the needed constants following the steps explained above. Physi-

cally, more imaging conditions can be created by either adding detection channels or adding pulse shapes. Adding shapes has the particular advantage of not increasing the cost of the system, although the setup presented here comes at minimal expense compared to similar experiments. In particular, a single laser is used, which not only reduces the expense but also the complexity of alignment and needs for tabletop space. The method presented here also makes it possible to reduce the number of PMTs needed for imaging, which also greatly reduces the cost of the setup. An additional benefit of this technique is that it relies less on filter optimization than other two-photon fluorescence imaging techniques. Because the excitation conditions are defined by the shaped pulses, the need for excitation filters is eliminated. In addition, only a dichroic is needed to separate the fluorescence signals; the emission bandpass filters that are often used are removed. This is actually a key point - the removal of these filters lets more fluorescence from unwanted wavelengths into a detection channel, increasing the crosstalk between the channels. However, this permits a more accurate determination of the crosstalk constants, in turn leading to an improvement in the unmixing. Thus, the removal of filters not only reduces the expense and planning constraints of the experiment, but actually improves the method overall. This will also increase signal throughput, which is a particular benefit in deep tissue imaging.

There are several potential avenues for future work with this method. One clear option for improvement is to implement an ultrabroadband laser such as a Venteon system with hundreds of nanometers of bandwidth. This would allow access to many more fluorescent proteins and would facilitate imaging samples expressing more than three fluorophores at a time. A simulation of the SH spectrum from such a figure, with potential shaped pulses to excite various fluorophores, is shown in figure 3.1. An additional opportunity for improvement is the use of an overdetermined system of equations. Here, one unneeded image was discarded before unmixing; however,

the method could be changed to include this extra image as a constraint in a least-squares solution. Optimization of the crosstalk constants could be used to improve the unmixing results. Another significant area for future work is in biological applications of the method. One benefit of this linear unmixing technique is that in samples co-expressing multiple fluorophores, the final pseudo-colored results give each cell a unique color based on the amount of each fluorophore it contains. This makes it possible to identify and track single cells based on their colors, in a manner similar to the Brainbow method [11].

References

- [1] B. N. G. Giepmans, S. R. Adams, M. H. Ellisman, and R. Y. Tsien. The fluorescent toolbox for assessing protein location and function. *Science*, 312(5771):217–224, 2006.
- [2] R. Y. Tsien. The green fluorescent protein. *Annual Review of Biochemistry*, 67(1):509–544, 1998. PMID: 9759496.
- [3] N. C. Shaner, P. A. Steinbach, and R. Y. Tsien. A guide to choosing fluorescent proteins. *Nature Methods*, 2(12):905–909, 2005.
- [4] E. R. Tkaczyk and A. H. Tkaczyk. Multiphoton flow cytometry strategies and applications. *Cytometry Part A*, 79A(10):775–788, 2011.
- [5] M. Qian, D. Cai, K. J. Verhey, and B. Tsai. A lipid receptor sorts polyomavirus from the endolysosome to the endoplasmic reticulum to cause infection. *PLoS Pathogens*, 5(6):e1000465, 06 2009.
- [6] D. Cai, D. P. McEwen, J. R. Martens, E. Meyhofer, and K. J. Verhey. Single molecule imaging reveals differences in microtubule track selection between kinesin motors. *PLoS Biology*, 7(10):e1000216, 10 2009.
- [7] J. Lippincott-Schwartz and G. H. Patterson. Photoactivatable fluorescent proteins for diffraction-limited and super-resolution imaging. *Trends in Cell Biology*, 19(11):555 – 565, 2009.
- [8] D. Cai, A. D. Hoppe, J. A. Swanson, and K. J. Verhey. Kinesin-1 structural organization and conformational changes revealed by fret stoichiometry in live cells. *The Journal of Cell Biology*, 176(1):51–63, 2007.
- [9] H. Ai, K. L. Hazelwood, M. W. Davidson, and R. E. Campbell. Fluorescent protein fret pairs for ratiometric imaging of dual biosensors. *Nature Methods*, 5(5):401–403, May 2008.
- [10] T. Kogure, S. Karasawa, T. Araki, K. Saito, M. Kinjo, and A. Miyawaki. A fluorescent variant of a protein from the stony coral montipora facilitates dual-color single-laser fluorescence cross-correlation spectroscopy. *Nature Biotechnology*, 24(5):577–581, June 2006.

- [11] J. Livet, T. A. Weissman, H. Kang, R. W. Draft, J. Lu, R. A. Bennis, J. R. Sanes, and J. W. Lichtman. Transgenic strategies for combinatorial expression of fluorescent proteins in the nervous system. *Nature*, 450(7166):56–62, November 2007.
- [12] H. J. Snippert, L. G. van der Flier, T. Sato, J. H. van Es, M. van den Born, C. Kroon-Veenboer, N. Barker, A. M. Klein, J. van Rheenen, B. D. Simons, and H. Clevers. Intestinal crypt homeostasis results from neutral competition between symmetrically dividing *lgr5* stem cells. *Cell*, 143(1):134 – 144, 2010.
- [13] K. Red-Horse, H. Ueno, I. L. Weissman, and M. A. Krasnow. Coronary arteries form by developmental reprogramming of venous cells. *Nature*, 464(7288):549–553, March 2010.
- [14] G. Feng, R. H. Mellor, M. Bernstein, C. Keller-Peck, Q. T. Nguyen, M. Wallace, J. M. Nerbonne, J. W. Lichtman, and J. R. Sanes. Imaging neuronal subsets in transgenic mice expressing multiple spectral variants of *gfp*. *Neuron*, 28(1):41 – 51, 2000.
- [15] T. Misgeld, M. Kerschensteiner, F. M. Bareyre, R. W. Burgess, and J. W. Lichtman. Imaging axonal transport of mitochondria in vivo. *Nature Methods*, 4(7):559–561, July 2007.
- [16] W. Denk, J. H. Strickler, and W. W. Webb. Two-photon laser scanning fluorescence microscopy. *Science*, 248(4951):73–76, 1990.
- [17] W. Denk. Two-photon excitation in functional biological imaging. *Journal of Biomedical Optics*, 1(3):296–304, 1996.
- [18] W. R. Zipfel, R. M. Williams, and W. W. Webb. Nonlinear magic: multiphoton microscopy in the biosciences. *Nature Biotechnology*, 21(11):1369–1377, 2003.
- [19] E. Sahai, J. Wyckoff, U. Philippar, J. E. Segall, F. Gertler, and J. Condeelis. Simultaneous imaging of *gfp*, *cfp*, and collagen in tumors in vivo using multiphoton microscopy. *BMC Biotechnology*, 5(14), 2005.
- [20] H. Kawano, T. Kogure, Y. Abe, H. Mizuno, and A. Miyawaki. Two-photon dual-color imaging using fluorescent proteins. *Nature Methods*, 5(5):373–374, May 2008.
- [21] S.E. Tillo, T.E. Hughes, N.S. Makarov, A. Rebane, and M. Drobizhev. A new approach to dual-color two-photon microscopy with fluorescent proteins. *BMC Biotechnology*, 10(6), 2010.
- [22] M. Drobizhev, N. S. Makarov, S. E. Tillo, T. E. Hughes, and A. Rebane. Two-photon absorption properties of fluorescent proteins. *Nature Methods*, 8(5):393–399, May 2011.

- [23] D. Entenberg, J. Wyckoff, B. Gligorijevic, E. T. Roussos, V. V. Verkhusha, J. W. Pollard, and J. Condeelis. Setup and use of a two-laser multiphoton microscope for multichannel intravital fluorescence imaging. *Nature Protocols*, 6(10):1500–1520, October 2011.
- [24] P. Mahou, M. Zimmerley, K. Loulier, K. S. Matho, G. Labroille, X. Morin, W. Supatto, J. Livet, D. Debarre, and E. Beaurepaire. Multicolor two-photon tissue imaging by wavelength mixing. *Nature Methods*, 9(8):815–818, August 2012.
- [25] J. W. Boardman. Inversion of imaging spectrometry data using singular value decomposition. In *Geoscience and Remote Sensing Symposium, 1989. IGARSS'89. 12th Canadian Symposium on Remote Sensing., 1989 International*, volume 4, pages 2069–2072, jul 1989.
- [26] T. Zimmermann, J. Rietdorf, and R. Pepperkok. Spectral imaging and its applications in live cell microscopy. *FEBS Letters*, 546(1):87–92, 2003.
- [27] R. Lansford, G. Bearman, and S. E. Fraser. Resolution of multiple green fluorescent protein color variants and dyes using two-photon microscopy and imaging spectroscopy. *Journal of Biomedical Optics*, 6(3):311–318, 2001.
- [28] H. Tsurui, H. Nishimura, S. Hattori, S. Hirose, K. Okumura, and T. Shirai. Seven-color fluorescence imaging of tissue samples based on fourier spectroscopy and singular value decomposition. *Journal of Histochemistry & Cytochemistry*, 48(5):653–662, 2000.
- [29] Y. Hiraoka, T. Shimi, and T. Haraguchi. Multispectral imaging fluorescence microscopy for living cells. *Cell Structure and Function*, 27(5):367–374, 2002.
- [30] M. E. Dickinson, E. Simbuerger, B. Zimmermann, C. W. Waters, and S. E. Fraser. Multiphoton excitation spectra in biological samples. *Journal of Biomedical Optics*, 8(3):329–338, 2003.
- [31] M. H. Brenner, D. Cai, J. A. Swanson, and J. P. Ogilvie. Two-photon imaging of multiple fluorescent proteins by phase-shaping and linear unmixing with a single broadband laser. *Optics Express*, 21(14):17256–17264, Jul 2013.
- [32] S. Kramer-Hämmerle, F. Ceccherini-Silberstein, C. Bickel, H. Wolff, M. Vincendeau, T. Werner, V. Erfle, and R. Brack-Werner. Identification of a novel rev-interacting cellular protein. *BMC Cell Biology*, 6(20), 2005.
- [33] B. Kraus, M. Zeigler, and H. Wolff. Linear fluorescence unmixing in cell biological research. *Modern Research and Educational Topics in Microscopy*, 2:863–873, 2007.
- [34] J. M. Dela Cruz, V. V. Lozovoy, and M. Dantus. Coherent control improves biomedical imaging with ultrashort shaped pulses. *Journal of Photochemistry and Photobiology A: Chemistry*, 180(3):307–313, 2006.

- [35] Y. Coello, V. V. Lozovoy, T. C. Gunaratne, B. Xu, I. Borukhovich, C. Tseng, T. Weinacht, and M. Dantus. Interference without an interferometer: a different approach to measuring, compressing, and shaping ultrashort laser pulses. *JOSA B*, 25(6):A140–A150, 2008.
- [36] V. V. Lozovoy, I. Pastirk, and M. Dantus. Multiphoton intrapulse interference. iv. ultrashort laser pulse spectral phase characterization and compensation. *Optics Letters*, 29(7):775–777, 2004.
- [37] B. Xu, J. M. Gunn, J. M. Dela Cruz, V. V. Lozovoy, and M. Dantus. Quantitative investigation of the multiphoton intrapulse interference phase scan method for simultaneous phase measurement and compensation of femtosecond laser pulses. *JOSA B*, 23(4):750–759, 2006.
- [38] D. Shcherbo, C. S. Murphy, G. V. Ermakova, E. A. Solovieva, T. V. Chepurnykh, A. S. Shcheglov, V. V. Verkhusha, V. Z. Pletnev, K. L. Hazelwood, P. M. Roche, S. Lukyanov, A. G. Zaraisky, M. W. Davidson, and D. M. Chudakov. Far-red fluorescent tags for protein imaging in living tissues. *The Biochemical Journal*, 418(3):567–574, 2009.
- [39] E. M. Merzlyak, J. Goedhart, D. Shcherbo, M. E. Bulina, A. S. Shcheglov, A. F. Fradkov, A. Gaintzeva, K. A. Lukyanov, S. Lukyanov, T. W. J. Gadella, and D. M. Chudakov. Bright monomeric red fluorescent protein with an extended fluorescence lifetime. *Nature Methods*, 4(7):555–557, 2007.
- [40] N. C. Shaner, M. Z. Lin, M. R. McKeown, P. A. Steinbach, K. L. Hazelwood, M. W. Davidson, and R. Y. Tsien. Improving the photostability of bright monomeric orange and red fluorescent proteins. *Nature Methods*, 5(6):545–551, 2008.
- [41] M. Drobizhev, N. S. Makarov, T. Hughes, and A. Rebane. Resonance enhancement of two-photon absorption in fluorescent proteins. *The Journal of Physical Chemistry B*, 111(50):14051–14054, 2007.
- [42] E. Salomonsson, L. A. Mihalko, V. V. Verkhusha, K. E. Luker, and G. D. Luker. Cell-based and in vivo spectral analysis of fluorescent proteins for multiphoton microscopy. *Journal of Biomedical Optics*, 17(9):0960011–0960019, 2012.
- [43] M. Comstock, V. Lozovoy, I. Pastirk, and M. Dantus. Multiphoton intrapulse interference 6; binary phase shaping. *Optics Express*, 12(6):1061–1066, 2004.
- [44] H. J. Koester, D. Baur, R. Uhl, and S. W. Hell. Ca²⁺ fluorescence imaging with pico- and femtosecond two-photon excitation: signal and photodamage. *Biophysical Journal*, 77(4):2226–2236, 1999.
- [45] D. Pestov, Y. Andegeko, V. V. Lozovoy, and M. Dantus. Photobleaching and photoenhancement of endogenous fluorescence observed in two-photon microscopy with broadband laser sources. *Journal of Optics*, 12(8), 2010.

CHAPTER IV

Fluorescence Resonance Energy Transfer

4.1 Introduction

As multiphoton microscopy has gained prevalence in the biological sciences, many variations on its basic theme have been developed to accomplish specific goals. One of the areas that has seen intense work is the adaptation of Fluorescence Resonance Energy Transfer (FRET) to two-photon microscopy systems. FRET occurs when an excited “donor” fluorophore is spatially close enough to an “acceptor” fluorophore in the ground state such that a dipole-dipole interaction enables the transfer of energy from the donor to the acceptor. This results in the acceptor molecule fluorescing rather than the donor. Not surprisingly this effect is strongly distance-dependent; its efficiency falls off as $\frac{1}{R^6}$ where R is the separation between the fluorophores [1]. Consequently, by monitoring changes in fluorescence signals due to FRET, it is possible to monitor the FRET efficiency and by extension the separation of the fluorophores. This has earned FRET a reputation as a “spectroscopic ruler,” as Stryer and Haugland called it in their 1967 study of the distance dependence [2]. A number of experiments have exploited this behavior to investigate biological systems, particularly studies of biological structures and interactions between molecules.

An interesting demonstration of FRET in a solution-based study that illustrates the power of its distance dependence is the investigation of the conformation states of

four-way DNA junctions conducted by Clegg *et al.* [3, 4]. It was thought that under low-salt conditions, these junctions had a square shape with four arms separated by ninety degrees; upon addition of salt ions, the structure was thought to fold into an X shape. Adjacent arms of the structure were labeled with donor and acceptor fluorophores and the acceptor fluorescence signal was monitored under different salt concentrations; the FRET efficiency increased with the salt concentration, indicating that the two arms were moving closer to each other [3]. Furthermore, the square shape in low-salt conditions was confirmed by comparing the FRET efficiencies with the fluorophore placed on different pairs of arms, with arms separated by 90° having higher FRET efficiency than arms separated by 180° [4]. These results clearly show the utility of FRET as a way to measure relative distances in biological systems.

A number of innovative studies taking advantage of FRET's distance dependence have been performed in the microscope as well. An early study used FRET images to examine the aggregation of lectin proteins on cell surfaces and how DNA dyes distribute themselves along polytene chromosomes [5]. A later study investigated the structure and compartmentalization of the cholera toxin in live cells [6]. This was achieved by labeling a subunit of the toxin with a fluorescent donor molecule and an antibody with the acceptor; the FRET efficiency changed as the toxin moved through the cell, allowing the researchers to determine its final position and conformation.

As the popularity of FRET grew, a natural extension was to implement two-photon excitation as the initial excitation of the donor. This provides all the benefits that two-photon excitation possesses over one-photon excitation, including reduced photodamage and photobleaching, increased penetration depth in tissues, and intrinsic sectioning ability [7–10]. These benefits are discussed in detail in Chapter I of this thesis. It should be noted that fluorophores show the same fluorescence lifetime and emission spectra under two-photon excitation as under one-photon [1], so utilizing two-photon excitation will not change the FRET process. An early demonstration

of two-photon FRET pointed out that it can be used to increase the effective two-photon absorption of fluorophores by coupling them as acceptors to donors with high two-photon absorption and then relying on the transfer process to generate the acceptor fluorescence [11]. Two-photon excited FRET has been used to study a wide range of biological systems, including protein interactions involved in traumatic brain injuries [12], intranuclear dimer formation of transcription factors in pituitary cells [13], and receptor-ligand complex clustering in apical endocytic membranes of MDCK cells [14].

Given the potential of FRET for observing dynamics in cellular systems, it is worthwhile to investigate potential applications of ultrafast pulse shaping to FRET methods. This chapter and the next outline two approaches to implementing pulse shaping in two-photon FRET. This chapter begins by giving an overview of the history and theory of Fluorescence Resonance Energy Transfer. It then describes experiments demonstrating that ultrafast pulse shaping can be applied to two-photon FRET microscopy to distinguish between FRET and non-FRET conditions in live cells.

4.2 Fluorescence Resonance Energy Transfer

The theory of Fluorescence Resonance Energy Transfer was first developed by Theodore Forster classically in 1946 and expanded quantum mechanically in 1948 [15, 16]. His work describes the nonradiative transfer of energy from an excited fluorescent donor molecule to an acceptor molecule in its ground state via an induced dipole-dipole interaction. A common misconception is that the energy is transferred by the donor emitting a photon which is subsequently absorbed by the acceptor; this is not the case and is the reason why it is important to note that it is a nonradiative process. The process is sometimes called Forster Resonance Energy Transfer to clarify this distinction [1]. Figure 4.1 shows a Jablonski diagram illustrating the energy

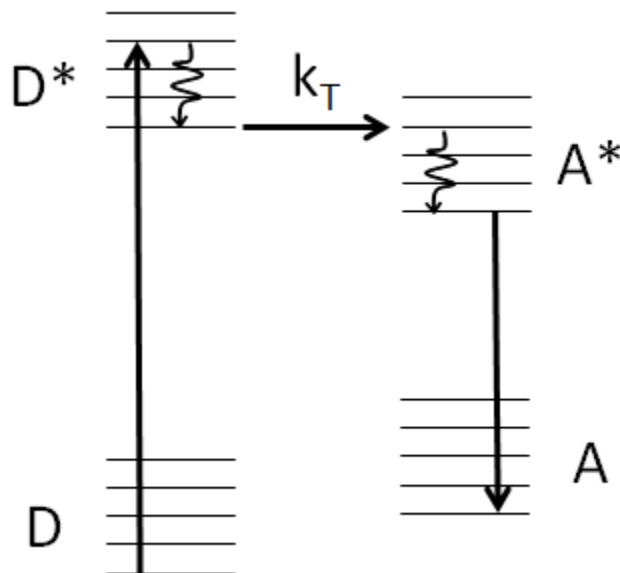


Figure 4.1: Jablonski diagram of FRET process. The donor molecule starts in its ground state D and is excited to its state D^* . After vibrational relaxation, energy is transferred to the acceptor at a rate k_T . The acceptor then undergoes relaxation to the lowest vibrational level of the first electronic excited state before emitting a photon and returning to the ground state. Adapted from [17].

transfer process. The donor is excited from the ground state D by absorption of a photon; it then relaxes to the lowest vibrational level of the excited state D^* . From here, rather than transitioning back to the ground state by emission of a photon, the energy may be transferred at a rate k_T to the acceptor. This excites the acceptor, which rapidly relaxes to the lowest vibrational level of its first electronic excited state A^* , preventing the energy from transferring back to the donor. Finally, the acceptor emits a photon and decays to the ground state A [17]. The acceptor does not need to be fluorescent for FRET to occur; the final relaxation can also be nonradiative.

The characteristics of FRET, including its efficiency, are derived from a rate equation for k_T . The rate is found by applying Fermi's Golden Rule to the transition between states (D^*, A) and (D, A^*) [17–19]. FRET occurs when the incident electric field induces a dipole in the donor, which in turn induces a dipole in the acceptor.

The interaction energy for this situation is given by

$$V \propto \frac{1}{n^2} \left(\frac{\vec{\mu}_D \cdot \vec{\mu}_A}{R^3} - \frac{3(\vec{\mu}_D \cdot \vec{R})(\vec{R} \cdot \vec{\mu}_A)}{R^5} \right) \quad (4.1)$$

where \vec{R} is the vector representing the distance between the two dipoles and $\vec{\mu}_D$ and $\vec{\mu}_A$ are the donor and acceptor dipole moments, respectively [17, 19]. Here, the $\frac{1}{n^2}$ term appears to account for the index of refraction of the medium. This potential can be simplified by combining all terms related to the orientation of the dipoles into the variable κ ; this leads to an interaction energy of the form [17–19]

$$V \propto \frac{\kappa}{n^2} \frac{|\vec{\mu}_D||\vec{\mu}_A|}{R^3} \quad (4.2)$$

It is assumed that the interaction between the donor and acceptor is weak enough such that their individual wavefunctions are not perturbed [17, 18]. According to Fermi's Golden Rule,

$$k_T \propto |\langle D^* A | V | D A^* \rangle|^2 \quad (4.3)$$

so the rate of energy transfer k_T is given by the matrix element of the interaction energy. Solving this for the given dipole-dipole interaction yields the final rate [16–18, 20]

$$k_T = \frac{1}{\tau_D} \left(\frac{R_0}{R} \right)^6 \quad (4.4)$$

In this rate equation, τ_D is the fluorescence lifetime of the donor and R_0 is the Forster radius, the separation distance at which the FRET efficiency falls to 50%. This form already shows the well-known $1/R^6$ distance dependence of FRET. The Forster radius

is given (in units of angstroms) as [17]

$$R_0 = \left(8.79 \times 10^{-5} \frac{J \kappa^2 \phi_D}{n^4} \right)^{\frac{1}{6}} \quad (4.5)$$

where ϕ_D is the donor quantum yield. J is the overlap integral, the mathematical representation of the requirement that the donor's emission spectrum overlaps with the acceptor's excitation spectrum. J depends on ϵ_A , the acceptor's extinction coefficient, as well as f_D , the donor emission [17]. J can be calculated from

$$J = \frac{\int \epsilon_A(\lambda) f_D(\lambda) \lambda^4 d\lambda}{\int f_D(\lambda) d\lambda} \quad (4.6)$$

which is in units of $M^{-1} cm^{-1} nm^4$ [17]. Using this rate for energy transfer, it is possible to find the FRET efficiency. The donor does not have to undergo FRET; it can relax from its excited state by any of several pathways, each with its own rate k_i . This means the efficiency of FRET is given by [19]

$$E = \frac{k_T}{k_T + \sum_{i \neq T} k_i} = \frac{k_T}{k_T + \frac{1}{\tau_D}} \quad (4.7)$$

Substitution of the rate found in (4.4) leads to the well-known equation for the FRET efficiency [17–20]:

$$E = \frac{1}{1 + (R/R_0)^6} \quad (4.8)$$

This form for the efficiency highlights that the Forster Radius is the distance at which the FRET efficiency falls to 50%; this varies depending on the fluorophores used but is often in the range of 5-100 Angstrom [17, 18, 20].

It is important to consider the role of the orientation factor κ^2 in FRET. Because both fluorophores act as electric dipoles, their relative angular orientations affect the

efficiency of the energy transfer process. The value of this orientation factor can vary from 0 to 4 depending on the positions of the molecules, and as a result it is a potential source of error in calculations of the Forster Radius or FRET efficiency [17, 18, 20]. It is often assumed that both fluorophores have rotational freedom and can re-orient rapidly compared to the lifetime of the excited donor, in which case κ averages to a value of $2/3$. This assumption may not always hold, but studies have shown that it is a good approximation in many cases [17, 18, 20].

FRET can be detected experimentally in a variety of ways. One method is to determine the increase in acceptor fluorescence when the donor is present compared to when the acceptor is alone, as when FRET is occurring there is an increase in acceptor signal. Similarly, it is possible to quantify the decrease in donor fluorescence when the acceptor is introduced to the sample, as energy being transferred to the acceptor decreases the energy available for the donor to emit as fluorescence. A third method is investigation of the fluorescence lifetime of the donor, as when FRET is occurring this lifetime is decreased [1, 21]. In the next section, a method for detection of FRET using ultrafast pulse shaping for selective excitation is presented [22, 23].

4.3 Detection of FRET Using Pulse Shaping

4.3.1 Introduction

A key requirement for FRET to occur is the overlap of the donor's emission spectrum with the acceptor's excitation spectrum; this ensures that energy can be transferred. When this is large, it can yield an improved FRET efficiency; however, it can also lead to direct overlap between both fluorophores' excitation or emission spectra. This spectral overlap can complicate FRET experiments. If the two emission spectra overlap, then it is possible to record donor fluorescence signal in the acceptor detection channel or vice versa. If the two excitation spectra overlap, then the ac-

ceptor may be directly excited by conditions meant to excite only the donor, leading to acceptor fluorescence that is mistakenly recorded as being due to energy transfer. Such spectral crosstalk must be either corrected for or avoided in order to obtain accurate FRET measurements, and one way to try to avoid it is through selective excitation.

In one-photon FRET experiments, selective excitation can be achieved by careful selection of the fluorophores in the FRET pair and appropriate filters. Separation between parts of the excitation spectra and filters placed in spectral regions where the excitation spectrum of one of the fluorophores dominates can provide good discrimination. However, in two-photon FRET experiments this can be more difficult to achieve. The introduction of filters leads to the amplitude shaping conditions discussed in the pulse shaping chapter of this thesis, which results in a lengthened pulse in time and lower two-photon fluorescence signal. Multicolor imaging in two-photon microscopy has been performed using other excitation schemes, but they do not lend well to selective excitation. For example, the use of ultrabroadband titanium:sapphire oscillators permits excitation of multiple fluorophores via a transform-limited (TL) pulse [24]. However, this excites all fluorophores present simultaneously; this will lead to strong direct excitation of the acceptor and make it difficult to separate that fluorescence from signal due to FRET. Another option is the use of tunable femtosecond lasers [25]. While these will allow selective excitation, the relatively long tuning time (on the order of seconds to minutes) makes this method difficult to apply to rapidly-changing biological systems. As one of the benefits of FRET is its ability to monitor how systems interact over time, a loss of temporal resolution decreases its utility.

Fortunately, ultrafast pulse shaping is a technique which easily permits rapid selective excitation in multicolor two-photon imaging. When a Spatial Light Modulator (SLM) is used to perform phase-only shaping, masks can be changed in as little as 10

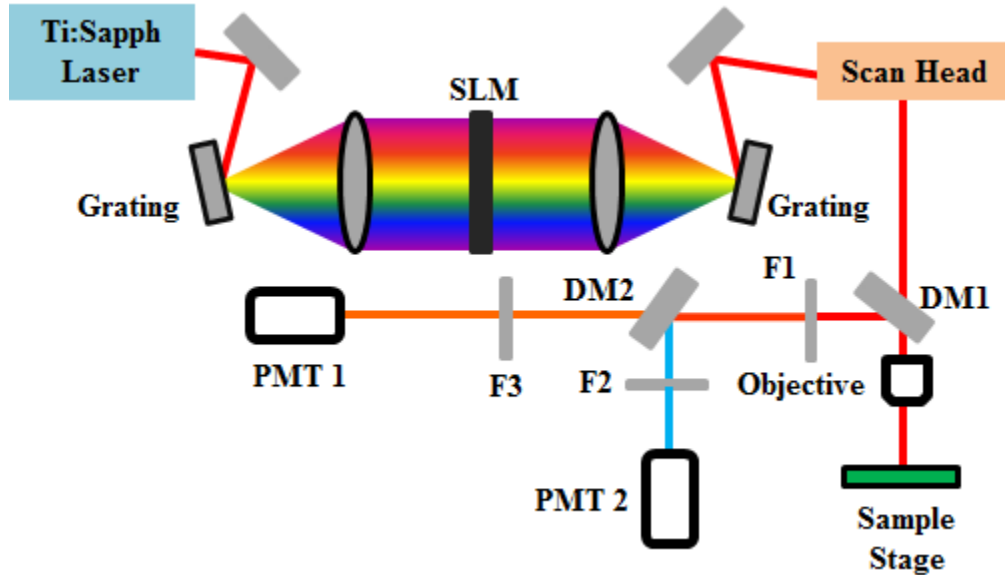


Figure 4.2: Experimental setup for detection of FRET. SLM = spatial light modulator, DM1 = 660DCXR dichroic mirror, DM2 = 595DCXR dichroic mirror, F1 = 650 nm short pass filter, F2 = 480/40 filter, F3 = 630/75 filter [22].

ms [26], greatly improving the potential time resolution of the experiment. Selective excitation using pulse shaping has been successfully demonstrated in a number of systems, such as excitation of fluorescent proteins over autofluorescence [27, 28] and enhancement of fluorescence from specific fluorophores [29–31]. Pulse shaping methods have also been used to image a calcium-based FRET indicator [32]. Here, a method is presented for selective excitation of fluorescent proteins in live cells using pulse shaping to distinguish between FRET and non-FRET conditions, as published in [22, 23]. This selective excitation paves the way for implementation of FRET stoichiometry as a way to quantify the FRET results.

4.3.2 Experimental Methods

The experimental setup used for this demonstration is shown in figure 4.2[22]. A 75 MHz Femtolasers Synergy titanium:sapphire (ti:sapph) oscillator with 110 nm bandwidth centered at 780 nm was aligned into a transmissive 4f pulse shaper setup. A CRi 640 pixel, phase-only spatial light modulator (SLM) was controlled via Matlab

and used to apply phase masks. For imaging, the shaped beam was sent into a Prairie Technologies modified Olympus BX51WI upright microscope and an Olympus UPlanApo 60x, 1.2NA water-immersion objective was used to focus on the sample. A variable neutral density filter was used in the beam path to control the power; at the sample it was approximately 5.5 mW. The objective recollected the fluorescence signal, which was then separated from the excitation light by a dichroic mirror and a shortpass filter. A second dichroic and bandpass filters then split the fluorescence into two PMT channels for detection.

Dispersion of the optics in the setup, including the objective, was compensated using Multiphoton Intrapulse Interference Phase Scan (MIIPS) [33–35]; more details on this technique can be found in Chapter 2 of this thesis. To perform MIIPS measurements, a 1 mm thick beta barium borate (BBO) crystal was mounted on a #1 thickness glass coverslip and placed at the focus of the microscope. The coverslip protected the crystal from the water required for the objective immersion. The second harmonic generated light from this crystal was then separated from the fundamental and coupled into a compact spectrometer for detection; Matlab code written in-house was then used to perform the MIIPS routine. To achieve a transform-limited (TL) baseline, the result of the MIIPS process was applied to the SLM before application of additional shapes.

Samples used in this experiment were two sets of COS-7 cells expressing the fluorescent proteins mCerulean as the donor fluorophore and mCherry as the acceptor fluorophore. One sample consisted of cells expressing both fluorophores, but not in complex, such that no FRET would occur; this was the “unlinked” sample. The cells in the second sample expressed a construct of the two fluorophores separated by a linker of 27 amino acids; this construct had a FRET efficiency of 22.19% as measured by FLIM-FRET [36, 37] and was the “linked” sample. To create these samples, COS-7 cells were grown on 100 mm tissue culture dishes with 10 mL Dulbecco’s Modified

Eagle’s Medium (DMEM) supplemented with 10% fetal bovine serum and 1% each Penicillin-Streptomycin and GlutaMAX glutamine. Once confluent, the media was removed and the dish was rinsed with 5 mL Phosphate-Buffered Saline (PBS) at pH 7.4. After rinsing, 1 mL of 0.25% Trypsin-EDTA was added and the dish was placed in the incubator for a few minutes to loosen the cells. Once the cells detached, the Trypsin-EDTA was nullified by the addition of 9 mL of media. The cells were then counted with a hemacytometer and approximately 120,000 cells were added to each of two 35 mm tissue culture dishes; these were then filled to 2 mL with media and allowed to incubate for 24 hours. For transfection, 100 μ L of Opti-Mem reduced serum media was placed in each of two small eppendorf tubes. For the linked sample, approximately 0.5 μ g of the purified plasmid DNA was added to the tube. For the unlinked sample, approximately 0.25 μ g of each of the two single fluorophores’ DNA was added to the tube. Finally, 6 μ L of FuGene 6 transfection reagent was added to each tube and they were incubated at room temperature for 15 minutes. After incubation, these solutions were added drop-wise to separate dishes of COS-7 cells. The cells were incubated for 24 hours to allow for expression of the fluorescent proteins. Just before imaging, the media was replaced with Ringer’s Buffer. During imaging, the cells were kept at 37 $^{\circ}$ C and the water-immersion objective was submerged directly into the buffer in the dish.

Two pulse shapes were designed to perform selective excitation, one to preferentially excite mCerulean and one to preferentially excite mCherry. The designs were based on the two-photon absorption spectra of the fluorophores, which are shown in figure 4.3 [24]. This illustrates that mCherry has a recently discovered peak in its absorption spectrum corresponding to an $S_0 - S_N$ transition [24]; the mCherry pulse was designed to take advantage of this and is thus centered at shorter wavelengths than the mCerulean pulse. Figure 4.4 shows the second harmonic spectra of the TL pulse and the two shaped pulses [22]. To design the phase masks, binary phase shap-

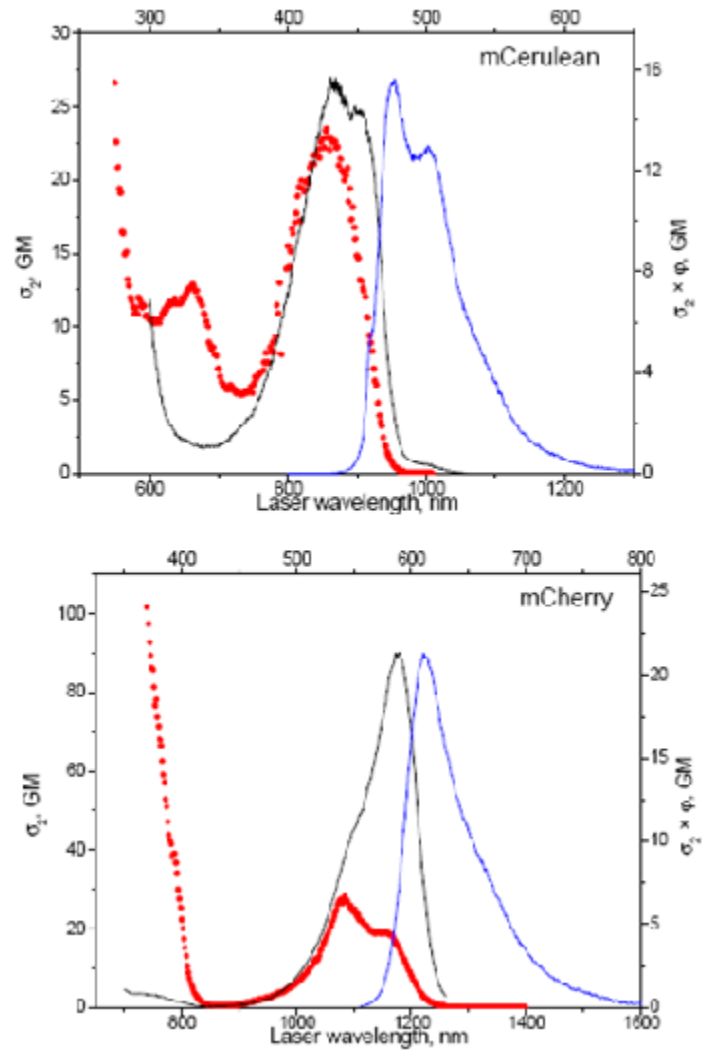


Figure 4.3: Two-photon absorption spectra of mCerulean and mCherry. The one-photon absorption curve is shown in black, the two-photon absorption is in red, and the fluorescence emission spectrum is in blue. mCerulean is in the top panel and mCherry is in the bottom panel. Taken from [24].

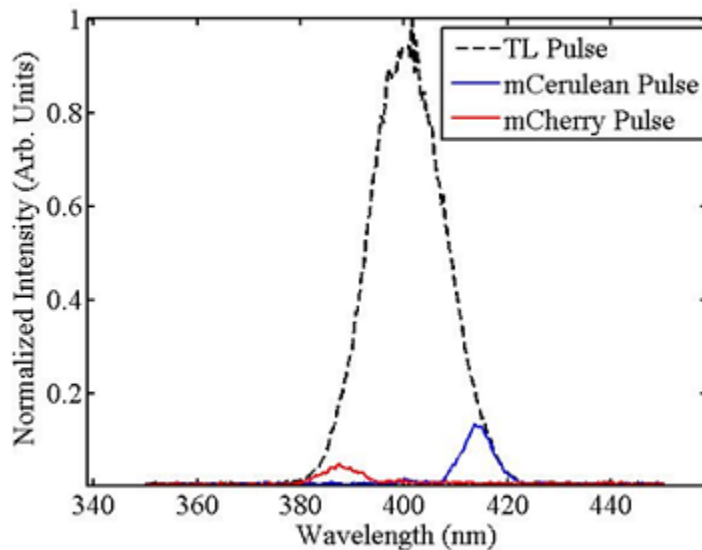


Figure 4.4: Second harmonic spectra of the shaped pulses. To take advantage of its large two-photon absorption, the mCherry pulse is centered at shorter wavelengths than the mCerulean pulse [22].

ing was used similarly to techniques demonstrated in Comstock *et al.* [38]. Masks consisted of a random pattern where every pixel had a phase value of either 0 or π ; this pattern was symmetric around a flat phase section of approximately 40 nm. The center of the flat phase section was located at twice the desired second harmonic peak wavelength of the shaped pulse. During imaging, the shaped pulses as well as the TL pulse were applied to multiple cells in each sample. The order in which the shapes were applied was alternated to eliminate effects that could be caused by photobleaching, and the TL pulse was always applied last. Individual cells were chosen in small regions of interest, and images were acquired as averages of 128 frames using 4 μ s per pixel dwell times. Prairie Technologies' PrairieView software was used for image acquisition, and subsequent analysis was performed in Matlab. Background images taken under the same imaging conditions with the laser beam blocked were used for background subtraction, and cells were masked during analysis so that only the central bright portions were used for calculations.

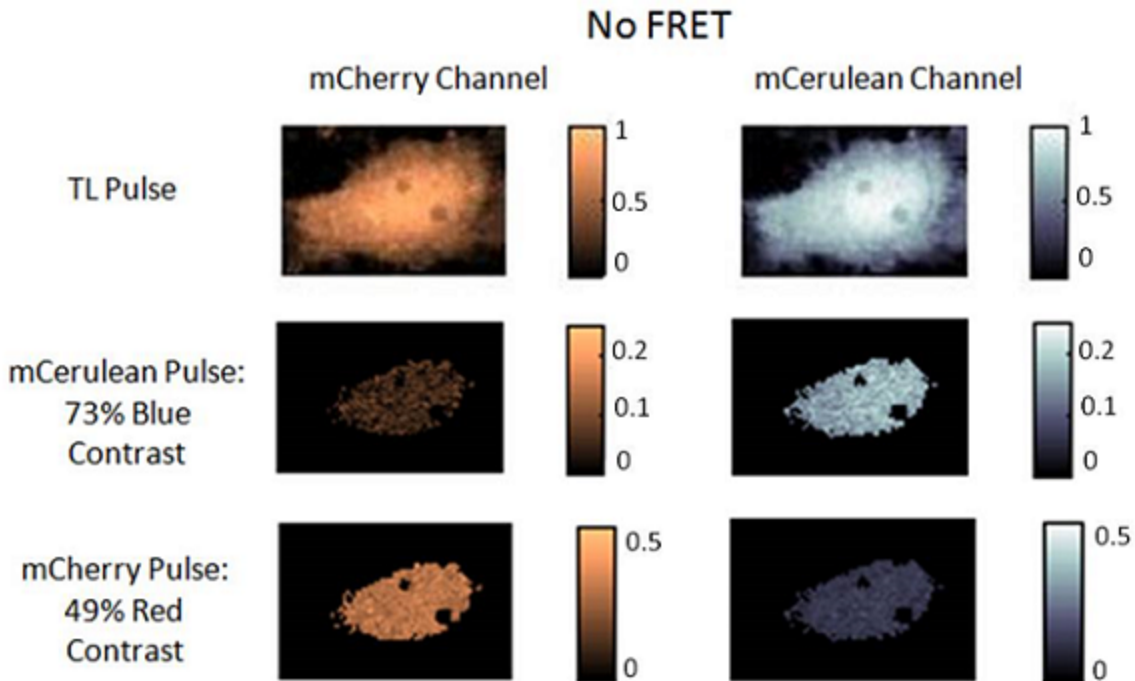


Figure 4.5: Demonstration of selective excitation in the No FRET condition. The left column displays the images from the mCherry channel and the right column displays the images from the mCerulean channel. The top row shows fluorescence excited by the TL pulse, the middle row is from the mCerulean pulse, and the bottom row is from the mCherry pulse [22].

4.3.3 Results and Discussion

The unlinked set of cells, which make up the “No FRET” condition, were imaged first. These cells were co-transfected with both the donor and acceptor but because the fluorophores are not linked, no FRET is expected. The results are shown in figure 4.5, which shows the mCherry fluorescence in the left column and the mCerulean fluorescence in the right column [22]. Images taken under excitation by the TL pulse are shown in the top row; as expected, this pulse excites both fluorophores with little distinction between the two. The middle and bottom rows show images of the same cell taken with the shaped pulses used for excitation. These images have been masked so that only the central bright region is shown and used for calculations; they have also been normalized to the TL image intensity to account for differences in

brightness and transfection efficiency between the two fluorophores. Contrast values were calculated from these image intensities with the following definitions:

$$\text{Blue Contrast} = \frac{m\text{Cerulean Fluorescence} - m\text{Cherry Fluorescence}}{m\text{Cerulean Fluorescence}} \quad (4.9)$$

$$\text{Red Contrast} = \frac{m\text{Cherry Fluorescence} - m\text{Cerulean Fluorescence}}{m\text{Cherry Fluorescence}} \quad (4.10)$$

where blue contrast is found when the mCerulean pulse shape is applied and red contrast is found when the mCherry pulse shape is applied. As figure 4.5 shows in the middle row, when the shape tuned to preferentially excite mCerulean was used for excitation, blue contrast of 73% was seen. In the bottom row, it can be seen that when the mCherry pulse shape is used, red contrast of 49% resulted. Similar results were obtained across multiple cells and repeated applications of the pulse shapes. This demonstrates that the shaped pulses do provide selective excitation of the target fluorophores compared to the TL pulse.

Next, cells in the FRET condition were imaged. These cells expressed the linked construct of the donor mCerulean and acceptor mCherry designed to facilitate FRET. Under these conditions, the use of the shaped pulses for selective excitation is expected to yield slightly different results compared to the No FRET condition. When the mCerulean pulse is used for excitation, the excited donor will transfer some of its energy to the acceptor in the energy transfer process, causing a decrease in donor fluorescence and an increase in acceptor fluorescence. This will result in a decrease in blue contrast compared to the No FRET condition. However, when the pulse designed to excite mCherry is used, some of the donor fluorophores will still be excited due to spectral overlap of the fluorophores' two-photon absorption spectra. These excited donor molecules can still transfer energy to the acceptor, resulting again in an increase of acceptor fluorescence and a decrease in donor fluorescence. Thus, an increase in the red contrast compared to the No FRET condition is expected when the mCherry

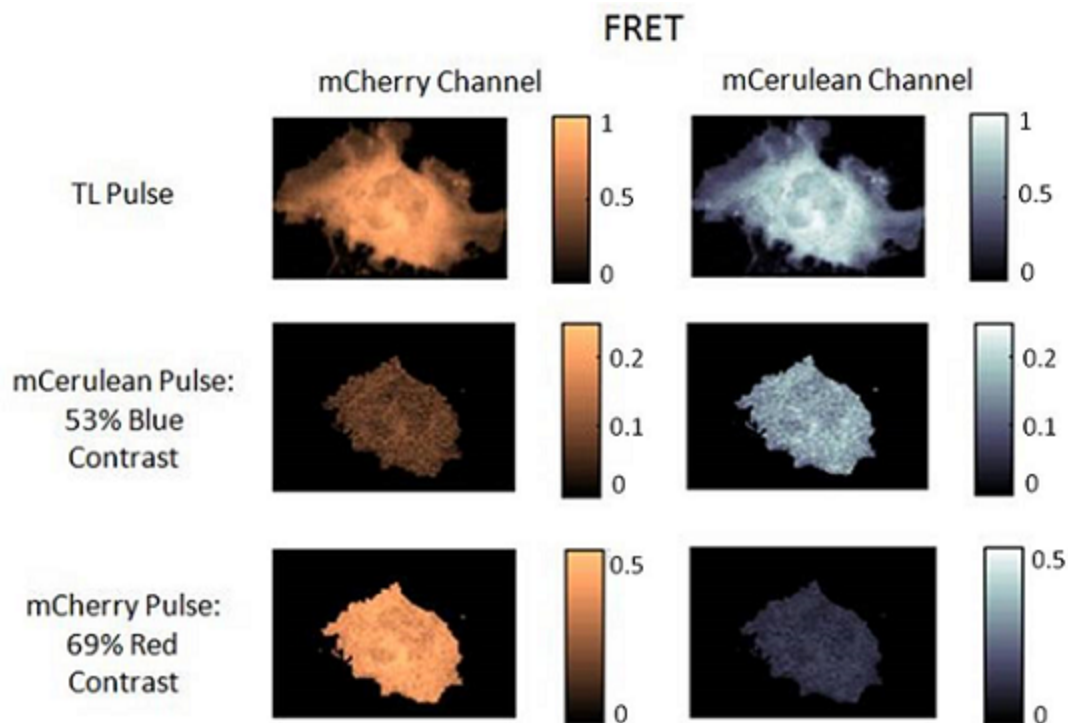


Figure 4.6: Demonstration of selective excitation in the FRET condition. The left column displays the images from the mCherry channel and the right column displays the images from the mCerulean channel. The top row shows fluorescence excited by the TL pulse, the middle row is from the mCerulean pulse, and the bottom row is from the mCherry pulse [22, 23].

pulse shape is used for excitation.

The images shown in figure 4.6 are taken from the linked sample and support these hypotheses [22, 23]. As before, the top row shows excitation by the TL pulse, the middle row shows excitation by the mCerulean pulse shape, and the bottom row shows excitation by the mCherry pulse shape. The left column shows the mCherry fluorescence and the right column shows the mCerulean fluorescence. The images are masked again to consider only the central bright regions, and as before they are normalized to the TL image intensity. As in the No FRET condition, excitation by the TL pulse leads to bright fluorescence from both donor and acceptor but little distinction between them. In the middle row, excitation with the mCerulean pulse

shape leads to the expected decrease in blue contrast compared to the No FRET samples, with it decreasing from 73% to 53%. Excitation with the mCherry pulse is shown in the bottom row; the red contrast increased from 49% to 69% between the two sample types. Multiple cells and repeated applications of the shaped pulses showed similar results.

This demonstrates that selective excitation via ultrafast pulse shaping works when applied to two fluorophores in a linked construct in live cells. Furthermore, it shows that this pulse-shaping-based method is able to distinguish between a FRET and non-FRET condition in live cells [22, 23]. The use of ultrafast pulse shaping gives this method improved temporal resolution compared to other two-photon FRET modalities, facilitating the study of biological interactions. While this method permits the study of cellular systems by monitoring the extent of FRET via changes in contrast, it does not provide quantitative results. This is actually a common problem in FRET studies - while some measurements of FRET efficiency and separation distance can be obtained, they are usually in arbitrary units and only meaningful in the experiment at hand. For FRET studies to be truly useful, they should provide more quantitative information such as stoichiometric data. Techniques to quantify FRET exist, but they have generally been limited to one-photon FRET. The extension of quantitative FRET microscopy methods to two-photon FRET by implementing ultrafast pulse shaping is the subject of the next chapter.

References

- [1] J. R. Lakowicz. *Principles of Fluorescence Spectroscopy*. Springer, 2007.
- [2] L. Stryer and R. P. Haugland. Energy transfer: a spectroscopic ruler. *Proceedings of the National Academy of Sciences of the United States of America*, 58(2):719–726, 1967.
- [3] R. M Clegg, A. I. H. Murchie, A. Zechel, C. Carlberg, S. Diekmann, and D. M. J. Lilley. Fluorescence resonance energy transfer analysis of the structure of the four-way dna junction. *Biochemistry*, 31(20):4846–4856, 1992.
- [4] R. M. Clegg, A. I. Murchie, and D. M. Lilley. The solution structure of the four-way dna junction at low-salt conditions: a fluorescence resonance energy transfer analysis. *Biophysical Journal*, 66(1):99–109, 1994.
- [5] T. M. Jovin and D. J. Arndt-Jovin. Fret microscopy: digital imaging of fluorescence resonance energy transfer. application in cell biology. In *Cell Structure and Function by Microspectrofluorometry*, volume 30, pages 99–117. Academic Press: London, 1989.
- [6] P. I. H. Bastiaens, I. V. Majoul, P. J. Verveer, H. Söling, and T. M. Jovin. Imaging the intracellular trafficking and state of the ab5 quaternary structure of cholera toxin. *The EMBO Journal*, 15(16):4246–4253, 1996.
- [7] W. Denk, J. H. Strickler, and W. W. Webb. Two-photon laser scanning fluorescence microscopy. *Science*, 248(4951):73–76, 1990.
- [8] W. Denk, D. W. Piston, and W. W. Webb. Two-photon molecular excitation in laser-scanning microscopy. In James B. Pawley, editor, *Handbook of Biological Confocal Microscopy*, chapter 28, pages 445–458. Plenum Press, 1995.
- [9] W. Denk. Two-photon excitation in functional biological imaging. *Journal of Biomedical Optics*, 1(3):296–304, 1996.
- [10] W. R. Zipfel, R. M. Williams, and W. W. Webb. Nonlinear magic: multiphoton microscopy in the biosciences. *Nature Biotechnology*, 21(11):1369–1377, 2003.
- [11] D. W. Brousmiche, J. M. Serin, J. M. J. Fréchet, G. S. He, T. Lin, S. J. Chung, and P. N. Prasad. Fluorescence resonance energy transfer in a novel two-photon

- absorbing system. *Journal of the American Chemical Society*, 125(6):1448–1449, 2003.
- [12] J. D. Mills, D. O. Okonkwo, A. Periasamy, G. A. Helm, J. R. Stone, D. G. Rubin, and D. E. Melon. Illuminating protein interactions in tissue using confocal and two-photon excitation fluorescent resonance energy transfer microscopy. *Journal of Biomedical Optics*, 8(3):347–356, 2003.
- [13] M. Elangovan, H. Wallrabe, Y. Chen, R. N. Day, M. Barroso, and A. Periasamy. Characterization of one-and two-photon excitation fluorescence resonance energy transfer microscopy. *Methods*, 29(1):58–73, 2003.
- [14] H. Wallrabe, M. Stanley, A. Periasamy, and M. Barroso. One-and two-photon fluorescence resonance energy transfer microscopy to establish a clustered distribution of receptor-ligand complexes in endocytic membranes. *Journal of Biomedical Optics*, 8(3):339–346, 2003.
- [15] T. Forster. Energiewanderung und fluoreszenz. *Naturwissenschaften*, 33(6):166–175, 1946.
- [16] T. Forster. Intermolecular energy migration and fluorescence. In Eugene V. Mielczarek, Elias Greenbaum, and Robert S. Knox, editors, *Biological Physics*, pages 148–160. American Institute of Physics, 1993.
- [17] P. R. Selvin. [13] fluorescence resonance energy transfer. *Methods in enzymology*, 246:300–334, 1995.
- [18] R. M. Clegg. Fluorescence resonance energy transfer. In Xue Feng Wang and Brian Herman, editors, *Fluorescence Imaging Spectroscopy and Microscopy*, volume 137 of *Chemical Analysis*, chapter 7, pages 179–252. John Wiley & Sons, 1996.
- [19] C. R. Cantor and P. R. Schimmel. *Biophysical Chemistry, Part II: Techniques for the study of biological structure and function*, volume 55, chapter 8, pages 448–454. W. H. Freeman and Company, 1980.
- [20] R. M. Clegg. Forster resonance energy transfer - fret what is it, why do it, and how it’s done. In TWJ Gadella, editor, *Laboratory Techniques in Biochemistry and Molecular Biology - FRET and FLIM Techniques*, volume 33, chapter 1, pages 1–57. Academic Press, 2009.
- [21] A. Hoppe, K. Christensen, and J. A. Swanson. Fluorescence resonance energy transfer-based stoichiometry in living cells. *Biophysical Journal*, 83(6):3652–3664, 2002.
- [22] M. H. Brenner, D. Cai, S. R. Nichols, S. W. Straight, A. D. Hoppe, J. A. Swanson, and J. P. Ogilvie. Pulse shaping multiphoton fret microscopy. In *SPIE BiOS*. International Society for Optics and Photonics, 2012.

- [23] M. H. Brenner, D. Cai, S. W. Straight, J. A. Swanson, and J. P. Ogilvie. Pulse-shaping-based two-photon fret microscopy. In *EPJ Web of Conferences*, volume 41, page 11009. EDP Sciences, 2013.
- [24] M. Drobizhev, N. S. Makarov, S. E. Tillo, T. E. Hughes, and A. Rebane. Two-photon absorption properties of fluorescent proteins. *Nature Methods*, 8(5):393–399, May 2011.
- [25] D. Entenberg, J. Wyckoff, B. Gligorijevic, E. T. Roussos, V. V. Verkhusha, J. W. Pollard, and J. Condeelis. Setup and use of a two-laser multiphoton microscope for multichannel intravital fluorescence imaging. *Nature Protocols*, 6(10):1500–1520, October 2011.
- [26] A. M. Weiner. Femtosecond pulse shaping using spatial light modulators. *Review of Scientific Instruments*, 71(5):1929–1960, 2000.
- [27] J. P. Ogilvie, D. Débarre, X. Solinas, J. Martin, E. Beaurepaire, and M. Joffre. Use of coherent control for selective two-photon fluorescence microscopy in live organisms. *Optics Express*, 14(2):759–766, 2006.
- [28] R. S. Pillai, C. Boudoux, G. Labroille, N. Olivier, I. Veilleux, E. Farge, M. Joffre, and E. Beaurepaire. Multiplexed two-photon microscopy of dynamic biological samples with shaped broadband pulses. *Optics Express*, 17(15):12741–12752, 2009.
- [29] E. R. Tkaczyk, A. H. Tkaczyk, K. Mauring, J. Y. Ye, J. R. Baker Jr, and T. B. Norris. Control of two-photon fluorescence of common dyes and conjugated dyes. *Journal of Fluorescence*, 19(3):517–532, 2009.
- [30] E. R. Tkaczyk, A. H. Tkaczyk, K. Mauring, J. Y. Ye, J. R. Baker Jr, and T. B. Norris. Quantitative differentiation of dyes with overlapping one-photon spectra by femtosecond pulse-shaping. *Journal of Luminescence*, 130(1):29–34, 2010.
- [31] I. Pastirk, J. M. Dela Cruz, K. A. Walowicz, V. V. Lozovoy, and M. Dantus. Selective two-photon microscopy with shaped femtosecond pulses. *Optics Express*, 11(14):1695–1701, 2003.
- [32] K. Isobe, A. Suda, M. Tanaka, F. Kannari, H. Kawano, H. Mizuno, A. Miyawaki, and K. Midorikawa. Multifarious control of two-photon excitation of multiple fluorophores achieved by phase modulation of ultra-broadband laser pulses. *Optics Express*, 17(16):13737–13746, 2009.
- [33] Y. Coello, V. V. Lozovoy, T. C. Gunaratne, B. Xu, I. Borukhovich, C. Tseng, T. Weinacht, and M. Dantus. Interference without an interferometer: a different approach to measuring, compressing, and shaping ultrashort laser pulses. *JOSA B*, 25(6):A140–A150, 2008.

- [34] V. V. Lozovoy, I. Pastirk, and M. Dantus. Multiphoton intrapulse interference. iv. ultrashort laser pulse spectral phase characterization and compensation. *Optics Letters*, 29(7):775–777, 2004.
- [35] B. Xu, J. M. Gunn, J. M. Dela Cruz, V. V. Lozovoy, and M. Dantus. Quantitative investigation of the multiphoton intrapulse interference phase scan method for simultaneous phase measurement and compensation of femtosecond laser pulses. *JOSA B*, 23(4):750–759, 2006.
- [36] C. Thaler, S. V. Koushik, P. S. Blank, and S. S. Vogel. Quantitative multiphoton spectral imaging and its use for measuring resonance energy transfer. *Biophysical Journal*, 89(4):2736–2749, 2005.
- [37] Y. Chen and A. Periasamy. Characterization of two-photon excitation fluorescence lifetime imaging microscopy for protein localization. *Microscopy research and technique*, 63(1):72–80, 2004.
- [38] M. Comstock, V. Lozovoy, I. Pastirk, and M. Dantus. Multiphoton intrapulse interference 6; binary phase shaping. *Optics Express*, 12(6):1061–1066, 2004.

CHAPTER V

Fluorescence Resonance Energy Transfer Stoichiometry

5.1 Introduction

As discussed in the previous chapter, Fluorescence Resonance Energy Transfer (FRET) has become an important tool in biological imaging [1, 2]. Its strong distance dependence makes it possible to learn a great deal about the structure of and interactions in biological systems. Traditional FRET techniques do have limitations, though. In particular, while FRET results can provide useful qualitative data, they often do not give much in the way of quantitative information. Although the FRET efficiency and relative distances can be determined with some techniques, more useful details about the stoichiometry of the interaction are difficult to measure. With increasing use of FRET in the microscope, techniques were developed to quantify FRET results by correcting for detector crosstalk, one of the major complicating factors in FRET studies. Measurements of FRET efficiency are often based on acceptor fluorescence signal detected under donor excitation conditions. However, not all excited donor molecules will transfer their energy to the acceptor molecules, resulting in some donor fluorescence; if this overlaps spectrally with the acceptor fluorescence, it will be erroneously recorded as signal due to FRET. Likewise, it is possible that

the acceptor molecule could be directly excited by the wavelengths used to excite the donor. Fluorescence resulting from this direct excitation would also potentially be recorded as signal due to FRET.

The first step in quantifying FRET is correcting for these crosstalk problems, and several methods have been proposed to do this. Gordon *et al.* [3] developed FRET_N, a method which uses a series of images taken with different filter cubes to determine the magnitude of the crosstalk terms and then correct for them. This method also corrects for differences in donor and acceptor concentration. FRET_N was used to investigate the behavior of Bcl-2, an anti-apoptotic protein, and Beclin, a protein that potentially acts as a tumor suppressor [3]. Xia and Liu [4] developed a similar method, N_{FRET} , which incorporates fluorescent proteins and accounts for differences in protein expression in different cells. These methods rely on the ability to selectively excite the donor and acceptor fluorophores in order to determine the magnitude of these crosstalk factors; an additional study by Erickson *et al.* [5] attempted to quantify FRET when selective excitation of each individual fluorophore was not possible.

The above examples were performed under one-photon imaging conditions, but work has been done in two-photon FRET imaging as well. Wallrabe *et al.* [6] developed a pixel-based FRET correction algorithm, PFRET, and compared its use in both one- and two-photon excited FRET imaging. Like the methods discussed above, PFRET explicitly corrects for crosstalk between detection channels; PFRET takes the additional step of comparing pixels of similar intensities to yield pixel-specific results. The method was easily extended to two-photon excited FRET and found “comparable” FRET efficiency values between the two excitation conditions [6]. Transitioning to two-photon excitation provides several significant benefits for biological imaging over one-photon microscopy as discussed in Chapter I, including reduced photodamage and photobleaching, increased penetration depth in tissues, and intrinsic sectioning ability [7–9].

An additional technique used to quantify FRET is Fluorescence Lifetime Imaging Microscopy (FLIM). This method takes advantage of the decrease in donor fluorescence lifetime that accompanies FRET [2]. When the donor and acceptor are in close proximity, energy transfer can occur quickly compared to the rate of other relaxation pathways, so most of the energy is transferred to the acceptor. This works to decrease the donor fluorescence lifetime as FRET efficiency increases [2]. FLIM-FRET measures the donor fluorophore lifetime in conditions when FRET does and does not occur and compares them to estimate the FRET efficiency. This method can be used for both one- and two-photon excited FRET, as it has been demonstrated that the fluorescence lifetimes are generally similar for both excitation methods [10]. Early FLIM-FRET studies investigated intranuclear dimer formation [11, 12] as well as amyloid-beta plaques [13]. FLIM-FRET suffers from the disadvantage of requiring an expensive and complicated time-correlated photon-counting setup. In addition, it has relatively long image acquisition times, often on the order of minutes.

While the methods described above have attempted to quantify FRET in the microscope, the results have been limited. Often, the results are measured in arbitrary units, facilitating comparisons between conditions within a given experiment but not necessarily valid outside of those parameters. They are also generally limited to values for the FRET efficiency and by extension the separation between the interacting molecules. However, when studying a biological interaction, these results are only moderately useful. Stoichiometric information, such as ratios of donor- and acceptor-labeled molecules present, would provide more detail about the interaction. Hoppe *et al.* developed FRET stoichiometry, an imaged-based method to determine just this type of stoichiometric data about a FRET interaction [14]. Specifically, FRET stoichiometry reveals the fractions of donor and acceptor in complex in the sample as well as the molar ratio of acceptor to donor. This method was used to examine the behavior of small G proteins during phagocytosis in macrophages [15].

FRET stoichiometry has not previously been implemented in two-photon microscopy. As a result, the previously mentioned benefits of two-photon imaging have not been realized for these types of stoichiometric measurements. This chapter details efforts to extend FRET stoichiometry to two-photon microscopy with the use of ultrafast pulse shaping methods. Pulse shaping allows for selective excitation of both the donor and acceptor fluorophores, something that has been difficult to achieve in earlier implementations of multicolor two-photon fluorescence microscopy. The use of ultrabroadband titanium:sapphire (ti:sapph) oscillators permits multicolor imaging but excites the distinct fluorophores simultaneously; this prohibits the selective excitation that is needed to determine the extent of the crosstalk between channels. Another potential solution is the use of tunable titanium:sapphire oscillators, but the relatively long tuning time of these lasers (on the scale of minutes) hurts the temporal resolution of studies of dynamic biological processes. Ultrafast pulse shaping provides fast selective excitation of a range of fluorophores, making it an ideal tool for application of FRET stoichiometry to two-photon microscopy. This chapter begins by reviewing the theory of one-photon FRET stoichiometry. The required modifications for a two-photon version of FRET stoichiometry are then introduced and a new, fully general version of the theory is derived. Finally, current experimental results are discussed and potential avenues for future work are outlined.

5.2 Theory of One-Photon FRET Stoichiometry

FRET stoichiometry is an image-based technique that makes straightforward extensions to existing FRET theory. It relies on a set of 3 images taken under different excitation and emission (detection) conditions:

1. I_A : Acceptor excitation conditions and acceptor emission conditions
2. I_D : Detector excitation conditions and detector emission conditions

3. I_F : Detector excitation conditions and acceptor emission conditions

In other words, I_A and I_D are images taken under conditions ideal for the acceptor and donor alone, while I_F is the image taken under conditions ideal for detection of FRET. These three images are recorded for each of a series of samples which are cells expressing different combinations of fluorophores: donor only, acceptor only, donor and acceptor in complex (such that FRET can occur), and the experimental samples of unknown combinations of donor and acceptor. A sample expressing both donor and acceptor, but not in complex, can also be used as a non-FRET control. To calculate the full stoichiometry it is important to also know the characteristic FRET efficiency, E , of the linked donor-acceptor complex; however, a modified stoichiometry can be determined without knowledge of this parameter. While I_A , I_D , and I_F are physically images, in the rest of this derivation these terms refer to the pixel intensity values of the images, as all calculations are performed on a pixel-by-pixel basis. That is, when I_A appears in an equation below, the mathematical value to use is the intensity recorded at a specific pixel of the I_A image. The equation is then solved for each pixel in the image.

The equations for FRET stoichiometry are derived from existing equations for FRET efficiency. FRET can be detected in two different ways - the decrease in fluorescence signal from the donor and the increase in fluorescence signal from the acceptor. Each of these methods leads to an equation for the FRET efficiency that depends on the emitted fluorescence and the fraction of donor or acceptor in complex - key pieces of the stoichiometry to be determined. For the measurements based on the decrease in donor fluorescence observed [14, 16], the FRET efficiency E is given by

$$E = \left[1 - \frac{F_{DA}(\lambda_D^{ex} \lambda_D^{em})}{F_D(\lambda_D^{ex} \lambda_D^{em})} \right] \left(\frac{1}{f_D} \right) \quad (5.1)$$

Here, the notation indicates what sample the fluorescence is being recorded from in the F and its subscripts, and the lambda terms in parentheses indicate the specific combination of excitation and emission wavelengths being used. That is, the terms are of the form $F_X(\lambda_{\#}^{\dagger}\lambda_{\#}^{\ddagger})$. F_X denotes which fluorophore the signal originates from, \dagger indicates the excitation or emission condition, and $\#$ indicates the acceptor or donor wavelength. For example, $F_D(\lambda_D^{ex}\lambda_D^{em})$ is the donor fluorescence observed at the donor's excitation and emission wavelengths; this combination of excitation and emission wavelengths is analogous to the I_D image described above. Similarly $F_{DA}(\lambda_D^{ex}\lambda_D^{em})$ is the donor fluorescence recorded under the same conditions but in the presence of the acceptor fluorophore. f_D denotes the fraction of donor molecules in complex with the acceptor; this is the population of donor molecules that could transfer energy in FRET. For measurements of FRET efficiency based on the increase of acceptor fluorescence [14, 16],

$$E = \left(\frac{\varepsilon_A(\lambda_D^{ex})}{\varepsilon_D(\lambda_D^{ex})} \right) \left[\frac{F_{AD}(\lambda_D^{ex}\lambda_A^{em})}{F_A(\lambda_D^{ex}\lambda_A^{em})} - 1 \right] \left(\frac{1}{f_A} \right) \quad (5.2)$$

This follows the same notation described above. $F_{AD}(\lambda_D^{ex}\lambda_A^{em})$ denotes the fluorescence recorded from the acceptor in the presence of the donor under the FRET imaging condition (that is, excite with the donor's wavelength and record at the acceptor's emission wavelength). $F_A(\lambda_D^{ex}\lambda_A^{em})$ is the fluorescence from the acceptor without the donor present under the same imaging conditions. Similarly to f_D , f_A is the fraction of acceptor in complex with the donor. This equation for FRET efficiency has an added term, $(\frac{\varepsilon_A(\lambda_D^{ex})}{\varepsilon_D(\lambda_D^{ex})})$, compared to (5.1). This term is the ratio of the extinction coefficient of the acceptor to that of the donor at the donor's excitation wavelength. It is important to note that this equation for the efficiency only holds when the donor does not emit at the acceptor's emission wavelength; however, this can happen experimentally and is one of the major potential problems in FRET. A correction for

this will be introduced later in the theory.

The FRET stoichiometry derivation begins by considering the case presented in (5.2). The challenge is to relate the fluorescence terms in that equation, namely $F_{AD}(\lambda_D^{ex}\lambda_A^{em})$ and $F_A(\lambda_D^{ex}\lambda_A^{em})$, to the three I_D , I_A , and I_F images described above that can be measured in the available samples. In particular, the contribution from the acceptor alone must be determined even when the donor is there as well, since in an unknown sample both fluorophores may be present. The potential donor emission signal at the acceptor emission wavelength must also be corrected. First, some assumptions are made about the ability of filters in the system to separate the donor and acceptor fluorescence. It is assumed that the contribution from the acceptor fluorophore when excited by the donor wavelength and detected in the donor channel is zero:

$$F_A(\lambda_D^{ex}\lambda_D^{em}) = 0 \quad (5.3)$$

Likewise, it is assumed that the contribution from the donor fluorophore when excited by the acceptor wavelength and detected in the acceptor channel is zero:

$$F_D(\lambda_A^{ex}\lambda_A^{em}) = 0 \quad (5.4)$$

Using this, and assuming that the fluorescence from the acceptor is not changed by the interaction with the donor (i.e. weak coupling) [14],

$$F_{AD}(\lambda_A^{ex}\lambda_A^{em}) = F_A(\lambda_A^{ex}\lambda_A^{em}) \quad (5.5)$$

This states that the fluorescence from the acceptor in the presence of the donor, under the ideal excitation and emission conditions for the acceptor, is the same as if the donor was absent. It is evident that this relies heavily on the assumption that the

donor does not contribute significant signal under the acceptor imaging conditions. With the use of a proportionality factor and as long as the emission from the acceptor at one excitation wavelength is proportional to the emission due to excitation at another wavelength, the fluorescence from the acceptor in the presence of the donor can be used to determine what the fluorescence would be in the absence of the donor [14]:

$$F_A(\lambda_D^{ex} \lambda_A^{em}) = \alpha F_{AD}(\lambda_A^{ex} \lambda_A^{em}) = \alpha I_A \quad (5.6)$$

where alpha is defined as

$$\alpha = \frac{F_A(\lambda_D^{ex} \lambda_A^{em})}{F_A(\lambda_A^{ex} \lambda_A^{em})} \quad (5.7)$$

and is measured in a sample containing the acceptor fluorophore only [14].

This has still not been corrected for spectral leakthrough of donor emission into the acceptor's detection channel. This leads to contamination in the I_F , or FRET, image:

$$F(\lambda_D^{ex} \lambda_A^{em}) = F_{AD}(\lambda_D^{ex} \lambda_A^{em}) + F_{DA}(\lambda_D^{ex} \lambda_A^{em}) = I_F \quad (5.8)$$

Fortunately, another proportionality factor can be used to determine the contribution of the donor fluorescence under these conditions.

$$F_{DA}(\lambda_D^{ex} \lambda_A^{em}) = \beta F_{DA}(\lambda_D^{ex} \lambda_D^{em}) = \beta I_D \quad (5.9)$$

Here, I_D is the image taken under donor imaging conditions and β is the proportionality constant found from samples containing donor fluorophores only [14]:

$$\beta = \frac{F_D(\lambda_D^{ex} \lambda_A^{em})}{F_D(\lambda_D^{ex} \lambda_D^{em})} \quad (5.10)$$

Now that the spectral leakthrough has been corrected and the contribution from the acceptor without the donor present has been determined even for conditions including the donor, these results can be substituted into (5.2) to find the final efficiency equation:

$$E = \left(\frac{\varepsilon_A(\lambda_D^{ex})}{\varepsilon_D(\lambda_D^{ex})} \right) \left[\frac{F(\lambda_D^{ex} \lambda_A^{em}) - \beta F_{DA}(\lambda_D^{ex} \lambda_D^{em})}{\alpha F_A(\lambda_A^{ex} \lambda_A^{em})} - 1 \right] \left(\frac{1}{f_A} \right) \quad (5.11)$$

This can be rewritten in terms of the three images acquired in the microscope to give:

$$E = \gamma \left[\frac{I_F - \beta I_D}{\alpha I_A} - 1 \right] \left(\frac{1}{f_A} \right) \quad (5.12)$$

where γ is used to represent the ratio of the extinction coefficients [14]. A simple rearrangement of terms leads to an equation for the fraction of acceptors in complex, one of the desired stoichiometric quantities [14]:

$$f_A = \frac{[C]}{[A_T]} = \gamma \left[\frac{I_F - \beta I_D}{\alpha I_A} - 1 \right] \left(\frac{1}{E} \right) \quad (5.13)$$

The first equality in this formula explicitly states how this fraction relates to the concentration of the molecules present, where $[C]$ is the concentration of the donor-acceptor complex and $[A_T]$ is the total concentration of free and complexed acceptor. This also assumes knowledge of the characteristic FRET efficiency of the interaction being studied, E . This can be measured by a number of techniques such as fluorescence lifetime imaging. However, if this is not known, the apparent efficiency of energy

transfer to the acceptor, denoted E_A , can still be found as $E_A = Ef_A$. While not the same as directly knowing the fraction of acceptors in complex, this result still reflects changes in that quantity [14].

The above portion of the derivation has looked at detection of FRET by observing the increase in acceptor fluorescence; this provided a way to determine the fraction of acceptor in complex. However, the fraction of donor in complex is another stoichiometric quantity of interest. This can be determined from (5.1), with its explicit dependence on that fraction; this means that $F_{DA}(\lambda_D^{ex}\lambda_D^{em})$ and $F_D(\lambda_D^{ex}\lambda_D^{em})$ must be determined in terms of the images that can be recorded. It is helpful to begin with (5.8) with the recognition that the term for fluorescence from the acceptor in the presence of the donor consists of two parts [14]:

$$F(\lambda_D^{ex}\lambda_A^{em}) = F_{AD}(\lambda_D^{ex}\lambda_A^{em}) + F_{DA}(\lambda_D^{ex}\lambda_A^{em}) \quad (5.14)$$

$$= F_A(\lambda_D^{ex}\lambda_A^{em}) + F_T(\lambda_D^{ex}\lambda_A^{em}) + F_{DA}(\lambda_D^{ex}\lambda_A^{em}) \quad (5.15)$$

This explicitly shows that the fluorescence from the acceptor in the presence of the donor under the FRET imaging conditions contains a component of fluorescence due to FRET (the F_T term) and a component of fluorescence due to accidental direct excitation of the acceptor (the F_A term). The FRET term can be rewritten in terms of the already-defined alpha and beta constants and other images:

$$F_T(\lambda_D^{ex}\lambda_A^{em}) = F(\lambda_D^{ex}\lambda_A^{em}) - \alpha F_{AD}(\lambda_D^{ex}\lambda_A^{em}) - \beta F_{DA}(\lambda_D^{ex}\lambda_D^{em}) \quad (5.16)$$

The $F_D(\lambda_D^{ex}\lambda_D^{em})$ term still has to be written in terms of images that can be recorded. This represents the total fluorescence emitted from the donor if the acceptor were not

present and can be thought of as

$$F_D(\lambda_D^{ex} \lambda_D^{em}) = F_T(\lambda_D^{ex} \lambda_A^{em}) \left(\frac{\xi}{\gamma} \right) + F_{DA}(\lambda_D^{ex} \lambda_D^{em}) \quad (5.17)$$

which is the fluorescence from energy transfer, corrected for differences in acceptor and donor detection channels and acceptor quantum yield by the ξ term, plus the fluorescence from the donor in the presence of the acceptor [14]. Substituting this into (5.1) yields

$$E = \left[1 - \frac{F_{DA}(\lambda_D^{ex} \lambda_D^{em})}{F_T(\lambda_D^{ex} \lambda_A^{em}) \left(\frac{\xi}{\gamma} \right) + F_{DA}(\lambda_D^{ex} \lambda_D^{em})} \right] \left(\frac{1}{f_D} \right) \quad (5.18)$$

By recognizing that the $F_{DA}(\lambda_D^{ex} \lambda_D^{em})$ is the same as the I_D image and the $F_T(\lambda_D^{ex} \lambda_A^{em})$ term is the I_F image, (5.18) can be rewritten in terms of images as

$$E = \left[1 - \frac{I_D}{(I_F - \alpha I_A - \beta I_D) \left(\frac{\xi}{\gamma} \right) + I + D} \right] \left(\frac{1}{f_D} \right) \quad (5.19)$$

A simple rearrangement of terms leads to the equation for the fraction of donor in complex [14]:

$$f_D = \frac{[C]}{[D_T]} = \left[1 - \frac{I_D}{(I_F - \alpha I_A - \beta I_D) \left(\frac{\xi}{\gamma} \right) + I + D} \right] \left(\frac{1}{E} \right) \quad (5.20)$$

Again, the first equality shows the explicit dependence of the concentrations of complex and total donor. As with the equation for the fraction of acceptor in complex, this assumes that the FRET efficiency E is already known. If not, an apparent efficiency for the donor can be found similarly to that for the acceptor [14]:

$$E_D = E f_D \quad (5.21)$$

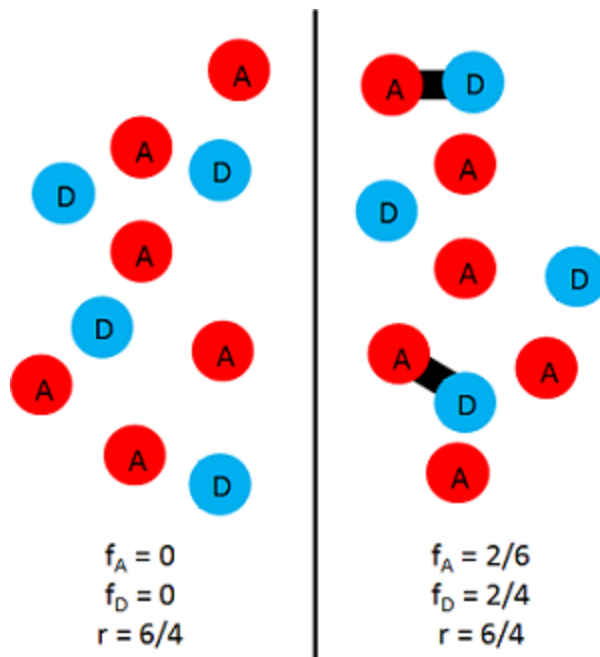


Figure 5.1: Example of FRET stoichiometry. The left side illustrates the f_A , f_D , and r values for a sample with no fluorophores in complex. The right side shows the same fluorophores, but now two complexes have formed. Note that the fractions change but the molar ratio does not. Image adapted from [17].

The final stoichiometric quantity desired is the molar ratio of acceptor to donor. It is straightforward to find this by combining the equations for the fractions of donor and acceptor in complex already found. By considering the actual concentrations, the molar ratio r is given by [14]

$$r = \frac{[A_T]}{[D_T]} = \left(\frac{\xi}{\gamma^2} \right) \frac{\alpha I_A}{(I_F - \alpha I_A - \beta I_D) \left(\frac{\xi}{\gamma} \right) + I_D} \quad (5.22)$$

Thus, FRET stoichiometry provides three key pieces of information that cannot normally be obtained from FRET experiments:

1. The fraction of donor in complex
2. The fraction of acceptor in complex
3. The molar ratio of acceptor to donor

Figure 5.1 illustrates this information in two different sample conditions [17]. The left side shows a sample with a mixture of acceptor and donor fluorophores but none in complex; the right side shows the same sample after two complexes have formed. The molar ratio is unchanged between the two situations, because no fluorophores have been added or removed, but the fractions in complex are different. Having this type of stoichiometric information makes it possible to gain a fuller understanding of a biological interaction.

Hoppe *et al.* demonstrated FRET stoichiometry in macrophages, and their results are shown in figure 5.2 [14]. This shows the FRET stoichiometry data from cells expressing combinations of Cyan Fluorescent Protein (CFP) as the donor fluorophore and Citrine as the acceptor fluorophore. Column A is the intensity images of cells expressing the FRET construct CFP-Citrine plus excess Citrine. The intensity variations in the cells are due to differences in protein expression or cell thickness. Column B shows the FRET stoichiometry results from the same cells, with the molar ratio R (r in the notation of this thesis) in the top image, the fraction of acceptor in complex in the middle image, and the fraction of donor in complex in the bottom image. In these cells, the donor is limited, as the cells are expressing the one-to-one complex with extra acceptor. As a result, the fraction of donor in complex is one; this is verified in the bottom image of Column B. The fraction of acceptor in complex is less than one, as expected. In addition, the molar ratio is inversely correlated with the fraction of acceptor in complex. As the amount of free acceptor present in the sample increases, the fraction of acceptor in complex decreases while the molar ratio of acceptor to donor increases. Column C shows a different set of cells expressing the CFP-Citrine complex with excess CFP; here, the fraction of acceptor in complex is one and the fraction of donor in complex is less than one. The molar ratio is correlated with the fraction of donor in complex - as the amount of donor is increased by adding more free donor, the fraction in complex goes down as does the molar ratio

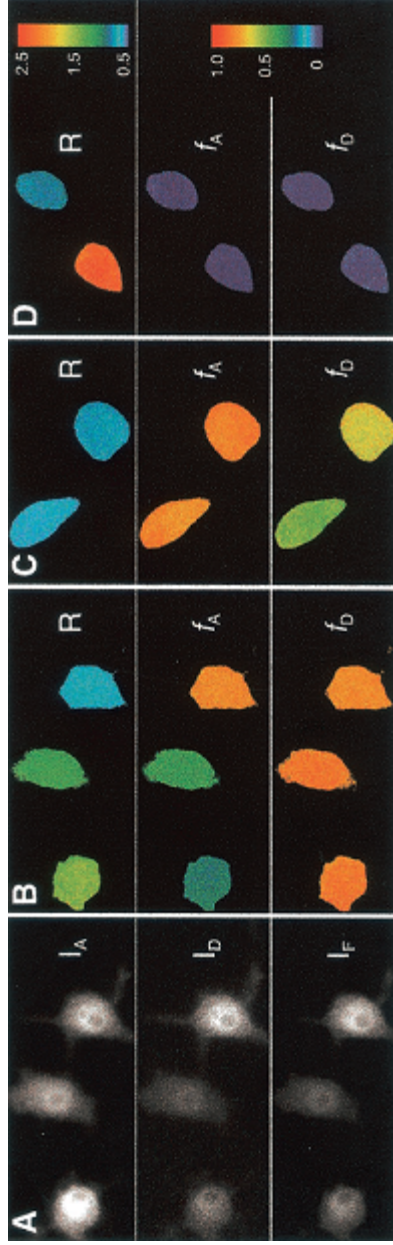


Figure 5.2: One-photon FRET stoichiometry data. The four columns in this graphic show the results of FRET stoichiometry in macrophages. Column A shows the intensity images I_A , I_D , and I_F of cells expressing a linked construct of CFP-Citrine, where FRET occurs between the donor CFP and acceptor Citrine, and excess free Citrine. The changes in brightness reflect changes in protein expression levels. Column B shows the FRET stoichiometry results from these same cells. The top image is the molar ratio (r in this work), the middle image is the fraction of acceptor in complex, and the bottom image is the fraction of donor in complex. As expected for a sample with excess acceptor, the fraction of donor in complex is one and the fraction of acceptor in complex is less than one. Column C shows cells expressing the CFP-Citrine complex with excess CFP (donor). Here, the fraction of acceptor in complex is one and the fraction of donor in complex is less than one. Column D shows cells expressing both donor and acceptor but not in complex; the fractions of donor and acceptor in complex are zero. Reprinted from [14], with permission from Elsevier.

of acceptor to donor. Finally, Column D shows cells expressing free CFP and free Citrine such that no FRET will occur between them. In this situation, the fractions are both zero, since no complex is present. Over the course of an interaction, this type of information can give a much clearer picture of the process than traditional FRET measurements.

5.3 Theory of Two-Photon FRET Stoichiometry

The above derivation for FRET stoichiometry was based on one-photon imaging conditions. As a result, it does not translate directly to the two-photon imaging case, and a modified theory is required. In particular, the assumptions of equations (5.3) and (5.4) do not necessarily hold. These statements assert that the donor fluorescence is negligible when excited at the acceptor's wavelength and detected in the acceptor channel, and similarly that the acceptor fluorescence is negligible when excited at the donor's wavelength and detected in the donor channel. There are two key reasons why these statements may not always hold in two-photon imaging. First, two-photon FRET imaging often removes bandpass filters from the detection channels, relying solely on dichroics to separate the fluorescence appropriately. This is because two-photon imaging is frequently used to image deep in tissues, which can significantly scatter the fluorescence signal before it is detected. Removing bandpass filters helps improve overall signal levels. In addition, removing bandpass filters has an added benefit when performing FRET stoichiometry calculations. This increases the crosstalk between detection channels, leading to more accurate determinations of the crosstalk constants and potentially more accurate stoichiometric measurements.

The second factor making the assumptions of (5.3) and (5.4) potentially fail in two-photon imaging is the potential overlap between the excitation spectra of the donor and acceptor fluorophores. This depends in part on the actual FRET pair used. Some level of overlap is generally present due to the requirement that the

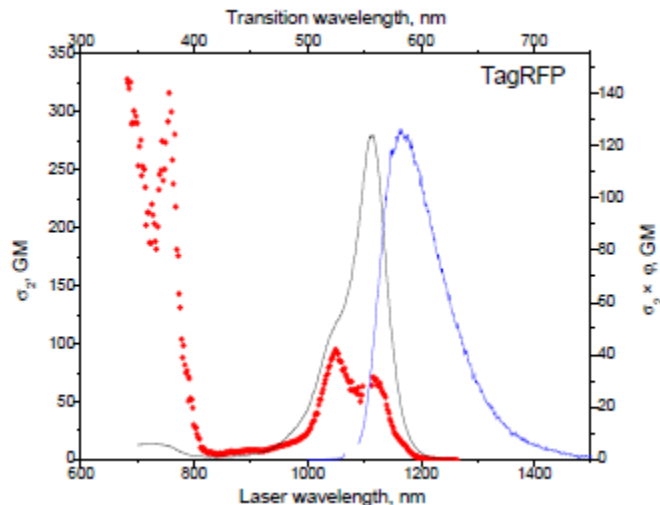


Figure 5.3: Two-photon cross-section of TagRFP. The two-photon absorption spectrum is shown in red, the one-photon absorption spectrum in black, and the fluorescence emission spectrum in blue. Taken from [19]. Note the sharp rise in two-photon absorption at wavelengths below 800 nm; this is not expected based on the one-photon absorption spectrum.

donor's emission spectrum overlaps with the acceptor's excitation spectrum for FRET to occur. However, the specific pair used may have more or less overlap between the excitation spectra and thus cannot always be assumed to be negligible. An additional factor important in two-photon imaging is the increasing use of transitions to higher excited states in certain red fluorescent proteins [18, 19]. These transitions have significant two-photon cross-sections at shorter wavelengths than would be expected by doubling the peak wavelengths for one-photon absorption. Figure 5.3 shows an example of this behavior in the red fluorescent protein TagRFP [19]. This increases the overlap of the donor and acceptor excitation spectra, in turn increasing the chances of accidental direct excitation of either fluorophore.

Given this flexibility in which assumptions may or may not hold for two-photon excited FRET stoichiometry, this section presents a new theory for the most general case. This derivation does not make any assumptions about certain fluorescence contributions being negligible and instead follows all possible contributions through the entire theory, leading to new equations for the fractions of donor and acceptor in

complex and the molar ratio of acceptor to donor. It follows the same structure as the one-photon case and utilizes the same equations for FRET efficiency. To begin, a random sample containing both donor and acceptor fluorophores is considered. Some, but not all, of these fluorophores will be in complex such that FRET can occur between them. The fluorescence signal from this sample will have three components:

1. F_D : Fluorescence from donor
2. F_A : Fluorescence from acceptor
3. F_C : Fluorescence from the donor-acceptor complex

The F_C term itself can be broken into three parts, following the equation $F_C = F_T + F_{DC} + F_{AC}$. These parts are:

1. F_{DC} = Fluorescence from the complexed donor
2. F_{AC} = Fluorescence from the complexed acceptor
3. F_T = Fluorescence from energy transfer

The F_{DC} term is non-zero because the FRET efficiency is not 100% - some donor molecules will be excited which will emit donor fluorescence rather than transferring that energy to the acceptor. Similarly, the F_{AC} term is non-zero because it can be directly excited by incident light even at the donor's excitation wavelength; thus, it is not solely dependent on energy transfer to fluoresce. However, it is important to note that the fluorescence from the complexed donor cannot be distinguished from the fluorescence from the free donor. Likewise, the fluorescence from the complexed acceptor cannot be distinguished from the fluorescence from the free acceptor. Consequently, the F_D and F_A terms already contain the signal from the complexed fluorophores and no additional terms beyond these two are required.

In this general sample situation, then, there are three signal components to consider:

1. F_D = all fluorescence from donor fluorophores
2. F_A = all fluorescence from acceptor fluorophores that is NOT due to FRET
3. F_T = all fluorescence due to energy transfer

The notation moving forward in this derivation is the same as that used in the one-photon case; namely, terms are of the form $F_X(\lambda_{\#}^{\dagger}, \lambda_{\#}^{\dagger})$. F_X denotes which fluorophore the signal originates from, \dagger indicates the excitation or emission condition, and $\#$ indicates the acceptor or donor wavelength. As an example, $F_D(\lambda_A^{ex}, \lambda_D^{em})$ denotes fluorescence signal from the donor when excited at the acceptor's wavelength and detected in the donor's emission channel.

For a theory that is applicable in the microscope, this derivation must be in terms of images that can be recorded. There are three images to consider:

1. $I_F = F(\lambda_D^{ex}, \lambda_A^{em}) = F_D(\lambda_D^{ex}, \lambda_A^{em}) + F_A(\lambda_D^{ex}, \lambda_A^{em}) + F_T(\lambda_D^{ex}, \lambda_A^{em})$
2. $I_A = F(\lambda_A^{ex}, \lambda_A^{em}) = F_D(\lambda_A^{ex}, \lambda_A^{em}) + F_A(\lambda_A^{ex}, \lambda_A^{em}) + F_T(\lambda_A^{ex}, \lambda_A^{em})$
3. $I_D = F(\lambda_D^{ex}, \lambda_D^{em}) = F_D(\lambda_D^{ex}, \lambda_D^{em}) + F_A(\lambda_D^{ex}, \lambda_D^{em}) + F_T(\lambda_D^{ex}, \lambda_D^{em})$

Thus, the I_F image looks at the FRET imaging condition, and the I_A and I_D images look at the imaging conditions ideal for the acceptor and donor fluorophores, respectively. Depending on the experimental conditions actually being used, it is possible that some of these terms will be negligible and can be set to zero. However, as discussed above, this derivation retains all terms to find the stoichiometric equations for the most general case. It is important to note that rejecting the assumptions of (5.3) and (5.4) has a broader effect than just keeping the $F_D(\lambda_A^{ex}, \lambda_A^{em})$ and $F_A(\lambda_D^{ex}, \lambda_D^{em})$ terms. In particular, $F_T(\lambda_A^{ex}, \lambda_A^{em})$ cannot be assumed to be zero because the donor fluorophore can be directly excited by the acceptor's excitation condition, which could lead to FRET. Similarly, $F_T(\lambda_D^{ex}, \lambda_D^{em})$ is not necessarily zero because fluorescence from the acceptor may leak into the donor emission channel.

The one-photon FRET stoichiometry derivation begins by finding an equation for f_A , the fraction of acceptor in complex, by considering the equation for FRET efficiency calculated from the increase in acceptor fluorescence given in (5.2). The theory presented here for the two-photon case will also use this equation as a starting point. The ratio of the extinction coefficients, given by the parameter γ , applies in the one-photon case. It is expected that in the two-photon case, this is replaced by the ratio of the two-photon absorption cross-sections. This factor normalizes the energy absorbed by the acceptor to that absorbed by the donor at the donor's excitation wavelength; at this wavelength both the donor and acceptor individually are excited via two-photon absorption, so the cross-section values should be valid to determine how the direct excitation of the acceptor compares to that of the donor. The factor is called γ_{TPE} in this derivation and is found using the same method as in the one-photon case.

Moving forward with this equation for the FRET efficiency, it is necessary to determine $F_{AD}(\lambda_D^{ex}\lambda_A^{em})$ and $F_A(\lambda_D^{ex}\lambda_A^{em})$ from images taken in the microscope. Those values can then be substituted into the equation for the efficiency. As in the one-photon derivation, the potential leakthrough of the donor fluorescence into the acceptor detection channel will be corrected. This begins by recognizing that $F_{AD}(\lambda_D^{ex}\lambda_A^{em})$, the fluorescence from the acceptor in the presence of the donor, can be written as

$$F_{AD}(\lambda_D^{ex}\lambda_A^{em}) = F_A(\lambda_D^{ex}\lambda_A^{em}) + F_T(\lambda_D^{ex}\lambda_A^{em}) \quad (5.23)$$

However, this definition does not account for donor fluorescence that could be present in the acceptor emission channel. Taking this into account, F_{AD} can be rewritten as

$$F_{AD}(\lambda_D^{ex}\lambda_A^{em}) = I_F - F_D(\lambda_D^{ex}\lambda_A^{em}) \quad (5.24)$$

based on the earlier definition of the image I_F . In order to substitute this into the

equation for the efficiency, $F_D(\lambda_D^{ex}\lambda_A^{em})$ has to be determined in terms of recorded images. Using the definition of the beta constant from the one-photon derivation given in (5.10),

$$F_D(\lambda_D^{ex}\lambda_A^{em}) = \beta F_D(\lambda_D^{ex}\lambda_D^{em}) \quad (5.25)$$

Using the earlier definition of the I_D image,

$$F_D(\lambda_D^{ex}\lambda_D^{em}) = I_D - F_A(\lambda_D^{ex}\lambda_D^{em}) - F_T(\lambda_D^{ex}\lambda_D^{em}) \quad (5.26)$$

At this point, a substitution is needed for the F_A and F_T terms. A new crosstalk constant η is defined as

$$\eta = \frac{F_A(\lambda_D^{ex}\lambda_A^{em})}{F_A(\lambda_D^{ex}\lambda_D^{em})} = \frac{F_A(\lambda_A^{ex}\lambda_A^{em})}{F_A(\lambda_A^{ex}\lambda_D^{em})} \quad (5.27)$$

This equality holds because η determines how the acceptor fluorescence is split between channels, regardless of how the fluorescence is excited. Assuming that the acceptor fluorophore emits at the same wavelengths regardless of whether it is directly excited or excited via FRET, η can also be used to determine how the F_T signal splits between detection channels:

$$\eta = \frac{F_T(\lambda_D^{ex}\lambda_A^{em})}{F_T(\lambda_D^{ex}\lambda_D^{em})} = \frac{F_T(\lambda_A^{ex}\lambda_A^{em})}{F_T(\lambda_A^{ex}\lambda_D^{em})} \quad (5.28)$$

Using this η constant to substitute back into equation (5.26) for $F_D(\lambda_D^{ex}\lambda_D^{em})$ gives

$$F_D(\lambda_D^{ex}\lambda_D^{em}) = I_D - \frac{1}{\eta}(F_A(\lambda_D^{ex}\lambda_A^{em}) - F_T(\lambda_D^{ex}\lambda_A^{em})) \quad (5.29)$$

Using this in the equation for $F_{AD}(\lambda_D^{ex}\lambda_A^{em})$ yields

$$F_{AD}(\lambda_D^{ex}\lambda_A^{em}) = I_F - \beta[I_D - \frac{1}{\eta}(F_A(\lambda_D^{ex}\lambda_A^{em}) - F_T(\lambda_D^{ex}\lambda_A^{em}))] \quad (5.30)$$

However, $F_{AD}(\lambda_D^{ex}\lambda_A^{em})$ was also previously defined in (5.23). Using this definition leads to a final formula for $F_{AD}(\lambda_D^{ex}\lambda_A^{em})$:

$$F_{AD}(\lambda_D^{ex}\lambda_A^{em}) = \frac{I_F - \beta I_D}{1 - \frac{\beta}{\eta}} \quad (5.31)$$

As $F_A(\lambda_D^{ex}\lambda_D^{em})$ and $F_T(\lambda_D^{ex}\lambda_D^{em})$ approach zero, as in the original one-photon derivation, η goes to infinity. In this limit, (5.31) goes to $I_F - \beta I_D$, matching its form in the original one-photon derivation.

To complete the equation for the FRET efficiency, the $F_A(\lambda_D^{ex}\lambda_A^{em})$ term still needs to be determined. While this is the fluorescence from the acceptor alone, this derivation is considering a general sample that contains donor fluorophores as well, so that needs to be taken into account. To do this, another new crosstalk constant, θ , is created:

$$\theta = \frac{F_D(\lambda_D^{ex}\lambda_D^{em})}{F_D(\lambda_A^{ex}\lambda_D^{em})} \quad (5.32)$$

so that

$$\theta F_D(\lambda_A^{ex}\lambda_D^{em}) = F_D(\lambda_D^{ex}\lambda_D^{em}) \quad (5.33)$$

Because θ looks solely at differences in excitation, it should hold for the acceptor's emission channel as well.

Using the initial definition of I_A given at the beginning of the derivation, this

definition of θ , and the β constant, an equation for $F_A(\lambda_A^{ex}\lambda_A^{em})$ can be found:

$$F_A(\lambda_A^{ex}\lambda_A^{em}) = I_A - \frac{1}{\theta}F_D(\lambda_D^{ex}\lambda_A^{em}) - F_T(\lambda_A^{ex}\lambda_A^{em}) \quad (5.34)$$

$$= I_A - \frac{\beta}{\theta}F_D(\lambda_D^{ex}\lambda_D^{em}) - F_T(\lambda_A^{ex}\lambda_A^{em}) \quad (5.35)$$

Further substitutions in this equation can be made by rewriting the $F_D(\lambda_D^{ex}\lambda_D^{em})$ term as a reorganization of the formula for the I_D image, using the η constant, and using the previously found form of $F_{AD}(\lambda_D^{ex}\lambda_A^{em})$:

$$F_A(\lambda_A^{ex}\lambda_A^{em}) = I_A - \frac{\beta}{\theta}[I_D - \frac{1}{\eta}F_{AD}(\lambda_D^{ex}\lambda_A^{em})] - F_T(\lambda_A^{ex}\lambda_A^{em}) \quad (5.36)$$

It is still necessary to determine the $F_T(\lambda_A^{ex}\lambda_A^{em})$ term. With the assumption that FRET efficiency is constant regardless of the excitation wavelength used to excite the donor, θ can be used to relate the F_T signal under both excitation conditions. Consequently,

$$F_T(\lambda_A^{ex}\lambda_A^{em}) = \frac{1}{\theta}F_T(\lambda_D^{ex}\lambda_A^{em}) = \frac{1}{\theta}[F_{AD}(\lambda_D^{ex}\lambda_A^{em}) - F_A(\lambda_D^{ex}\lambda_A^{em})] \quad (5.37)$$

Now, a number of substitutions and algebraic simplifications can be performed to finally arrive at an expression for $F_A(\lambda_D^{ex}\lambda_A^{em})$. Namely, (5.37) can be substituted into (5.36); the already-defined alpha crosstalk constant from the one-photon derivation can be applied; and (5.31) can be used to simplify the final expression. This gives a final result of

$$F_A(\lambda_D^{ex}\lambda_A^{em}) = \frac{\theta\alpha}{\theta - \alpha}I_A - \frac{\alpha}{\theta - \alpha}I_F \quad (5.38)$$

In the limit where the assumptions of (5.3) and (5.4) are kept, θ approaches infinity. Under these conditions, (5.38) goes to αI_A as in the original one-photon derivation.

Now, the two terms needed for the equation for FRET efficiency measured by the increase in acceptor fluorescence are finally known in terms of images that can be recorded in the microscope. Substituting (5.31) for $F_{AD}(\lambda_D^{ex}\lambda_A^{em})$ and (5.38) for $F_A(\lambda_D^{ex}\lambda_A^{em})$ into (5.2) gives

$$E = \gamma_{TPE} \left[\frac{\frac{\eta}{\eta-\beta} I_F - \frac{\beta\eta}{\eta-\beta} I_D}{\frac{\theta\alpha}{\theta-\alpha} I_A - \frac{\alpha}{\theta-\alpha} I_F} - 1 \right] \left(\frac{1}{f_A} \right) \quad (5.39)$$

This equation can be used to determine the gamma factor by setting $f_A = 1$ (such as in a sample containing only complexed fluorophores) and rearranging:

$$\gamma_{TPE} = E \left[\frac{\frac{\eta}{\eta-\beta} I_F - \frac{\beta\eta}{\eta-\beta} I_D}{\frac{\theta\alpha}{\theta-\alpha} I_A - \frac{\alpha}{\theta-\alpha} I_F} - 1 \right]^{-1} \quad (5.40)$$

Similarly, this can be rearranged to find the first of the key stoichiometric quantities f_A , the fraction of acceptor in complex:

$$f_A = \gamma_{TPE} \left[\frac{\frac{\eta}{\eta-\beta} I_F - \frac{\beta\eta}{\eta-\beta} I_D}{\frac{\theta\alpha}{\theta-\alpha} I_A - \frac{\alpha}{\theta-\alpha} I_F} - 1 \right] \left(\frac{1}{E} \right) \quad (5.41)$$

In the limit of $\eta, \theta \rightarrow 0$ to match the conditions of the original derivation, these equations for E , γ_{TPE} , and f_A simplify to their original forms.

At this point in the derivation, it is useful to introduce the sensitized emission. This is the increase in acceptor fluorescence due to energy transfer, and it can be calculated from microscope images. Experimentally, determination of the sensitized emission can serve as a confirmation that FRET is occurring. The sensitized emission term is $F_T(\lambda_D^{ex}\lambda_A^{em})$ and it can be found using the relation for the I_F image:

$$F_T(\lambda_D^{ex}\lambda_A^{em}) = I_F - F_D(\lambda_D^{ex}\lambda_A^{em}) - F_A(\lambda_D^{ex}\lambda_A^{em}) \quad (5.42)$$

The F_D term here can be found by combining the definition of the β constant with

the definitions of $F_D(\lambda_D^{ex} \lambda_D^{em})$ found in (5.29) and $F_{AD}(\lambda_D^{ex} \lambda_A^{em})$ found in (5.31) to give:

$$F_D(\lambda_D^{ex} \lambda_A^{em}) = \frac{\beta}{\eta - \beta} (\eta I_D - I_F) \quad (5.43)$$

The F_A term in (5.42) was found previously in (5.38). Substitution of these results and simplification leads to the following equation for the sensitized emission:

$$F_T(\lambda_D^{ex} \lambda_A^{em}) = \left(\frac{\eta\theta - \beta\alpha}{(\theta - \alpha)(\eta - \beta)} \right) I_F - \left(\frac{\beta\eta}{\eta - \beta} \right) I_D - \left(\frac{\alpha\theta}{\theta - \alpha} \right) I_A \quad (5.44)$$

Up to this point, the derivation has found the fraction of acceptor in complex using the equation for FRET efficiency based on the increase in acceptor fluorescence, as well as the sensitized emission. This leaves two stoichiometric quantities of interest to be determined, the fraction of donor in complex and the molar ratio of acceptor to donor. The derivation of the one-photon FRET stoichiometry theory used the equation for FRET efficiency based on the decrease in donor fluorescence to determine the fraction of donor in complex, and that process will be repeated here. This equation is given in (5.1). It depends on the fluorescence from the donor in the presence of the acceptor (in the numerator) as well as the fluorescence from the donor as if the acceptor were absent (in the denominator), so these quantities must be determined in terms of images from the microscope. The fluorescence from the donor in the presence of the acceptor is found from the expression for the I_D image:

$$F_D(\lambda_D^{ex} \lambda_D^{em}) = I_D - F_A(\lambda_D^{ex} \lambda_D^{em}) - F_T(\lambda_D^{ex} \lambda_D^{em}) \quad (5.45)$$

The original derivation defined the fluorescence from the donor alone, as if the accep-

tor were not there, as

$$F_{DO}(\lambda_D^{ex}\lambda_D^{em}) = F_T(\lambda_D^{ex}\lambda_A^{em}) \left(\frac{\xi}{\gamma_{TPE}} \right) + F_{DA}(\lambda_D^{ex}\lambda_D^{em}) \quad (5.46)$$

That is, the fluorescence from the donor alone can be thought of as the fluorescence from the donor with the acceptor present plus some portion of the FRET signal. Here, the constant ξ has the same meaning and definition as in the original derivation, where it accounts for factors such as quantum yield and detector sensitivity to relate the amount of sensitized emission detected to the amount of donor fluorescence lost.

To continue, the quantities in (5.45) have to be replaced with images. This can be done using the η constant and the definition of $F_{AD}(\lambda_D^{ex}\lambda_A^{em})$ from (5.31). These substitutions give the fluorescence from the donor in the presence of the acceptor as

$$F_{DA}(\lambda_D^{ex}\lambda_D^{em}) = \left(\frac{1}{\eta - \beta} \right) (\eta I_D - I_F) \quad (5.47)$$

As η approaches zero, this reduces to I_D , as in the one-photon equation. To complete the efficiency equation, the $F_T(\lambda_D^{ex}\lambda_A^{em})$ term is needed for the formula for the fluorescence from the donor without the acceptor present. This was found as the sensitized emission in (5.44). Placing all of these new terms in the equation for the FRET efficiency determined by the decrease in donor fluorescence gives the final result:

$$E = \left[1 - \frac{\left(\frac{1}{\eta - \beta} \right) (\eta I_D - I_F)}{\left(\frac{\xi}{\gamma_{TPE}} \right) \left(\left(\frac{\eta\theta - \beta\alpha}{(\theta - \alpha)(\eta - \beta)} \right) I_F - \left(\frac{\beta\eta}{\eta - \beta} \right) I_D - \left(\frac{\alpha\theta}{\theta - \alpha} \right) I_A \right) + \left(\frac{1}{\eta - \beta} \right) (\eta I_D - I_F)} \right] \left(\frac{1}{f_D} \right) \quad (5.48)$$

Setting f_D to one, as is the case in a sample containing all linked fluorophores, leads to an equation for the constant ξ :

$$\xi = \frac{\gamma_{TPE} E \left(\frac{1}{\eta - \beta} (\eta I_D - I_F) \right)}{(1 - E) \left(\left(\frac{\eta\theta - \beta\alpha}{(\theta - \alpha)(\eta - \beta)} \right) I_F - \left(\frac{\beta\eta}{\eta - \beta} \right) I_D - \left(\frac{\alpha\theta}{\theta - \alpha} \right) I_A \right)} \quad (5.49)$$

By rearranging (5.48) an equation for the fraction of donor in complex can be found:

$$f_D = \left[1 - \frac{(\frac{1}{\eta-\beta})(\eta I_D - I_F)}{(\frac{\xi}{\gamma_{TPE}})((\frac{\eta\theta-\beta\alpha}{(\theta-\alpha)(\eta-\beta)})I_F - (\frac{\beta\eta}{\eta-\beta})I_D - (\frac{\alpha\theta}{\theta-\alpha})I_A) + (\frac{1}{\eta-\beta})(\eta I_D - I_F)} \right] \left(\frac{1}{E} \right) \quad (5.50)$$

Now that the fractions of donor and acceptor in complex are known, the last of the three stoichiometric quantities to be determined - the molar ratio of acceptor to donor, r - can be found. This is defined as f_D/f_A , just as in the one-photon derivation. Performing the division and some simplification yields a result for r :

$$r = \left(\frac{\xi}{\gamma_{TPE}^2} \right) \left[\frac{((\frac{\eta\theta-\beta\alpha}{(\theta-\alpha)(\eta-\beta)})I_F - (\frac{\beta\eta}{\eta-\beta})I_D - (\frac{\alpha\theta}{\theta-\alpha})I_A)(\frac{\theta\alpha}{\theta-\alpha}I_A - \frac{\alpha}{\theta-\alpha}I_F)}{(\frac{\xi}{\gamma_{TPE}})((\frac{\eta\theta-\beta\alpha}{(\theta-\alpha)(\eta-\beta)})I_F - (\frac{\beta\eta}{\eta-\beta})I_D - (\frac{\alpha\theta}{\theta-\alpha})I_A)} \right. \\ \left. \times ((\frac{\eta}{\eta-\beta}I_F - \frac{\beta\eta}{\eta-\beta}I_D) - (\frac{\theta\alpha}{\theta-\alpha}I_A - \frac{\alpha}{\theta-\alpha}I_F)) \right. \\ \left. + ((\frac{1}{\eta-\beta})(\eta I_D - I_F))((\frac{\eta}{\eta-\beta}I_F - \frac{\beta\eta}{\eta-\beta}I_D) - (\frac{\theta\alpha}{\theta-\alpha}I_A - \frac{\alpha}{\theta-\alpha}I_F)) \right] \quad (5.51)$$

This completes the derivation of FRET stoichiometry for the most general two-photon case.

5.4 Current Results

5.4.1 Experimental Methods

The experimental setup used to acquire images for FRET stoichiometry is similar to that described in Chapter III for linear unmixing experiments. A diagram of this setup is shown in figure 5.4. Pulses from a Femtolasers Synergy titanium:sapphire (ti:sapph) oscillator (75 MHz repetition rate, approximately 80 nm pulse bandwidth centered at approximately 790 nm) were used for shaping with a Biophotonic Solutions

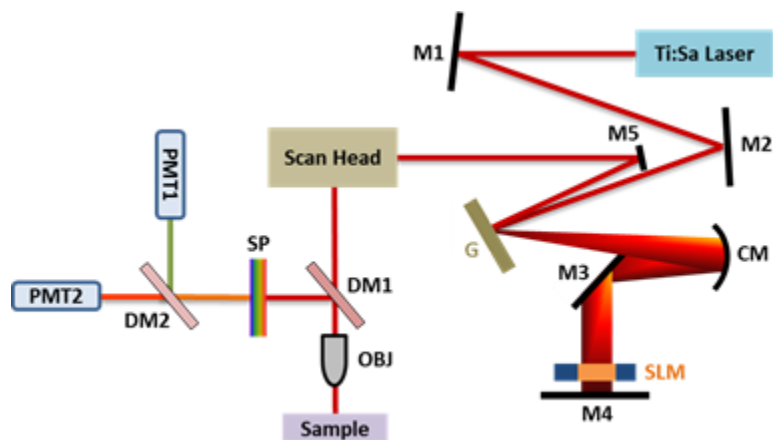


Figure 5.4: Experimental setup for FRET stoichiometry. M1-M5: mirrors, G = grating, CM = curved mirror, SLM = spatial light modulator, DM1 = 660DCXR dichroic mirror, DM2 = 550DCXR dichroic mirror, OBJ = 60x NA1.2 water immersion objective; SP = 650 nm short pass filter.

Inc. femtoJock pulse shaper. A single-mask 128-pixel spatial light modulator (SLM) in a reflective 4f setup is used in the femtoJock for phase shaping of the input pulses. A variable neutral density filter was used to control the laser power at the sample. The laser was aligned into an Olympus BX51WI upright microscope modified with a Prairie Technologies scanning mirror head. An Olympus UPlanApo 60x, 1.2NA water-immersion objective was used for both focusing into the sample and recollecting the fluorescent signal. A 660DCXR dichroic mirror separated the fluorescence from the input laser light, and further blocking of the fundamental was performed by a short-pass filter with a cutoff at 650 nm. Finally, a 550DCXR dichroic was used to separate the fluorescence signal into two photomultiplier tube (PMT) channels for simultaneous multicolor detection.

Dispersion in the setup was corrected via implementation of Multiphoton Intrapulse Interference Phase Scan (MIIPS) with the femtoJock pulse shaper [20–22]. The theory of this technique is reviewed in Chapter II of this thesis. In short, MIIPS records the output second harmonic (SH) signal from a beta barium borate (BBO) crystal as the SLM applies varying amounts of phase to the pulse. The SH signal is

maximized when the dispersion is minimized; at this applied phase, the dispersion in the system is compensated and TL pulses are achieved. For accurate compensation in the microscope, MIIPS must be performed after all microscope optics including the objective. This means that the SH generation step must occur after the objective. For the use of the water immersion objective, this was accomplished by mounting a 1 mm thick BBO crystal on a #1 glass coverslip and placed at the focus of the microscope. The cover slip served to protect the BBO crystal from the water used for immersion. After the crystal, a 670 nm short-pass filter was used to block the fundamental light and the SH light was coupled into a spectrometer. The MIIPS routine was performed by the femtoJock box and its associated software. The final pulse shape was applied to the SLM as a TL baseline, and additional shapes were added to this. Further dispersion compensation was achieved with chirped mirrors using a total of 8 pairs of bounces with -200 fs^2 per bounce; this was used in conjunction with MIIPS.

When choosing fluorophores for two-photon FRET microscopy, two key factors must be considered. The first is that for FRET to occur efficiently, the emission spectrum of the donor must overlap with the one-photon excitation spectrum of the acceptor. This holds for two-photon excited FRET, as the fluorescence emission of the donor is unchanged [16] and the dipole-dipole energy transfer of FRET is unaffected by the method of donor excitation. The second is that the two-photon excitation spectra of the fluorophores should overlap with the spectrum of the laser. It must be possible to selectively excite both the donor and the acceptor fluorophores in order to acquire all images needed for FRET stoichiometry calculations, so the overlap of the laser spectrum with the acceptor's excitation spectrum must be considered in addition to that of the donor. The spectrum of the laser is shown in figure 5.5 and the two-photon cross-sections of the fluorophores used in this experiment are shown in figure 5.6 (taken from [19]). In figure 5.6, the two-photon absorption spectrum is in red, the one-photon absorption spectrum is in black, and the emission spectrum

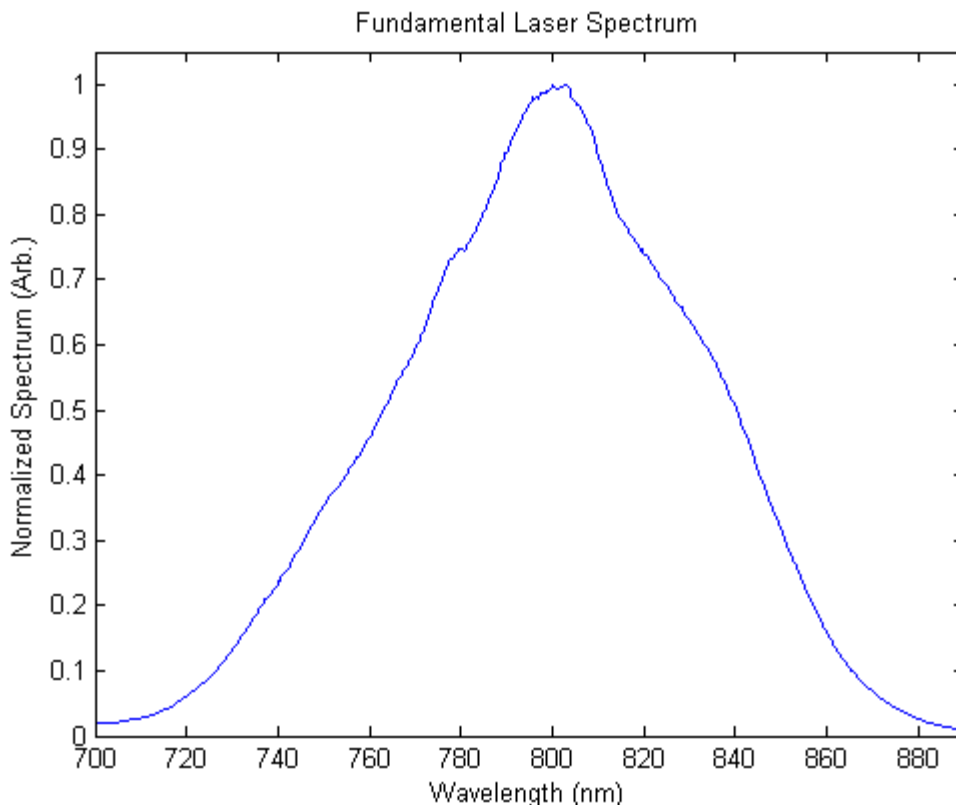


Figure 5.5: Spectrum of the laser used for FRET stoichiometry experiments.

is in blue. The donor in this experiment was mTFP1.0 (referred to as TFP) and the acceptor was TagRFpT. The spectrum for TagRFpT is shown, but the two are spectrally similar [23, 24]. The emission spectrum of TFP overlaps with the one-photon absorption spectrum of TagRFpT over wavelengths of approximately 500-600 nm, satisfying that requirement for FRET. In addition, comparison of these spectra with the laser spectrum shows that with phase shaping, both fluorophores can be selectively excited. This takes advantage of the fact that TagRFpT shows a large peak in its two-photon absorption spectrum at shorter wavelengths than expected. It is thought that this is due to transitions to excited states higher than S_1 [18, 19]. The TFP-TagRFpT construct used in this experiment had a FRET efficiency of 9% measured by acceptor photobleaching.

To perform the required selective excitation of both the donor and acceptor fluo-

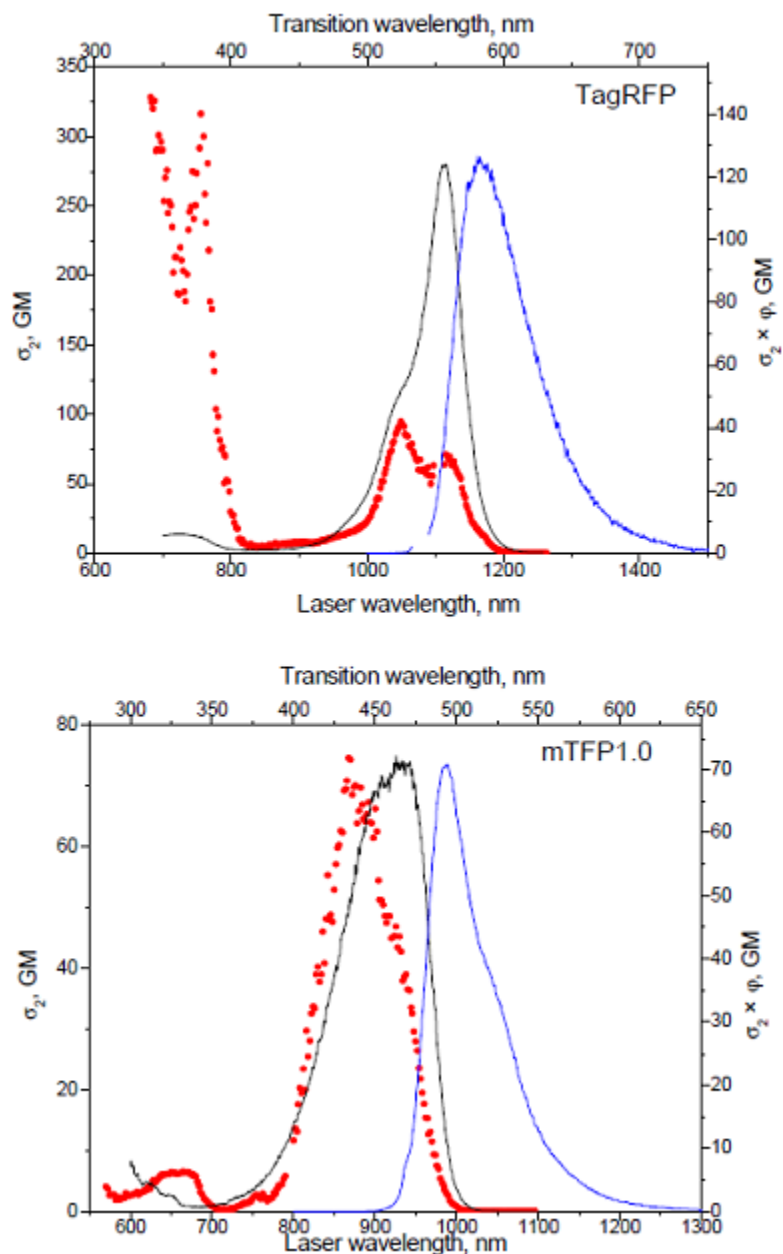


Figure 5.6: Two-photon cross-sections of fluorophores used for FRET stoichiometry. The two-photon absorption spectrum is shown in red, the one-photon absorption spectrum is in black, and the emission spectrum is in blue. mTFP1.0 was the donor and TagRFPt (spectrally similar to TagRFP [23, 24]) was the acceptor. Note that the emission spectrum of TFP overlaps with the one-photon absorption spectrum of TagRFPt, facilitating FRET. Spectra are taken from [19].

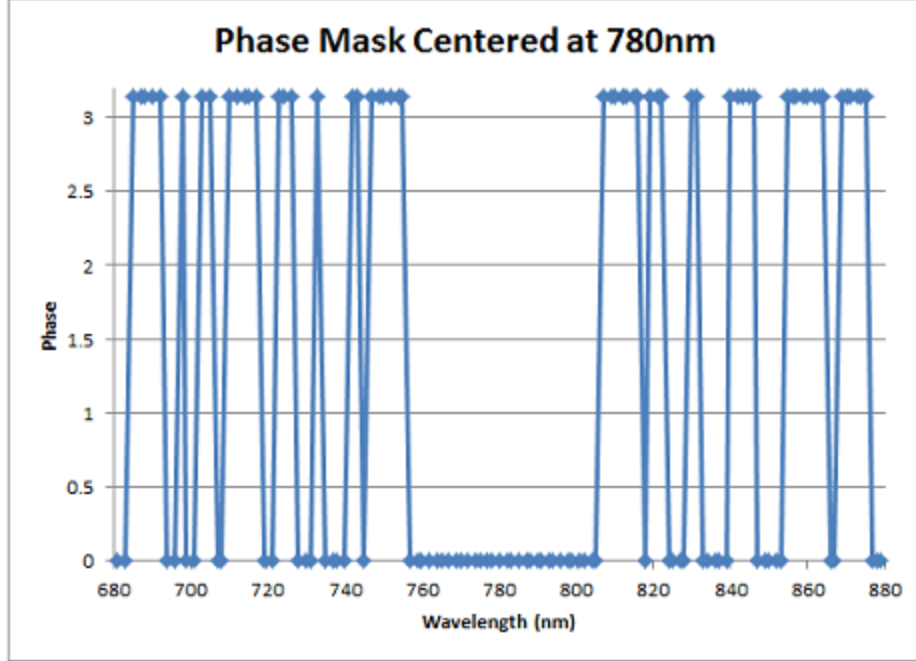


Figure 5.7: Phase mask for selective excitation of TagRFPt.

rophores, two phase masks were created and applied to the SLM. These were designed following the method outlined by Comstock *et al.* [25]. For excitation of the acceptor TagRFPt, a phase mask centered at 780 nm in the fundamental (corresponding to 390 nm in the SH) with a 50 nm central flat section was created; this is shown in figure 5.7. The mask is 128 elements long, with the flat section centered around the desired two-photon excitation wavelength maximum. The mask is symmetric around this region and consists of a semi-random choice of zero or π at each point based on a prime number sequence. The sequence could be multiplied by a spacing factor to adjust the number of pixels in each zero or π region before flipping to the other value, and the prime number sequence could start at different integers. These acted as optimization parameters for the masks. Due to TagRFPt's strong two-photon absorption at shorter wavelengths [18, 19], this phase shape is actually centered at shorter wavelengths than the mask designed for TFP. The TFP mask, shown in figure 5.8, is centered at 820 nm in the fundamental (corresponding to 410 nm in the SH) with a 50 nm central flat section. It was designed following the same methods used

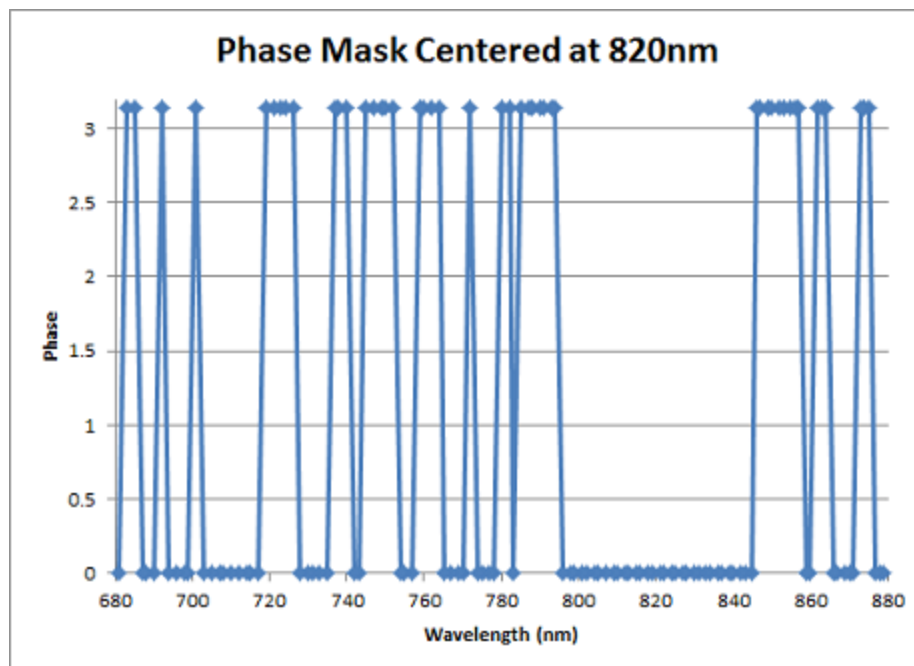


Figure 5.8: Phase mask for selective excitation of TFP.

for the TagRFpT mask. The SH spectra of the TL pulse and the two shaped pulses are shown in figure 5.9. They are centered appropriately, at 390 nm and 410 nm.

The shaped and TL pulses were used to image multiple cells in different sample types. To determine the constants used in FRET stoichiometry (i.e. the α , β , θ , and η values), samples of the acceptor and donor only are required. In addition, a sample containing only the linked donor-acceptor construct is needed to determine the gamma and xi factors, and a sample containing both the donor and acceptor unlinked so that FRET cannot occur is used as a control. The experimental samples consist of the linked construct plus excess donor or acceptor. All samples were COS-7 cells expressing the various combinations of TFP, TagRFpT, and TFP-TagRFpT. The cells were initially grown in 100 mm tissue culture dishes with 10 mL Dulbecco's Modified Eagle's Medium (DMEM) supplemented with 10% fetal bovine serum and 1% each Penicillin-Streptomycin and GlutaMAX glutamine. When the cells were confluent enough to split, the media was aspirated and 5 mL Phosphate-Buffered Saline (PBS) at pH 7.4 was used to rinse the dish. The PBS was then also aspirated and 1 mL of

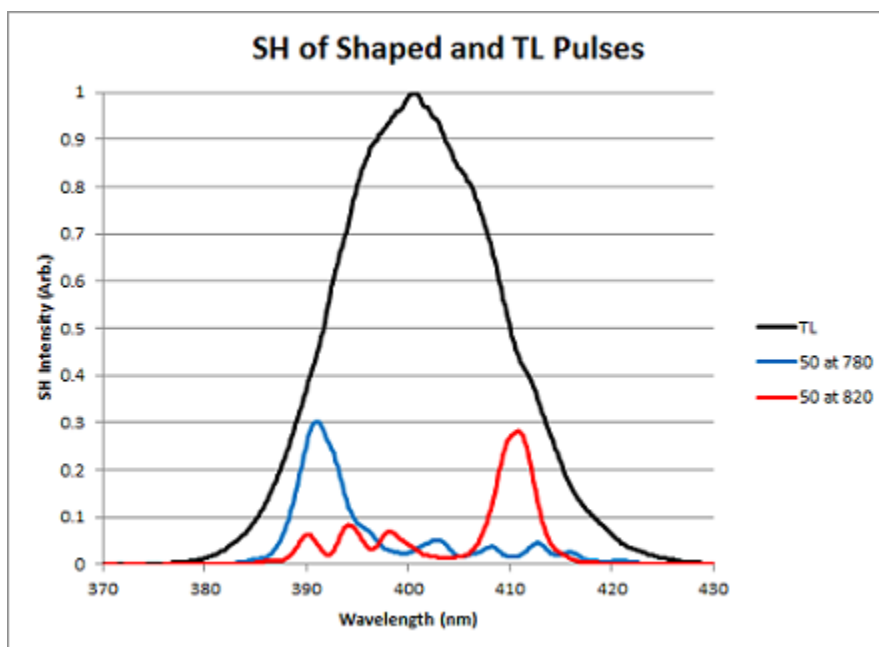


Figure 5.9: SH spectra of shaped and TL pulses for FRET stoichiometry.

0.25% Trypsin-EDTA was added. The dish was placed in the incubator for several minutes to allow the cells to loosen from the surface of the dish. Once the cells detached, 9 mL of the DMEM-based media was added to nullify the Trypsin-EDTA. A hemacytometer was used to count the cells, and approximately 60,000 cells were added to each of six 35 mm tissue culture dishes. This created one dish each for TFP-only cells, TagRFpT-only cells, TFP-TagRFpT (the FRET construct) cells, TFP + TagRFpT (unlinked, no FRET) cells, TFP-TagRFpT + TFP (construct plus excess TFP) cells, and TFP-TagRFpT + TagRFpT (construct plus excess TagRFpT) cells. The dishes were filled to approximately 2 mL final volume with media and placed in the incubator for 24 hours.

For transfection, 100 μL of Opti-Mem reduced serum media was placed in each of six small eppendorf tubes, one for each dish to be transfected. A total of approximately 0.5 μg of purified plasmid DNA was added to each eppendorf, split evenly between the number of fluorophores being introduced. For example, the TFP-only cells used 0.5 μg of TFP DNA, but the TFP + TagRFpT cells used 0.25 μg of each of

the two individual DNAs. To perform the transfection, 3 μL of FuGene 6 transfection reagent was added to each tube, then the tubes were shaken to mix and allowed to sit at room temperature for 15 minutes to incubate. The solutions were then remixed by gentle pipetting and added dropwise to the six tissue culture dishes from the previous day, one eppendorf tube for each dish. The cells were then returned to the incubator for an additional 24 hours to allow protein expression.

Just before imaging, the media in the dishes was removed and replaced with 2 mL of Ringer's Buffer. The dishes were kept at 37° C during imaging and the objective was immersed directly into the buffer for image acquisition. To choose a region of interest for imaging, the dish was viewed with the microscope eyepiece and an Exfo fluorescence lamp for excitation. The microscope was switched to laser excitation and PMT detection just before image acquisition; laser power at the sample was approximately 3.5 mW. Visualization and image acquisition were performed with Prairie Technologies' PrairieView software. After focusing on the cells, the an image was taken with the first of the two pulse shapes used for excitation. The beam was blocked to minimize laser exposure and the second pulse shape was applied, then its image was taken. The beam was then blocked for a final time while the TL pulse was applied and the final image was acquired. Consequently, the data is organized in fields of view, corresponding to each imaged area of interest, with three images acquired from each field of view. To prevent confusion with potential photobleaching or photodamage effects, the order in which the two shapes were applied was alternated. This was repeated for multiple cells in each sample dish and for all six samples; the objective was cleaned between samples with lens tissue and a mixture of ethanol and acetone. Images were 512x512 pixels, corresponding to an area of approximately 220x220 μm , and were taken as averages of 16 frames with a 4 μs per pixel dwell time. In addition to the cell samples, images were acquired from uniformly-doped fluorescent plastic slides to determine the shading patterns across the field of view.

These images were taken under the same conditions as the cell images, with only the PMT voltages adjusted to compensate for the brighter fluorescence from the slide.

After acquisition, all image analysis was performed in Matlab. First, image-specific background subtraction was performed. The images from the two PMT channels taken under TL excitation conditions were summed, and that resulting image was used to identify two regions in each field of view with no fluorescence signal. These regions were used to create a mask which was then applied to the images taken with the shaped pulses from that field of view. The pixels in the mask were averaged to find a single background value which was subtracted from each pixel in the image. The background values varied by less than 2% across the image field, indicating that any shading patterns present did not affect the background subtraction. Each field of view imaged used a different mask, and the backgrounds of each individual image determined the background value subtracted from that image. After background subtraction, shading correction was performed using the images from the fluorescent slide. The fluorescent slide images were first corrected for bias by subtracting an image taken under identical imaging conditions but with the beam blocked. Then, all other images were corrected according to the equation [14]

$$\text{Corrected Intensity} = (\text{Maximum Intensity of Shading Image}) * \frac{\text{Experimental Image}}{\text{Shading Image}} \quad (5.52)$$

Following these image correction steps, the pixel intensities in individual cells are averaged to a single value. These averaged values from the cell in each of the I_A , I_D , and I_F images are used as the I_A , I_D , and I_F terms in the FRET stoichiometry equations. Before averaging, the images are masked such that saturated pixels are excluded. The user then identifies each individual cell so that only the pixels in that cell are included in the average. An example showing a corrected image of several

cells expressing TagRFPT and its corresponding mask is shown in figure 5.10. Note that the saturated cell in the top portion of the image is excluded, as are isolated saturated regions in one of the central cells. Four cells are passed by the mask for averaging and use in subsequent calculations.

5.4.2 Results

The first step in the FRET stoichiometry calculations is to determine the constants α , β , η , and θ . The alpha constant is defined as $\alpha = I_F/I_A$ and it quantifies the extent to which the acceptor fluorophore is accidentally directly excited by the donor pulse shape. It is measured in samples containing acceptor (TagRFPT) only. Over a sample of 15 cells, $\alpha = 0.43 \pm 0.02$ calculated using the average cell intensities. This value indicates that the intensity in the I_A image is larger than that in the I_F image, reflecting the fact that the pulse shape designed for the acceptor does in fact excite it more efficiently than the pulse shape designed for the donor. Next, the beta constant is found; this quantifies how the donor fluorescence is split between detection channels. It is defined as $\beta = I_F/I_D$ and is calculated from cells expressing the donor (TFP) only. Over a sample of 19 cells, beta is found to be $\beta = 0.06 \pm 0.004$. The very small beta value makes sense, as it is due to much more donor fluorescence appearing in the donor emission channel than the acceptor emission channel.

The remaining constants, eta and theta, are the constants that are new to two-photon FRET stoichiometry. To determine these, the image I_N is introduced, which is the image taken under acceptor excitation conditions and in the detector's emission channel. That is, it is the opposite of the FRET condition. I_N is implemented here because it facilitates calculation of eta and theta without relying on images which give only very dim fluorescence - using such images in calculations makes it difficult to obtain accurate results. Eta is the equivalent of beta, but for the acceptor. It defines how the acceptor fluorescence is split between detection channels and is calculated as

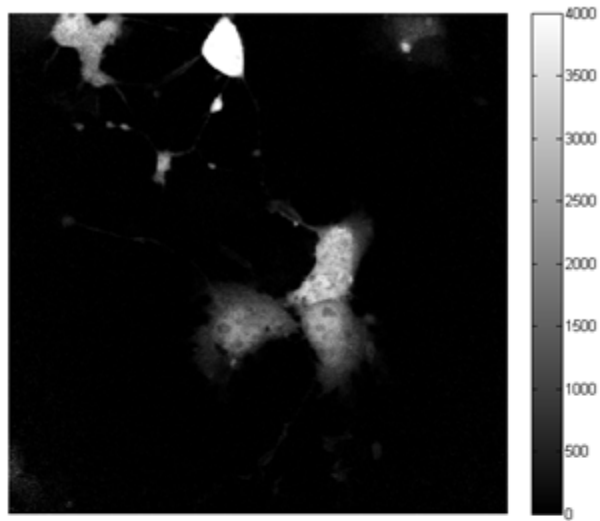


Figure 5.10: Sample corrected image and corresponding mask for cells expressing TagRFpt. Note that the saturated cell in the top portion of the image is excluded, as are isolated saturated regions in one of the central cells.

$\eta = I_A/I_N$ from a sample containing acceptor only. Using the average intensities of 15 cells, eta is $\eta = 3.46 \pm 0.11$. This value is in agreement with the expectation that more acceptor fluorescence is detected in the acceptor detection channel than in the donor detection channel. Finally, theta is the equivalent of alpha, but for the donor. It determines how much the donor can be directly excited by the acceptor pulse shape. Based on a population of 19 cells, theta is found to be $\theta = 1.08 \pm 0.05$ based on cell intensity averaging. This value for theta indicates that the donor is more effectively excited by its pulse shape than by the shape designed for the acceptor, although the value close to one indicates that the improvement is small.

With these constants determined, the next step is to use them in the determination of gamma, which is calculated according to equation (5.40). This is found by looking at the sample containing the linked construct of donor and acceptor and making the assumption that all acceptors present are in complex. To find gamma, the term in the denominator using the average intensity values is calculated for each cell and then an average result is found. The final subtraction of one and division of the FRET efficiency is performed with this average value. For a population of 18 cells, the intermediate result was 1.16 ± 0.09 leading to a final gamma value of $\gamma_{TPE} = 0.57$. Xi is also found from the cells expressing the linked construct with the assumption that all donors present are in complex. Calculation with equation (5.49) and all previously found constants gives $\xi = 0.67 \pm 0.65$ from 18 cells.

Continuing to work with the cells expressing the linked construct permits a test of the equations for the fractions of donor and acceptor in complex. These values should be approximately one for the linked construct, as all fluorophores present are in complex. Furthermore, the values of γ_{TPE} and ξ to be used in these calculations were derived under the assumption that the fractions equal one. The fraction of acceptor in complex, f_A , is found using equation (5.41); using the averaged intensities of 18 cells yields $f_A = 1.00 \pm 0.58$. Similarly, the fraction of donor in complex, f_D , is found

with equation (5.50) to be $f_D = 1.6 \pm 0.89$. These values are both one to within a single standard deviation, although the standard deviations are relatively large. This calculation can be repeated for the sample of cells containing both free acceptor and free donor; in this sample, there is no FRET because no fluorophores are in complex. Consequently, both the fraction of donor and fraction of acceptor in complex should be zero. For a sample of 10 cells in this sample condition, $f_A = 0.40 \pm 0.48$ and $f_D = 0.29 \pm 0.38$. Again, these values are within one standard deviation of the expected result.

The final set of samples to consider are the samples of unknown stoichiometry, which contain either complex plus excess donor or complex plus excess acceptor. The fractions of donor and acceptor in complex can be calculated in these as well as a test of FRET stoichiometry. First, the sample containing complex plus excess acceptor is considered. In this sample, it is expected that $f_D = 1$ and $f_A < 1$. For a sample size of six cells, these fractions were found to be $f_A = 0.45 \pm 0.54$ and $f_D = 1.53 \pm 2.02$. In the sample of complexed fluorophores plus excess donor, it is expected that $f_D < 1$ and $f_A = 1$. Calculated results for these fractions were $f_A = -0.41 \pm 0.5$ and $f_D = -0.19 \pm 0.27$.

5.5 Future Work

The results presented above are significant progress toward the implementation of FRET stoichiometry in two-photon microscopy. A new theory considering all possible fluorescence contributions was derived to adapt FRET stoichiometry for two-photon microscopy experiments. It was then applied to images of live cells and promising results were obtained - although the standard deviations were large, indicating variation across cells, calculated results were generally within one standard deviation of the expected values. Simulations of FRET stoichiometry image data and calculations are currently being implemented to determine how to improve the results. Active

areas of investigation include methods to decrease the large standard deviations and transitioning to pixel-by-pixel calculations, where the individual pixel intensities from the images are used as the I_A , I_D , and I_F values in the stoichiometry calculations. This would make it possible to view the stoichiometry results as images, giving a clearer picture of the interaction in individual cells.

Several ideas are currently being investigated in the simulations. One of these is the use of a non-optimal dichroic to separate the fluorescence channels. This would serve to increase the fluorescence crosstalk; the idea that this may be beneficial is counterintuitive. The amount of crosstalk is used directly to determine the beta and eta constants needed for the stoichiometric calculations. When this crosstalk is very small - as is the case for well-chosen dichroics - the image intensities used to determine the constants are small, potentially introducing extra noise and uncertainty into the results. This effect may already be present in the data presented here - beta is very small compared to the other constants, indicating low crosstalk between the detection channels. Likewise, eta effectively looks at the inverse of beta and is relatively large. Purposefully choosing a “bad” dichroic to boost the fluorescence crosstalk boosts the signal in the images used for calculations, potentially leading to a better determination of the constants.

Two additional ideas are being tested in simulations. The first is to improve the overall fluorescence signal in the sample by using brighter fluorophores. The relatively narrow bandwidth of the laser used for these experiments limited the choice of fluorescent proteins that could be used, as both the donor and acceptor two-photon absorption spectra had to overlap with the laser. The second is to choose a FRET pair with a higher FRET efficiency. The TFP-TagRFpT pair used here has an efficiency of 9%, but pairs with efficiencies around 20% are possible. As with the overall fluorophore choice, this was dictated by the available laser bandwidth. The FRET stoichiometry system described here is currently being transitioned to use with

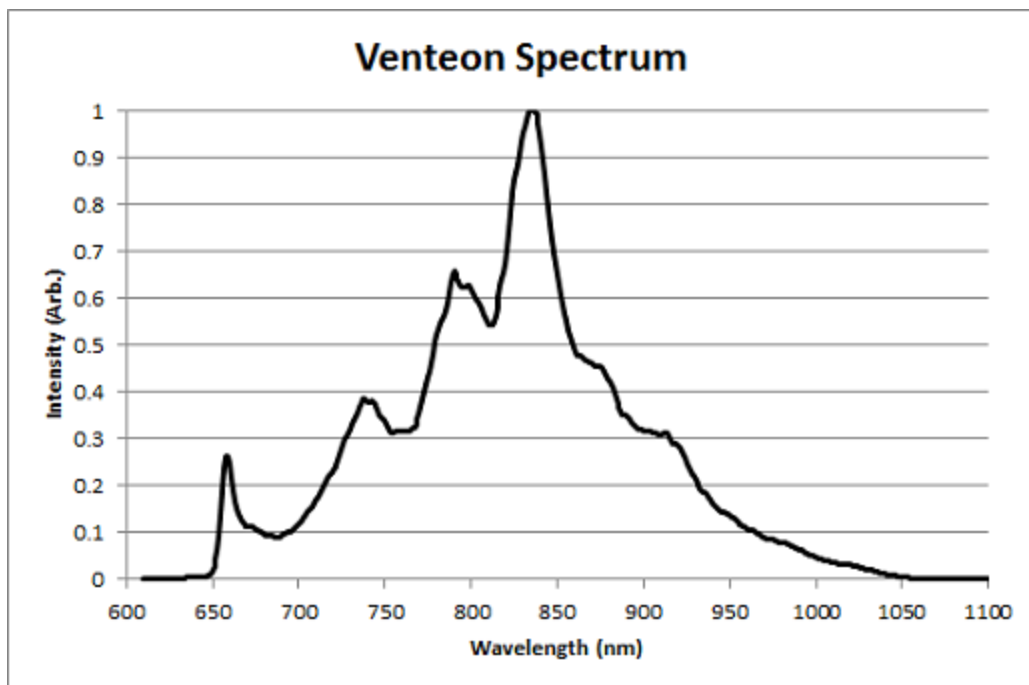


Figure 5.11: Spectrum of Venteon ultrabroadband laser.

a Venteon Pulse:One laser, which has a larger bandwidth; this is shown in figure 5.11. This increases the number of fluorophores that can be excited and can thus be used to create new FRET pairs. With improvements such as these, two-photon FRET stoichiometry should be viable for a range of biological systems.

References

- [1] L. Stryer and R. P. Haugland. Energy transfer: a spectroscopic ruler. *Proceedings of the National Academy of Sciences of the United States of America*, 58(2):719–726, 1967.
- [2] P. R. Selvin. [13] fluorescence resonance energy transfer. *Methods in enzymology*, 246:300–334, 1995.
- [3] G. W. Gordon, G. Berry, X. Liang, B. Levine, and B. Herman. Quantitative fluorescence resonance energy transfer measurements using fluorescence microscopy. *Biophysical Journal*, 74(5):2702–2713, 1998.
- [4] Z. Xia and Y. Liu. Reliable and global measurement of fluorescence resonance energy transfer using fluorescence microscopes. *Biophysical Journal*, 81(4):2395–2402, 2001.
- [5] M. G. Erickson, B. A. Alseikhan, B. Z. Peterson, and D. T. Yue. Preassociation of calmodulin with voltage-gated calcium channels revealed by fret in single living cells. *Neuron*, 31(6):973–985, 2001.
- [6] H. Wallrabe, M. Stanley, A. Periasamy, and M. Barroso. One-and two-photon fluorescence resonance energy transfer microscopy to establish a clustered distribution of receptor-ligand complexes in endocytic membranes. *Journal of Biomedical Optics*, 8(3):339–346, 2003.
- [7] W. Denk, J. H. Strickler, and W. W. Webb. Two-photon laser scanning fluorescence microscopy. *Science*, 248(4951):73–76, 1990.
- [8] W. Denk. Two-photon excitation in functional biological imaging. *Journal of Biomedical Optics*, 1(3):296–304, 1996.
- [9] W. R. Zipfel, R. M. Williams, and W. W. Webb. Nonlinear magic: multiphoton microscopy in the biosciences. *Nature Biotechnology*, 21(11):1369–1377, 2003.
- [10] A. Volkmer, V. Subramaniam, D. J. S. Birch, and T. M. Jovin. One-and two-photon excited fluorescence lifetimes and anisotropy decays of green fluorescent proteins. *Biophysical Journal*, 78(3):1589–1598, 2000.

- [11] Y. Chen and A. Periasamy. Characterization of two-photon excitation fluorescence lifetime imaging microscopy for protein localization. *Microscopy research and technique*, 63(1):72–80, 2004.
- [12] Y. Chen, J. D. Mills, and A. Periasamy. Protein localization in living cells and tissues using fret and flim. *Differentiation*, 71(9-10):528–541, 2003.
- [13] B. J. Bacskai, J. Skoch, G. A. Hickey, R. Allen, and B. T. Hyman. Fluorescence resonance energy transfer determinations using multiphoton fluorescence lifetime imaging microscopy to characterize amyloid-beta plaques. *Journal of Biomedical Optics*, 8(3):368–375, 2003.
- [14] A. Hoppe, K. Christensen, and J. A. Swanson. Fluorescence resonance energy transfer-based stoichiometry in living cells. *Biophysical Journal*, 83(6):3652–3664, 2002.
- [15] A. D. Hoppe and J. A. Swanson. Cdc42, rac1, and rac2 display distinct patterns of activation during phagocytosis. *Molecular Biology of the Cell*, 15(8):3509–3519, 2004.
- [16] J. R. Lakowicz. *Principles of Fluorescence Spectroscopy*. Springer, 2007.
- [17] A. L. Mattheyses, G. Meaden, M. Marchand, A. Hoppe, and S.L. Shorte. A user’s guide and utility for fret stoichiometry. http://www.pfid.org/html/un_fret/?en, Accessed June 2009. Can now be accessed via the Internet Archive Wayback Machine at http://web.archive.org/web/20100824023236/http://www.pfid.org/html/un_fret/?en.
- [18] M. Drobizhev, N. S. Makarov, T. Hughes, and A. Rebane. Resonance enhancement of two-photon absorption in fluorescent proteins. *The Journal of Physical Chemistry B*, 111(50):14051–14054, 2007.
- [19] M. Drobizhev, N. S. Makarov, S. E. Tillo, T. E. Hughes, and A. Rebane. Two-photon absorption properties of fluorescent proteins. *Nature Methods*, 8(5):393–399, May 2011.
- [20] Y. Coello, V. V. Lozovoy, T. C. Gunaratne, B. Xu, I. Borukhovich, C. Tseng, T. Weinacht, and M. Dantus. Interference without an interferometer: a different approach to measuring, compressing, and shaping ultrashort laser pulses. *JOSA B*, 25(6):A140–A150, 2008.
- [21] V. V. Lozovoy, I. Pastirk, and M. Dantus. Multiphoton intrapulse interference. iv. ultrashort laser pulse spectral phase characterization and compensation. *Optics Letters*, 29(7):775–777, 2004.
- [22] B. Xu, J. M. Gunn, J. M. Dela Cruz, V. V. Lozovoy, and M. Dantus. Quantitative investigation of the multiphoton intrapulse interference phase scan method for simultaneous phase measurement and compensation of femtosecond laser pulses. *JOSA B*, 23(4):750–759, 2006.

- [23] N. C. Shaner, M. Z. Lin, M. R. McKeown, P. A. Steinbach, K. L. Hazelwood, M. W. Davidson, and R. Y. Tsien. Improving the photostability of bright monomeric orange and red fluorescent proteins. *Nature Methods*, 5(6):545–551, 2008.
- [24] E. Salomonsson, L. A. Mihalko, V. V. Verkhusha, K. E. Luker, and G. D. Luker. Cell-based and in vivo spectral analysis of fluorescent proteins for multiphoton microscopy. *Journal of Biomedical Optics*, 17(9):0960011–0960019, 2012.
- [25] M. Comstock, V. Lozovoy, I. Pastirk, and M. Dantus. Multiphoton intrapulse interference 6; binary phase shaping. *Optics Express*, 12(6):1061–1066, 2004.

CHAPTER VI

Conclusion

This thesis has demonstrated the potential of ultrafast pulse shaping to enable new measurements in two-photon fluorescence microscopy. Utilizing phase shaping to perform selective excitation of fluorescent proteins expressed in live cell samples - the common theme in the work presented here - overcomes many of the barriers that exist in performing multicolor two-photon imaging with conventional methods. Current methods for such multicolor imaging fall into one of three broad categories: the use of tunable lasers, which limits the temporal resolution of the experiment; the use of multiple beams, which require expensive laser systems that can be difficult to align; and the use of broadband lasers, which provides no selectivity in which fluorophores can be excited. The implementations of ultrafast pulse shaping demonstrated in this thesis use a single broadband titanium:sapphire laser in a straightforward optical setup for rapid, selective excitation of multiple fluorophores.

First, the use of linear unmixing to perform three-color fluorescence microscopy was demonstrated [1]. This technique used two different excitation pulse shapes, coupled with two detection channels, to create four imaging conditions. By using a linear unmixing algorithm based on the intensities of these images, the contribution of each of the three fluorophores was calculated and used to identify individual cells. In samples containing cells expressing single fluorophores, the fluorescent signals were

well separated and cells were easily identified based on the fluorophore present. In samples containing cells expressing all three fluorophores, the linear unmixing calculation gave each cell a different color, allowing the cells to be uniquely identified. This method has several benefits over other three-color imaging techniques; one is reduced cost. Existing methods rely on physically distinct excitation and detection channels for each fluorophore present, which becomes prohibitively expensive as the number of colors increases. However, the method presented here can be easily extended to more fluorophores by creating new shaped pulses for excitation and adapting the equations. Linear unmixing also relies less on filters than other existing methods. While this does help to reduce the cost, it also makes linear unmixing a promising technique for use in tissue studies. Because the fluorescence signal can be decreased by scattering in biological systems, removing filters leads to improved signal to noise over other imaging methods.

Next, the potential of ultrafast pulse shaping in two-photon Fluorescence Resonance Energy Transfer (FRET) microscopy was investigated [2, 3]. Shaped pulses were successfully used to distinguish between FRET and non-FRET conditions. This also demonstrated that selective excitation via shaped pulses works for a linked construct of two fluorescent proteins in live cells. Compared to existing two-photon FRET methods, the use of pulse shaping has improved temporal resolution, as it does not depend on tuning a laser to access different fluorophores or acquiring photon counts to generate Fluorescence Lifetime Imaging Microscopy (FLIM) results. The next step is to use these ultrafast pulse shaping techniques to develop a quantitative FRET microscopy method based on FRET stoichiometry. Several steps towards that goal were presented in this thesis. A thorough investigation of the theory behind FRET stoichiometry was conducted, which found that several assumptions made for the one-photon case do not hold for the two-photon case. As a result, a new, fully general theory of two-photon stoichiometry was derived and presented here. This theory

was then applied to images of live cells acquired with phase shaping, and the results were largely consistent with the expected stoichiometry. Although these results are promising, the technique needs to be perfected, and simulation studies are ongoing to investigate potential solutions. Ideas being actively investigated include the use of less-than-optimal filters, brighter fluorophores, and more efficient FRET pairs. An additional possibility is the use of pulse shaping to perform selective excitation in the other quantitative FRET methods discussed in Chapter V; while these methods do not provide the full stoichiometry of the interaction, they do provide information about the FRET efficiency that can be used to investigate how the interaction progresses over time.

Beyond completing the implementation of two-photon FRET stoichiometry, there are several other avenues to be explored to improve the use of ultrafast pulse shaping in two-photon microscopy methods. One of these is the advent of ultrabroadband titanium:sapphire oscillators, with bandwidths of hundreds of nanometers. This larger bandwidth increases the available library of fluorescent proteins that can be excited by the laser, making it possible to choose fluorophores that are ideal for their brightness or other characteristics beyond simply their spectra. An example of this is shown in Chapter III in figure 3.1. This shows the SH spectrum of the Femtolasers Synergy oscillator used for the work presented in this thesis compared to the simulated second harmonic spectrum of an ultrabroadband Venteon oscillator, showing that the Venteon spans an approximately 3 times larger spectral range. Figure 3.1 also shows several potential shaped pulse spectra for excitation of common fluorescent dyes and proteins. It is evident that switching to the Venteon will allow access to a much broader spectrum of fluorophores. This also makes it possible to choose more efficient FRET pairs, as the spectral overlap needed for FRET can be prioritized over the spectral overlap of the fluorophores with the laser.

Moving beyond phase shaping to create single second harmonic peaks for highly

selective excitation and into the creation of multiple peaks is another area of active exploration. Expanding to two shaped peaks rather than one allows simultaneous excitation of two fluorophores while still excluding others that may be present in the sample. It also makes it possible to adjust the excitation efficiency for the two fluorophores by adjusting the relative second harmonic peak heights of the shaped pulses. This can be easily achieved by designing the phase masks with different flat phase widths. Another possibility for designing double-peak phase masks is the use of genetic algorithms. These have been implemented experimentally, using fluorescent signals to determine the best pulse shapes for selective excitation of individual fluorophores [4–7]. While the work presented in this thesis demonstrates that genetic algorithms are unnecessary for the creation of single peaks - all masks used here were designed based solely on knowledge of the fluorophores' two-photon excitation spectra - they may be helpful in designing more complex masks.

The field of microscopy has seen significant changes and improvements over its hundreds of years, with the implementation of fluorescence as a contrast mechanism, the introduction of FRET for observing dynamic interactions, and the use of two-photon excitation for imaging live biological samples such as cells and tissues. The addition of ultrafast pulse shaping is further changing the field, and the applications presented in this work - linear unmixing for multicolor imaging, the detection of FRET, and the quantification of FRET via two-photon FRET stoichiometry - further enhance the tools available for studying biological systems. These new methods will enable applications such as tracking of interacting species with stoichiometric information from FRET, unique identification of cells expressing multiple fluorophores in a manner similar to Brainbow [8], or the ability to quantitatively image multiple interacting or non-interacting FRET pairs [9].

References

- [1] M. H. Brenner, D. Cai, J. A. Swanson, and J. P. Ogilvie. Two-photon imaging of multiple fluorescent proteins by phase-shaping and linear unmixing with a single broadband laser. *Optics Express*, 21(14):17256–17264, Jul 2013.
- [2] M. H. Brenner, D. Cai, S. R. Nichols, S. W. Straight, A. D. Hoppe, J. A. Swanson, and J. P. Ogilvie. Pulse shaping multiphoton fret microscopy. In *SPIE BiOS*. International Society for Optics and Photonics, 2012.
- [3] M. H. Brenner, D. Cai, S. W. Straight, J. A. Swanson, and J. P. Ogilvie. Pulse-shaping-based two-photon fret microscopy. In *EPJ Web of Conferences*, volume 41, page 11009. EDP Sciences, 2013.
- [4] T. Brixner, N. H. Damrauer, B. Kiefer, and G. Gerber. Liquid-phase adaptive femtosecond quantum control: Removing intrinsic intensity dependencies. *The Journal of Chemical Physics*, 118(8):3692–3701, 2003.
- [5] E. R. Tkaczyk, A. H. Tkaczyk, K. Mairing, J. Y. Ye, J. R. Baker Jr, and T. B. Norris. Control of two-photon fluorescence of common dyes and conjugated dyes. *Journal of Fluorescence*, 19(3):517–532, 2009.
- [6] E. R. Tkaczyk, A. H. Tkaczyk, K. Mairing, J. Y. Ye, J. R. Baker Jr, and T. B. Norris. Quantitative differentiation of dyes with overlapping one-photon spectra by femtosecond pulse-shaping. *Journal of Luminescence*, 130(1):29–34, 2010.
- [7] M. Comstock, V. Lozovoy, I. Pastirk, and M. Dantus. Multiphoton intrapulse interference 6; binary phase shaping. *Optics Express*, 12(6):1061–1066, 2004.
- [8] J. Livet, T. A. Weissman, H. Kang, R. W. Draft, J. Lu, R. A. Bennis, J. R. Sanes, and J. W. Lichtman. Transgenic strategies for combinatorial expression of fluorescent proteins in the nervous system. *Nature*, 450(7166):56–62, November 2007.
- [9] A. D. Hoppe, B. L. Scott, T. P. Welliver, S. W. Straight, and J. A. Swanson. N-way fret microscopy of multiple protein-protein interactions in live cells. *PLoS ONE*, 8(6):e64760, 06 2013.